附件 2   浙江水利水电学院"南浔青年学者"申请表

姓　名	冯伯华	出生年月年龄（年龄）	___1994___年__4__月岁（ 28 岁）	参加工作时间	___2022___年_8_月
现所在单位（部门）	机械与汽车工程学院	最高学历/学位	研究生/博士	专业技术职务	讲师

符合条款	符合科研类，（1）两篇 SCI TOP 期刊，绩点 100，（2）一篇 EI，绩点 10。

所涉业绩	教学类绩点：_____	
	科研类绩点：___110___	1.一作发表《Friction》一篇，《Journal of Materials Processing Technology》一篇，《机械工程学报》一篇
	人才称号类绩点：_____	
	总绩点	110
	备注：请严格按照《浙江水利水电学院"南浔青年学者"实施办法（试行）》（浙水院〔2022〕114号）附件《业绩成果绩点赋值项目库》的类目、分类、等级（等次）、绩点填写。	

个人承诺	**本人承诺上述所填内容真实、准确；如有不实，本人承担相应责任。** 签名：冯伯华　时间：2022.11.24

以上部分由申请人填写，所在单位审核。以下由单位（部门）和学校填写。

所在单位（部门）意见	1.经审核，申请人所填内容：□属实　　□不属实； 2.是否符合所申请的类别：□符合　□不符合； 3.是否同意推荐：□同意　□不同意。 　　　　　　　　　　　　　　负责人签名：　　　　（部门盖章） 　　　　　　　　　　　　　　___年___月___日

科技处审核意见	负责人签名：　　　（部门盖章） ___年___月___日	教务处审核意见	负责人签名：　　　（部门盖章） ___年___月___日

其他相关职能部门审核意见	负责人签名：　　　（部门盖章） ___年___月___日

学校意见	（学校盖章） ___年___月___日

备注：表格请用 A4 纸打印，有关佐证材料附后。

RESEARCH ARTICLE

Capillary electroosmosis properties of water lubricants with different electroosmotic additives under a steel-on-steel sliding interface

Bohua FENG[1], **Zhiqiang LUAN**[1], **Tao ZHANG**[1], **Jiawei LIU**[1], **Xiaodong HU**[1], **Jiju GUAN**[2], **Xuefeng XU**[1,*]

[1] *Key Laboratory of Special Purpose Equipment and Advanced Manufacturing Technology, Ministry of Education & Zhejiang Province, Zhejiang University of Technology, Hangzhou 310023, China*

[2] *College of Mechanical Engineering, Changshu Institute of Technology, Changshu 215500, China*

Abstract: The process of lubricant penetration into frictional interfaces has not been fully established, hence compromising their tribological performance. In this study, the penetration characteristics of deionized water (DI water) containing an electroosmotic suppressant (cetyltrimethylammonium bromide (CTAB)) and an electroosmotic promoter (sodium lauriminodipropionate (SLI)), were investigated using steel-on-steel friction pairs. The results indicated that the lubricant with electroosmotic promoter reduced the coefficient of friction and wear scar diameter, whereas that with an electroosmotic suppressant exhibited an opposite behavior compared with DI water. The addition of SLI promoted the penetration of the DI water solution, thus resulting in the formation of a thick lubricating film of iron oxide at the sliding surface. This effectively reduced the abrasion damage, leading to a lower coefficient of friction and wear loss.

Keywords: electroosmosis; friction interface; electroosmotic additives; water lubricants; tribological performance

1 Introduction

In mechanical systems, lubricants are widely used to reduce friction and improve worn surface quality [1]. During cutting processes, lubricants can enter contact surfaces to form lubricating films through the gaps at the tool–chip interface, which generates a film-to-film contact of low shearing resistance and hence improves interfacial friction and wear conditions. Nevertheless, the penetration mechanism of lubricants into the interface of frictional pairs is still not well understood, thus compromising their cutting performance. Previous studies [2–4] pointed out that capillaries exist at the contact interface of two sliding pairs, such as tool–workpiece interfaces and the contact surfaces of friction pairs, and lubricants thus penetrate the contact zone through these capillaries. In recent years, various transparent tools have been designed and used in the machining of pure lead, aluminum, and copper to study the penetration mechanism of lubricants [5, 6]. The experimental results showed that during machining, capillaries were indeed formed at the end of the tool–chip interface. Many of authors [3, 5] believed that these capillaries play a critical role in lubricant penetration. These capillaries serve as passageways by which lubricants can enter and wet the contact interface and promote the formation of lubricating films. Bieria et al. [7] found that lubricants were driven to the tool–chip interface via these microscale capillaries under both capillary force and atmospheric pressure for lubrication. The study reported in Ref. [8]

---

demonstrated that the penetration depth of lubricants into capillaries was directly proportional to the coefficient of the capillary force in the liquids but inversely proportional to the capillary radius. The pressure formed within the capillaries was also verified to be the main driving force in the lubricant penetration process [9]. Xu et al. [10] studied the effects of capillary force, atmospheric pressure, and capillary wall viscous resistance on the penetration performance of cutting fluids during grinding of Cr12 die steel. Their results showed that the capillary penetration depth of grinding fluids was a complex process dominated by multiple forces. Thus, the process and mechanism of lubricant penetration into frictional interfaces need to be further clarified.

During the friction and wear processes, the contact interface of frictional pairs is broken, scratched, or undergoes plastic deformation. The highly active "fresh" surface is exfoliated, and the electrons overflow from these "fresh" surfaces, leading to electron emission [11], which mainly includes chemi-emission [12], fracto-emission [13, 14], and tribo-emission [15]. Govindaraj and Subbiah [16] observed electron emission during the cutting process of stainless steel, low carbon steel, and copper using carbide tools with different cutting parameters. They pointed out that the magnitude of the electron emission was not only related to the resistivity, hardness, tensile strength, and yield strength of the material, but also to the cutting speed and depth. The electron emission intensity accumulated for 1,000 ms during scratching of a carbon film with a diamond stylus under dry air condition was approximately 100 pC [17]. The magnitudes of the electron emission and tribo-electrification intensity for metal–metal contact are inferior to those between insulators and semiconductors [18], however, it was shown that tens of microvolts could still be generated between friction pairs made of Fe/Fe [19]. The emitted electrons are affected by a strong normal electric field at the friction interface, causing a gas discharge in the gap of the friction pair that generates a plasma [20] under dry friction [21] or oil-lubricated [22] conditions. These triboelectric phenomena can generate a self-excited electric field at the friction interface, which may generate an electrokinetic effect on the lubricants in the capillaries, promoting the penetration of lubricants through capillary electroosmosis.

Capillary electroosmosis is a process in which the electrolyte solution in a capillary moves relative to the fixed wall of the capillary under an applied electric field. The capillary, axial electric fields at both ends of the capillary, and electrical double layer (EDL, including the diffusion layer and fixed layer) produced at the liquid/solid interface are the necessary factors for capillary electroosmosis [23]. The walls of metals, quartz, and most natural substances are negatively charged when they are immersed in a water-based solution [24]. The formation of the EDL is mainly due to the resulting surface charge of the capillary wall. Co-ions from the solution are repelled and counter-ions are attracted to screen the surface charges, creating a charged region close to the capillary inner surface [25]. Because of the strong electrostatic effect between ions, the fixed layer ions are immobilized, whereas the diffusion layer ions move under the effect of the electric field. The movement of diffusion layer ions drives the solution in the capillary to move concurrently under the influence of the solution viscosity and finally forms an electroosmotic flow (EOF) [26]. In general, the EOF can be promoted by enhancing the electric field strength [27], increasing the pH [28], and reducing the internal diameter of the capillaries [29]. Moreover, zwitterionic surfactants [30] (such as 3-[(3-cholamidopropyl)-dimethylammonio]-1-prop anesulfonate (CHAPS) and sodium lauriminodipr-opionate (SLI)) can improve the EOF, but cationic surfactants [31] (such as cetyltrimethylammonium bromide (CTAB) and tetradecyltrimethylammonium bromide (TTAB)) may change the EOF direction [29] due to a change in the EDL properties caused by the adsorption of electroosmotic additive molecules on the capillary surface. Chen et al. [32] systematically studied the application of a high-pressure electro-osmotic pump in micro-column liquid chromatography and designed an electroosmotic pump with an output pressure of at least 5 MPa and a stable flow rate of about 1 μL/min for pure water and methanol. They reported that the EOF rate and pressure could be controlled quantitatively by adjusting the

driving voltage at both ends of the capillary and the diameter of the capillary. Wang and Wu [33] investigated the driving characteristics of microfluids on a moving wall. They pointed out that an increase in the moving speed of the wall could improve the EOF speed and rate when the fluid pressure in the micro-channel and the driving voltage were constant. Zhong and Chen [34] found that the EOF velocity of deionized (DI) water was approximately 11 mm/s when an electric field of 800 V/cm was applied to both ends of a capillary with a diameter of 25 μm. This result was similar to that (approximately 3.55 mm/s) of an investigation based on a capillary penetration model of the tool–chip contact zone [9].

In this study, we first developed a device for measuring the EOF velocity of DI water with two types of electroosmotic additives at various concentrations. Second, the tribological performances of DI water with the electroosmotic additives were evaluated by four-ball tests of steel-on-steel contact pairs to explore the penetration characteristics of lubricants in the capillaries of the friction interface. Third, we also investigated the effects of different rotational speeds and applied loads on the friction and wear properties when taking the capillary electroosmosis effect in the friction interface into consideration. Finally, X-ray photoelectron spectroscopy (XPS) of the worn surfaces lubricated by DI water with different electroosmotic additives was conducted. The goal of this study is to explore the penetrability of lubricants at steel-on-steel friction interfaces and reveal the mechanism of electroosmosis, which affects the capillary penetration of lubricants at the friction interface.
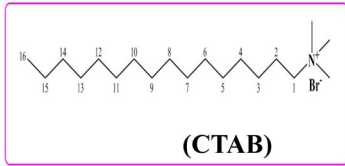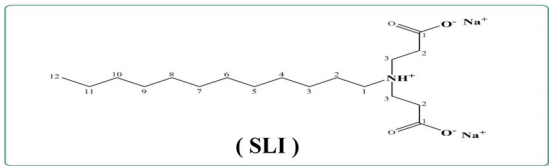
2 Methods

2.1 Preparation of the lubricants

To minimize the influence of excess ions in the lubricating fluid on these exploratory experiment, DI water was used as the reference lubricant because of its simple composition and its positive and negative ions due to hydrolysis of water molecules [35]. In this study, CTAB (cationic surfactant) and SLI (zwitterionic surfactant) were used as electroosmotic additives, and DI water was employed as the base fluid. Electroosmotic additives in powder form were directly added into the base fluid at a concentration range of 0.05–0.3 mM (mmol/L). Subsequently, the lubricants were ultrasonically treated in a water bath for 30 min to ensure complete dissolution of the electroosmotic additives. Both electroosmotic additives were purchased from Shanghai Macklir Biochemical Co., Ltd., China. DI water containing CTAB was used as the electroosmotic suppressant lubricant, and DI water containing SLI was used as the electroosmotic promoter lubricant. The main properties of the electroosmotic additives used are summarized in Table 1.

2.2 Capillary electroosmosis experiment

The surface tension and contact angle of the lubricants utilized in this study were measured by the drop weight method [36] and goniometry method [37], respectively. Each group of experiments was repeated five times at room temperature, and the average value was recorded. To measure the EOF velocity of the various lubricants under different conditions, a

Table 1 Properties of the electroosmotic additives.

Electroosmotic additives	CTAB	SLI
Function	Electroosmotic suppressant	Electroosmotic promoter
Relative molecular mass	364.5	373.44
Physical state	Powder	Powder
Chemical molecular formula	(CTAB)	(SLI)

device, as shown in Fig. 1, was fabricated. The capillaries used in the device were 304 stainless steel tubes with internal/external diameters of 0.5/1.1 mm and 0.9/1.5 mm, and a length of 40 mm. Syringes of 2.5 mL were vertically installed on both sides of the device. After fabricating the device, ultrasonic cleaning with DI water for 10 min was performed to ensure tidiness of the inner wall of the capillaries and syringes. The lubricants were added from one side of the syringe to avoid bubbles, and the two sides of the liquid level in the syringe were finally in horizontal position under the action of gravity. Each type of lubricants was added to the 1.5 mL level of both syringes. The electrodes in contact with the lubricants were platinum electrodes with a diameter of 2 mm. The output end of the high-voltage electrostatic generator (EST802A, Beijing Huajinghui Technology Ltd., China) was connected to the left electrode with an output voltage of 1.5 kV or 3 kV, whereas the other electrode was grounded. According to the formula $E=U/d$, the intensities of the electric field generated at both ends of the capillary were approximately 400 V/cm and 800 V/cm, which exceeded the starting electric field intensity of capillary electroosmosis (150 V/cm) [38]. Each test lasted for 30 min, and the EOF velocities of the different lubricants were calculated based on their moving volume. Each test was repeated

five times at room temperature (25 °C), and the average value was then recorded.

2.3 Friction and wear testing

The tribological tests were conducted on an MMW-1 multispecimen test system (Jinan Shijin Group-Co., Ltd., China). The tribological properties of the lubricants containing CTAB and SLI were compared with those of pure DI water under different testing conditions using a four-ball method (see Fig. 2(a)). The test conditions were as follows: at room temperature (25 °C); additive concentrations of 0.05, 0.1, 0.2, and 0.3 mM; rotational speeds of 600, 800, 1,000, and 1,200 rpm; and loads of 49, 98, and 147 N. The evaluation duration was 30 min. The steel balls employed in the tests were 12.7 mm in diameter and made of AISI 52100 steel with an HRC hardness of 59–61. The scratches on the friction interface shown in Fig. 2(b) were a half cylinder with a radius of ~1 μm. As a counterpart ball slid on it, a cylinder cavity was formed, which was approximately considered to be a capillary [1, 39, 40]. The change in the experimental parameters affected the morphology of the capillaries on the friction interface, thus influencing the penetration effect of the lubricants [5, 41]. Figure 2(c) presents a schematic of the friction capillary interface. A
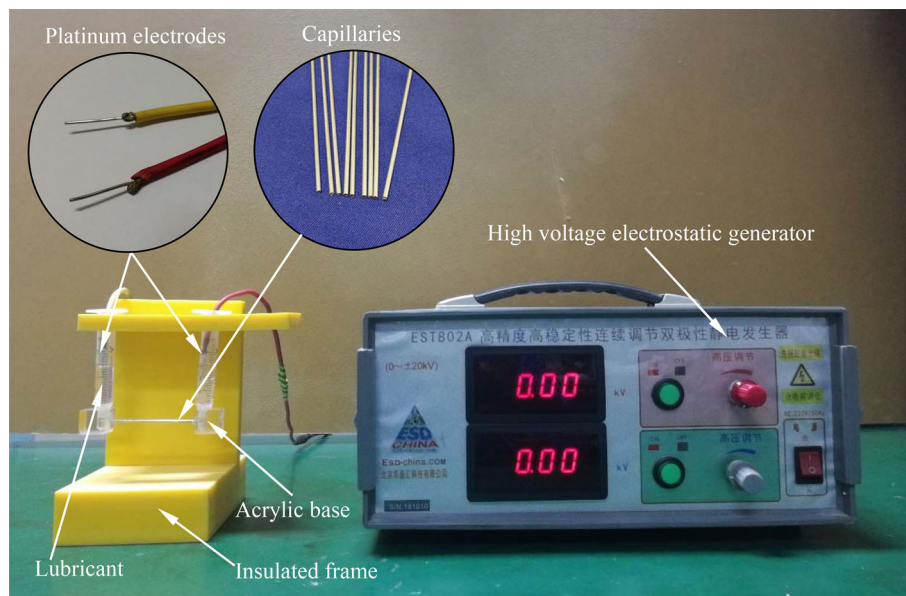

Fig. 1 Photograph of the device designed for measuring the EOF velocity of the lubricants.

strong radial electric field was generated due to the frictional electrification between the friction surfaces [19, 42], and the electrons emitted from the sliding contact were affected by this electric field, which generated a plasma [20, 22]. These above phenomena resulted in an axial self-excited electric field directed toward the closed end in the capillary. To analyze the chemical states and distribution of the chemical elements on the worn surfaces, additional ball-on-disk tests were performed. The steel balls used for these tests were the same as those for the four-ball tests, and the steel disks employed were φ32 mm × φ16 mm × 0.8 mm. They were made of AISI 52100 steel with an HRC hardness of 25–28. The tests were conducted at room temperature (25 °C), an additive concentration of 0.2 mM, a rotational speed of 800 rpm, and a load of 98 N; the test duration was 15 min. Before testing, the specimen holders and test balls/disks were dipped in acetone and cleaned in an ultrasonic bath for 10 min. Each test was repeated five times, and the average value was recorded. After each test, the disks and balls were cleaned in an ultrasonic bath. The wear scar diameters (WSDs) of the balls and the surface topographies of the disks were analyzed using a three-dimensional dynamic microscope system (VW-6000, Keyence, Japan). The worn surfaces of the balls and disks were examined using a scanning electron microscopy (SEM) system equipped with an

energy dispersive X-ray spectroscopy (EDS) (EVO18, Zeiss, Germany), and a Kratos AXIS Ultra DLD X-ray photoelectron spectrometer (Shimadzu Corporation, Japan) equipped with an Al $k\alpha$ radiation source (15 keV, 10 mA). The pass energy was 20 eV for fine scanning at a resolution of 0.3 eV, using the binding energy of adventitious carbon (284.8 eV) as a reference.

3 Results and discussion

3.1 Capillary electroosmosis properties

Due to the diameter limitation of commercial capillaries, it is difficult to investigate the electroosmosis properties of lubricants in small capillaries with an internal diameter of 1–2 μm [9]. Therefore, macroscopic capillaries with different diameters were used to comparatively investigate the EOF velocity of different solutions. Table 2 presents the measurements of the surface tensions and contact angles of DI water and lubricants with the two different surfactants, in which the results of the DI water were used as a comparison. We observed that the surface tensions and contact angles of the two kinds of lubricants were smaller than those of the DI water and decreased with increasing surfactant concentration. The EOF velocities of the lubricants containing CTAB and SLI under different conditions are depicted in Figs. 3(a) and
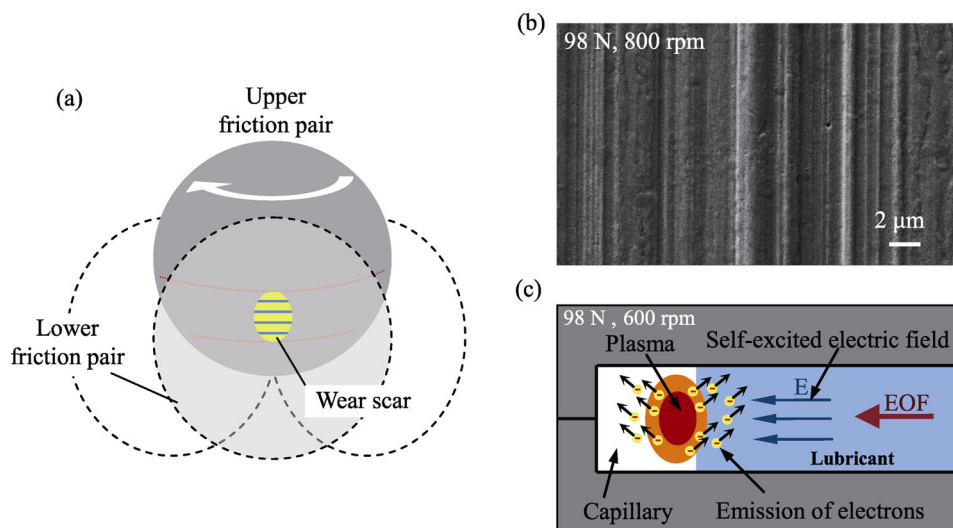

Fig. 2 (a) Schematic of the four-ball test. (b) Capillaries at the friction interface. (c) Schematic of the friction capillary interface.

3(b). The absolute values of the EOF velocities of both lubricants increased rapidly with the increase in CTAB and SLI concentrations under the same electric field strength. With an increase in the electric field intensity on both sides of the capillary, the absolute values of both EOF velocities increased obviously. For example, the EOF velocities of DI water in the capillary with an internal diameter of 0.9 mm were 0.65×10^{-4} and 0.77×10^{-4} μL/ms when the electric field intensities were 400 and 800 V/cm, respectively. It should also be noted that the EOF velocity increased with a decrease in the inner diameter of the capillary. The EOF velocities of the DI water under 800 V/cm in the capillaries with internal diameters of 0.5 and 0.9 mm were 1.09×10^{-4} and 0.77×10^{-4} μL/ms, respectively. This is mainly because the increased ratio of the side area to the cross-sectional area of the capillary can improve the EOF [29]. The maximum absolute values of the EOF velocities were recorded when the concentrations of CTAB and SLI reached 0.2 and 0.1 mM, respectively. This may be because the adsorption of electroosmotic additives molecules in the inner surface of the capillary tended to become saturated [43, 44].

As shown in Fig. 3, the direction of the EOF velocity is opposite to that of the electric field when CTAB lubricants are employed. This is mainly because the quaternary ammonium cationic group of the CTAB molecule is positively charged [45], and the CTAB molecules are firmly adsorbed on the inner wall of the capillary under the influence of the electrostatic attraction [46]. With the increase in CTAB concentration, the adsorption quantity of the CTAB molecules on the capillary wall increased gradually until the entire negatively charged internal wall of the capillary was covered, forming a single molecule adsorption layer. The density of negative charges on the capillary wall continued to decrease until it reached zero, and the EOF weakened until it disappeared eventually.

The second adsorption layer on the capillary walls was formed by the interaction of the hydrophobic chains in the CTAB molecules with the increased concentration of CTAB, as displayed in Fig. 4(a). Chen [38] suggested that when the CTAB concentration in the solution reaches 0.05 mM, the second

adsorption layer forms (at this time, the direction of the EOF began to reverse). With the increase in CTAB concentration, the rate of the reversed EOF increased. When the CTAB concentration reached 0.2 mM, the velocity of the EOF became stable, and the adsorption of CTAB molecules on the inner surface of the capillary reached saturation.

Additionally, we can observe from Fig. 3 that the direction of the EOF velocity is the same as that of the electric field when SLI lubricants are used. Under 400 V/cm, the EOF velocities of the SLI lubricant with 0.2 mM were 36.9% and 29.6% higher than those of the DI water with capillary inner diameters of 0.5 and 0.9 mm, respectively. Under 800 V/cm, the enhancing effect of the SLI lubricant with 0.2 mM on the EOF was stronger: the velocities were 54.5% and 36.7% higher than those of DI water, respectively. A possible reason for this phenomenon is that one SLI molecule has one cationic group containing nitrogen and two carboxylic acid anion groups. As shown in Fig. 4(b), the positive cationic groups of the SLI molecules are closely adsorbed on the negatively charged capillary walls and form an additional fixed layer under the electrostatic effect between the charges. The carboxylic acid anion groups remained in the solution and did not move with the movement of the solution. This condition doubled the negative charge on the capillary wall, resulting in the enhanced EOF [47].

Upon combining Table 2 with Fig. 3, it can be seen that when the surfactant concentration increased from 0.2 to 0.3 mM, although the surface tension and contact angle continued to decrease, the EOF velocity did not change significantly. This result indicates that the penetration of the lubricating fluid in the capillaries was mainly controlled by the EOF instead of electrowetting at such a low concentration of surfactant.

3.2   Tribological properties

3.2.1   *Tribological behaviors under different concentrations*

Figure 5 presents the variations in COF and WSD as a function of concentration when the lubricants containing CTAB and SLI are used. The performance

Table 2 Values of the contact angles and surface tensions for the three Different types of lubricants at various concentrations. The results achieved by DI water were used for comparison.

Lubricant		Surface tension γ (mN·m^{-1})	Contact angle θ (°)
0 mM	DI water	72.0	79.5
0.05 mM	CTAB	60.9	77.7
	SLI	61.7	77.3
0.1 mM	CTAB	58.3	75.6
	SLI	60.1	76.1
0.2 mM	CTAB	57.1	74.1
	SLI	58.2	74.3
0.3 mM	CTAB	54.9	72.1
	SLI	55.9	71.5
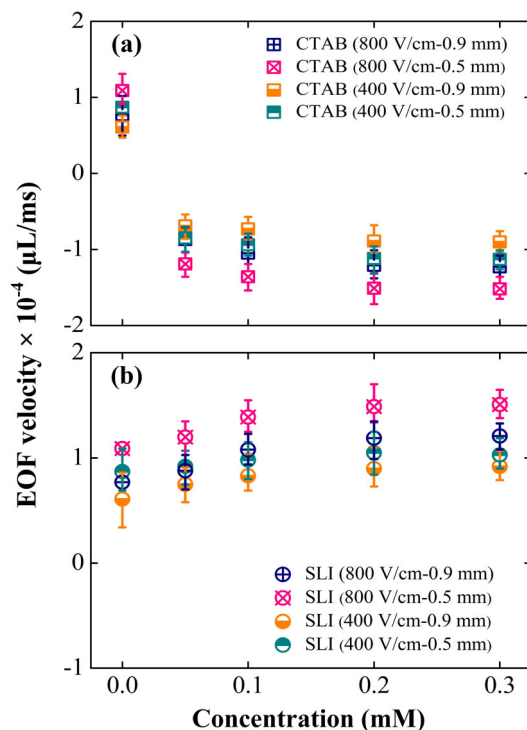
Fig. 3 Effect of electroosmotic additive type and concentration, capillary diameter, and electric field strength on EOF velocity. The values consistent with the direction of the electric field line are positive, and the test time is 30 minutes. The types of electroosmotic additives are (a) CTAB and (b) SLI.

achieved using DI water is also shown in Fig. 5 for comparison. The COFs and WSDs increased with increasing concentration of CTAB, and the highest friction increase was obtained when the concentration of CTAB reached 0.2 mM. The COF and WSD were

25.5% and 10.4% higher compared with those of DI water (0.289 in COF and 0.692 mm in WSD), respectively. This could be because CTAB might suppress the penetration of lubricants into the friction interface due to the changed EDL structure on the inner walls of the capillary, reducing the amount of lubricants participating in the anti-friction and anti-wear processes and consequently increasing the COF and WSD.

As illustrated in Fig. 5, the COFs and WSDs sharply decrease and then remain stable with increasing concentrations of SLI. When the concentration of SLI reached 0.1 mM, the best performance was recorded, in which the COF and WSD were 22.7% and 10.7% lower than those of DI water, respectively. These results suggest that the addition of SLI promotes the EOF toward the deeper friction interface, leading to more lubricants entering into the capillaries of the friction interface to participate in the anti-wear process, resulting in the reduction of the COF and WSD. However, when the concentration of electroosmotic additives continued to increase, the COFs and WSDs basically remain unchanged. This should be due to the saturation of the adsorption of CTAB and SLI molecules on the inner wall of the capillary [48].

Figure 6 displays the SEM images and EDS spectra of the worn surfaces of the friction balls under different lubrication conditions. In Fig. 6(a), a large number of deep furrows are clearly shown on the worn surface employing the CTAB lubricant, indicating severe abrasive wear. However, the furrows produced by the SLI lubricant were shallower, as presented in Fig. 6(c), suggesting a better anti-wear capacity. The EDS spectra detected within the dashed boxed areas on the worn surfaces show that the contents of Br on the worn surfaces are 0 wt%, and those of the Na element are 0.01–0.09 wt%. CTAB contains Br while SLI contains Na, suggesting that only very small amounts of the additives were involved in the lubrication process during the trials. In addition, the maximum mass fractions of CTAB and SLI in the electroosmotic suppressant lubricant and electroosmotic promoter lubricant are only 0.0109 wt% and 0.0112 wt%, respectively. Therefore, the lubricating performances
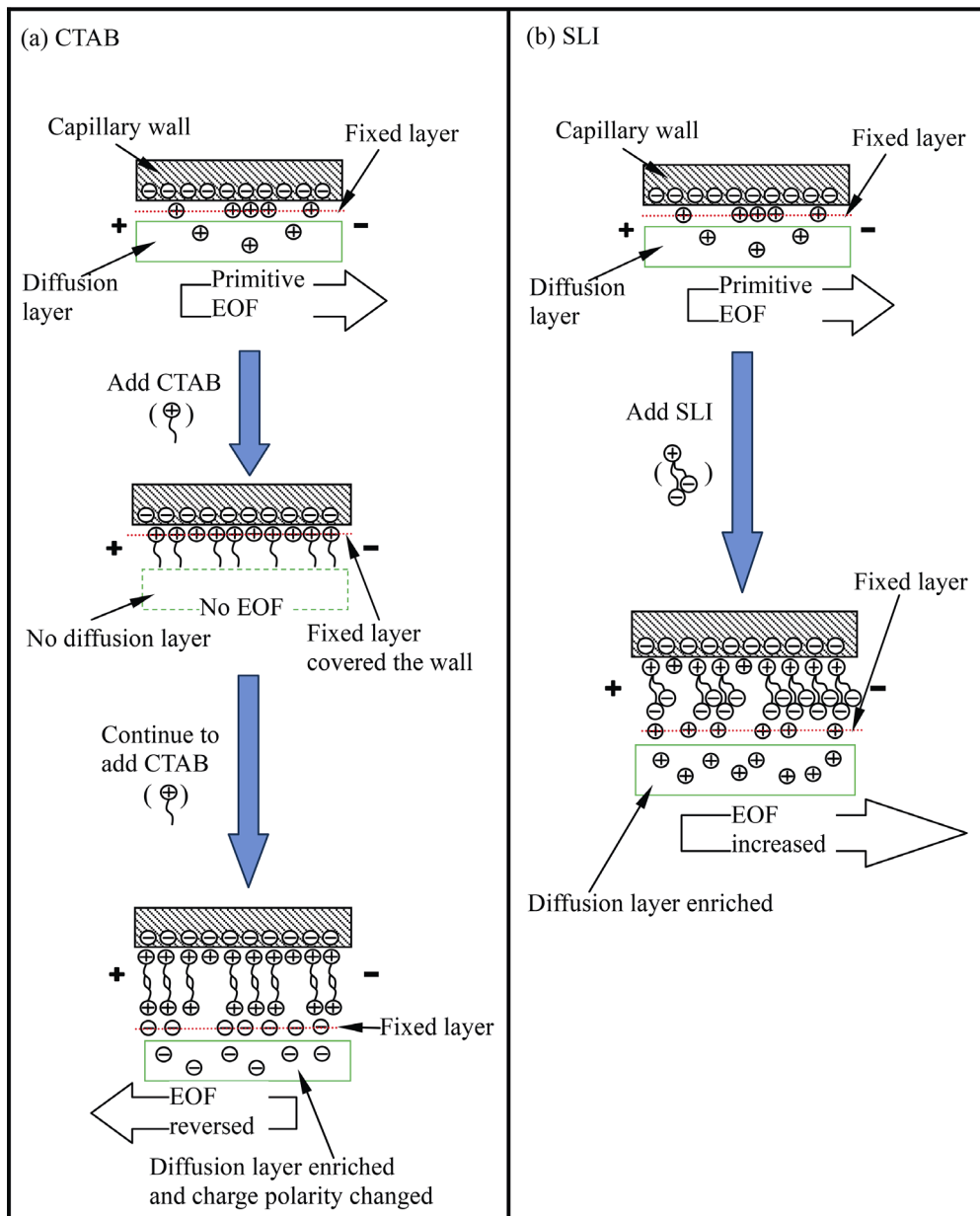
Fig. 4   Regulation mechanism of different electroosmotic additive molecules on EOF: (a) CTAB and (b) SLI.

of the electroosmotic additives themselves had little effect on the anti-friction and anti-wear performance of the lubricants. The improvement in the tribological performance of the lubricant may be mainly due to the amount of lubricant penetrating into the steel-on-steel sliding interface. In addition, the content of O on the worn surface using the SLI lubricant is higher than that of the other two cases, indicating that more oxygen is supplied to participate in the anti-wear process and form an oxide film on the worn surface. Additional details

are discussed in Section 3.3.

3.2.2   *Tribological behavior under different rotational speeds*

Figure 7 shows the WSD and COF as a function of rotational speed under the lubrication conditions of the electroosmotic suppressant and electroosmotic promoter; the results recorded under DI water are used for comparison. The COFs decreased rapidly, whereas the WSDs showed an opposite trend with increasing rotational speed. Huang et al. [49] found
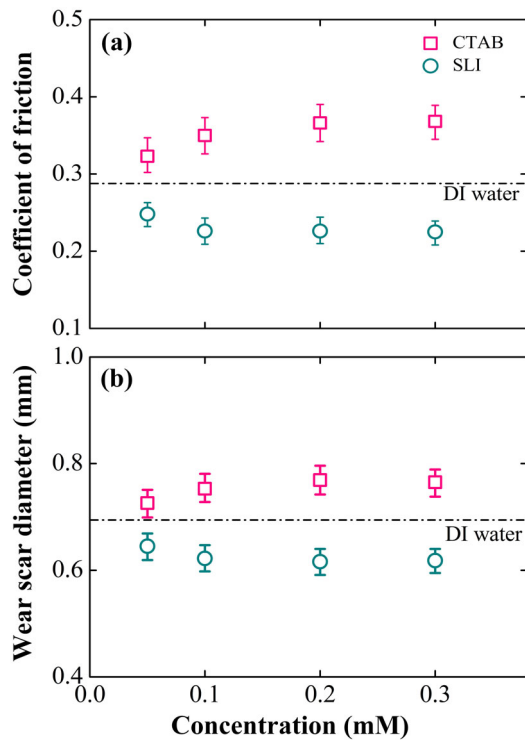
Fig. 5 Effect of electroosmotic additive concentration on (a) COFs and (b) WSDs for four-ball tests at 800 rpm and 98 N. The results obtained using DI water are used for comparison.

that the variations in the COF and wear rate of friction pairs were closely related to the contact condition of the friction pairs with varying sliding speed when they compared the anti-wear performance under minimum quantity lubrication (MQL) and electrostatic minimum quantity lubrication (EMQL) conditions at different test speeds. As indicated in Fig. 7, the COFs and WSDs lubricated by the SLI lubricant are comparatively lower than those lubricated by the CTAB lubricant at all rotational speeds. Compared with DI water (0.289), the use of SLI and CTAB lubricants could achieve a 22.5% reduction but a 25.5% increment in COF, respectively, when the rotational speed was 800 rpm. This may be mainly because the increase in rotating speed could result in severer contact, which increases the axial electric field strength at both ends of the capillary at the friction interface. The addition of SLI can promote more water and oxygen molecules penetrating the friction interface, which promote the formation of an oxide film, thus enhancing the tribological performance. However, the addition of CTAB suppresses the penetration of water into
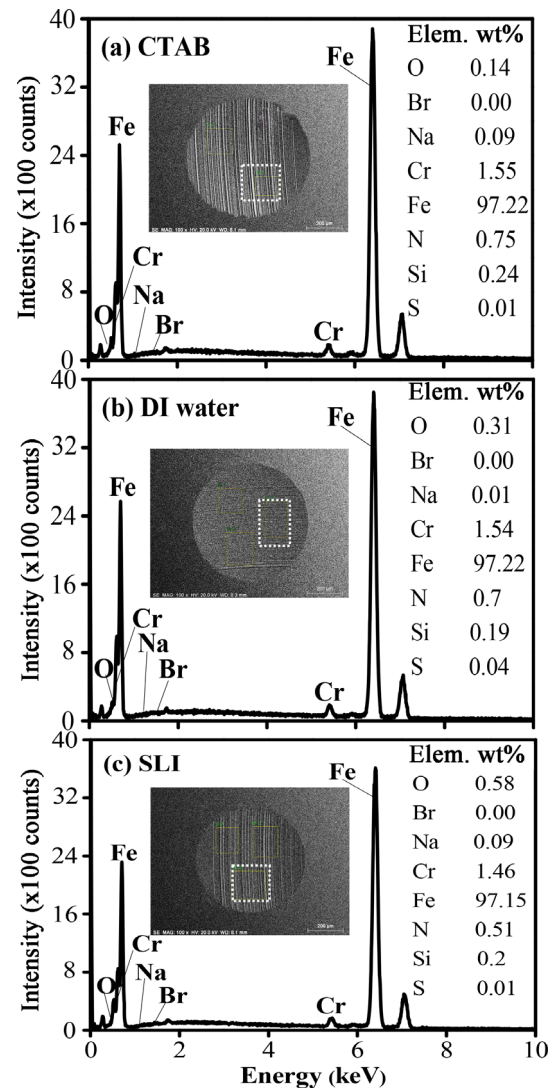

Fig. 6 SEM images of the worn surfaces lubricated with (a) CTAB, (b) DI water, and (c) SLI, and EDS spectra detected at the dashed boxed areas on the worn surfaces of the SEM images at 0.2 mM electroosmotic additive concentration, 800 rpm, and 98 N.

the friction interface, leading to a worse tribological performance.

3.2.3 Tribological behaviors under different applied loads

Figure 8 depicts the COF and WSD as a function of the applied load under different lubrication conditions using the results recorded under DI water as comparison. The COFs and WSDs of the SLI lubricant are lower than those of the CTAB lubricant under different loads. The capability of SLI in promoting the lubricant into the capillaries of the
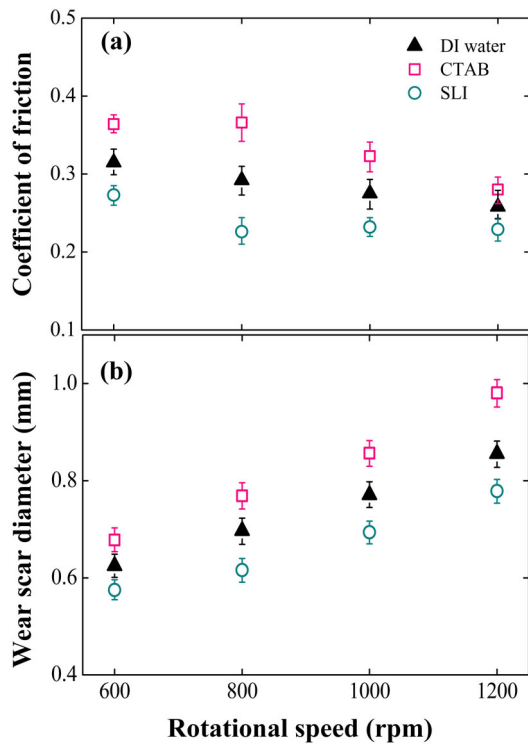
Fig. 7 Effect of rotational speed on (a) COFs and (b) WSDs for four-ball tests at 0.2 mM electroosmotic additive concentration and 98 N.

Fig. 8 Effect of applied load on (a) COFs and (b) WSDs for four-ball tests at 0.2 mM electroosmotic additive concentration and 800 rpm.

friction interface is remarkable based on the reduced COFs and WSDs in comparison with CTAB. As can be seen from Fig. 8, the COF initially decreases and then increases with increasing applied load for both SLI lubricant and DI water cases. It is possible that the increase in the applied load leads to an increase in wear surface roughness, leading to the increase in the diameter of the capillaries on the worn surface, resulting in a lower EOF [40]. As explained earlier, the axial electric fields at both ends of the capillary were enhanced by the production of a strong plasma in the friction zone when the applied load increased. A stronger electric field accelerates the EOF of lubricants and promotes lubricant penetration into the contact interface. Moreover, it can bring more oxygen molecules into the contact area to form an anti-wear layer, thus achieving a better tribological performance [16]. However, when the load is further increased, the excessive pressure between the friction pairs may cause the anti-wear layer formed on the worn surface to peel off quickly [50], increasing the wear of the friction pairs, as reflected by the larger values
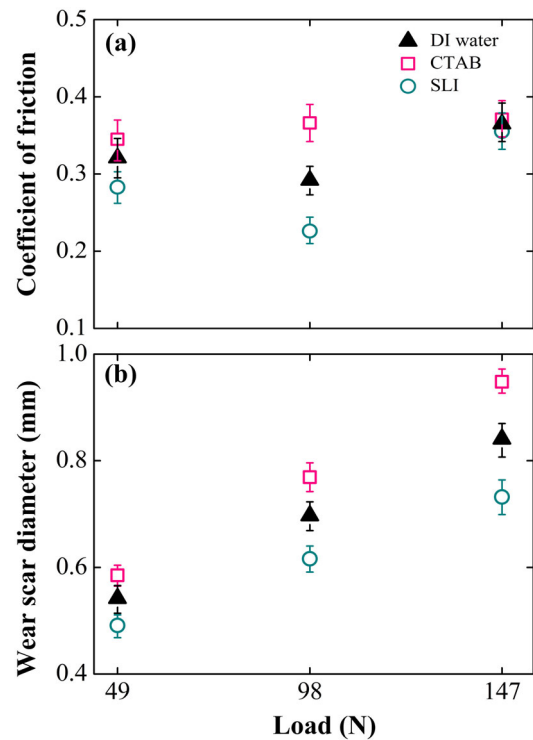
of COF.

3.2.4 Surface topography

Figure 9 compares the overall characteristics of the SEM and optical micrographs of the worn surfaces under all conditions. It is evident from Figs. 9(a, c, e) that the quality of the worn surfaces using the SLI lubricant was better than those using the DI water and CTAB lubricants, which is consistent with the relevant friction and wear behaviors. A possible explanation for this result may be that more lubricant penetrated the interface of the friction pair and formed an oxide layer on the worn surface. The oxide layer could effectively protected the worn surface of the friction pairs and minimize scratches, leading to a better surface quality. Regarding the experimental evidence on the SEM micrographs shown in Figs. 9(b, d, f), typical characteristics of irregular lamellar wear debris are clearly obtained on the surfaces in all cases. Moreover, even flake shedding occurred under the DI water and CTAB lubrication conditions, which demonstrated that adhesion and plastic deformation
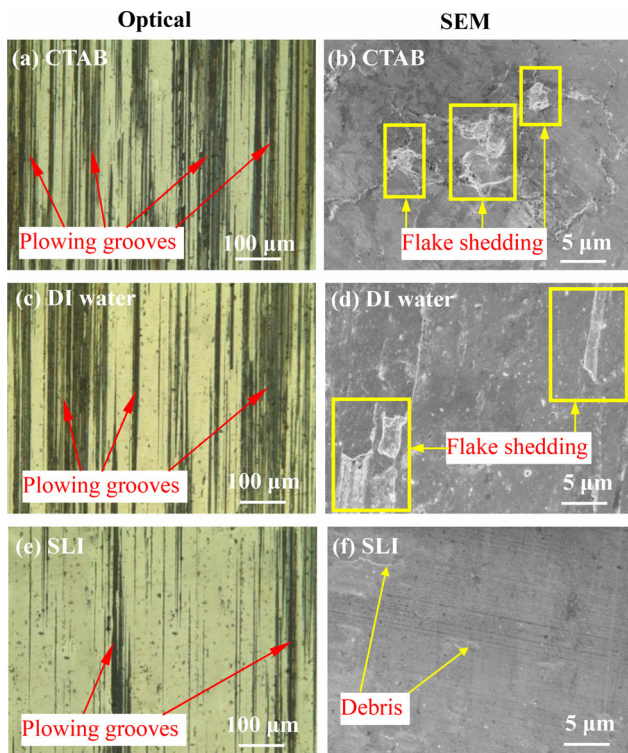
Fig. 9 Optical and SEM micrographs of the worn surfaces lubricated with (a, b) CTAB lubricant, (c, d) DI water, and (e, f) SLI lubricant at 0.2 mM concentration, 800 rpm, and 98 N.

took place [51]. In addition, there are plowing grooves with different degrees on the worn surfaces under all lubrication conditions. Therefore, it appears that the wear mechanism for all lubricants is generally dominated by the combination of adhesive wear, abrasive wear, and plastic deformation.

3.3 XPS analysis of worn surfaces

To investigate the effect of the electroosmotic additives on the penetrability of the lubricating fluid at the friction interface, the worn disk surfaces were analyzed by XPS. Figure 10 provides the O 1s and Fe 2p XPS spectra on the raw AISI 52100 steel and worn surfaces lubricated by the CTAB, SLI, and DI water lubricants. XPSPEAK 41 was employed to fit the spectral elements, and Table 3 lists the relative areas of FeO, Fe_2O_3 and Fe_3O_4, and FeOOH on the AISI 52100 steel and worn surfaces.

For the AISI 52100 steel surface, the peaks in the O 1s spectra illustrated in Fig. 10(a) are related to the absorbed Fe–O bonds. The 710.7 and 725.1 eV binding energies, probed in the Fe 2p spectrum

presented in Fig. 10(b), are attributed to Fe $2p_{3/2}$ and Fe $2p_{1/2}$ for Fe_2O_3 and Fe_3O_4, but the 706.8 eV binding energy may be assigned to Fe $2p_{3/2}$ for Fe [37]. Furthermore, the peak at ~719.7 should be ascribed to the satellite peak of Fe $2p_{3/2}$ for Fe_2O_3 and Fe_3O_4 [52].

For the DI water lubrication condition, new peaks are detected in the Fe 2p spectra, as shown in Fig. 10(b). The ~712.7 eV binding energy is attributed to the Fe $2p_{3/2}$ for FeOOH, indicating that there is a chemical reaction between DI water and Fe at the friction interface [53]. In addition, the peaks at 709.9 and 724.1 eV are attributed to the Fe $2p_{3/2}$ and Fe $2p_{1/2}$ for FeO [36]. According to the observations above, we can infer that an oxide layer is formed on the contact interface with DI water lubrication.

For the CTAB lubricant, the respective peaks at 531.2 eV and ~712.7 eV correspond to the FeOOH also existing on the O 1s and Fe 2p spectra. Compared with that by DI water, the peaks assigned to the Fe $2p_{3/2}$ and Fe $2p_{1/2}$ for FeO obviously weakened, and the relative areas of FeOOH in addition to Fe_2O_3 and Fe_3O_4 detected on the worn surface produced with the CTAB lubricant are lower than those of DI water (see Table 3). This indicates that only a preliminary chemical reaction took place on the worn surface and the oxide film formed on the worn surface was thin. This is because the CTAB molecules formed a second adsorption layer on the capillary wall under the action of the electrostatic force between charges, reducing the EOF and causing less lubricating fluid to participate in the anti-wear process.

For the SLI lubricant, the types of peaks detected on the worn surface are the same as those of DI water. However, the relative areas of FeOOH and Fe_2O_3&Fe_3O_4 detected on the worn surface produced by the SLI lubricant are higher than those of DI water (see Table 3). This demonstrated that the penetrating capacity of the lubricants into the contact interface was improved when the electroosmotic promoter was employed, and more oxygen was supplied to produce an oxide film on the worn surface [9]. The existence of a higher oxygen content on the worn disc surface caused the Fe^0 and Fe^{+2} to
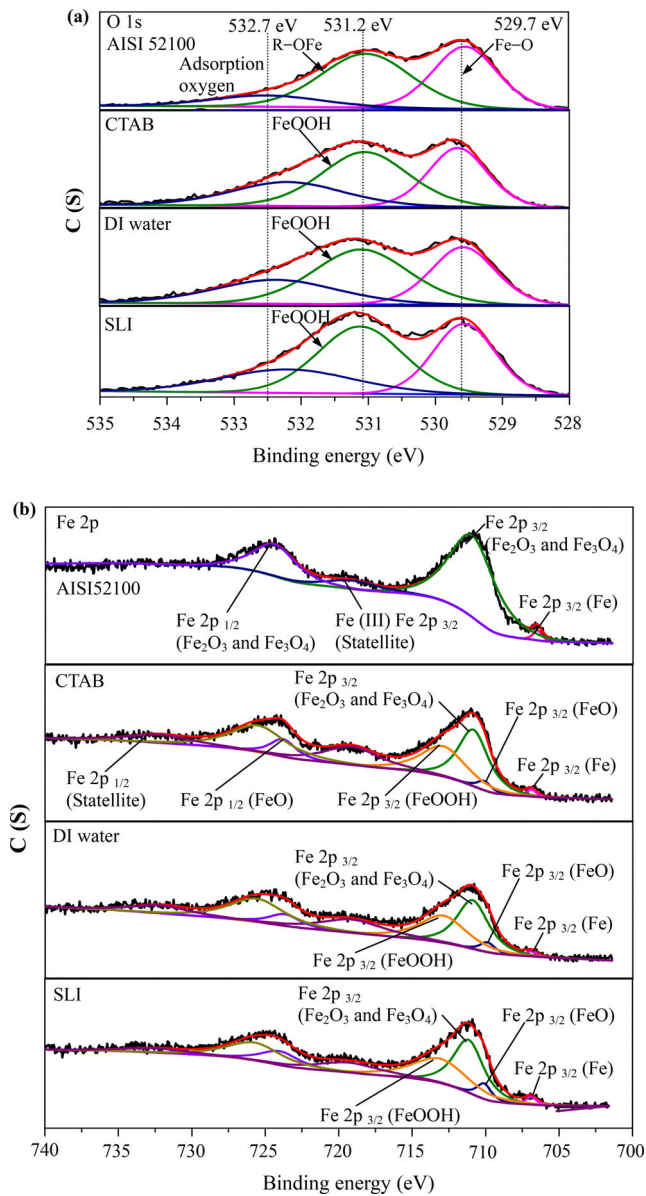
Fig. 10 XPS spectra of (a) O 1s and (b) Fe 2p on the AISI 52100 steel surface and the worn surfaces lubricated with CTAB, DI water, and SLI lubricants.

transform into Fe^{+3} [52].

Based on the above findings, a penetration model of the friction region under different lubricants is illustrated in Fig. 11. The penetration property of DI water into the capillaries of the friction interfaces differed under the addition of different electroosmotic additives, leading to a different thickness oxide film generated on the friction interfaces, which consisted of Fe_2O_3&Fe_3O_4 and FeOOH. The contact on the friction interface was changed from steel on steel to film on film owing

Table 3 Relative areas of FeO, Fe_2O_3 and Fe_3O_4, and FeOOH on AISI 52100 steel and worn surfaces produced using the CTAB, DI water, and SLI lubricants.

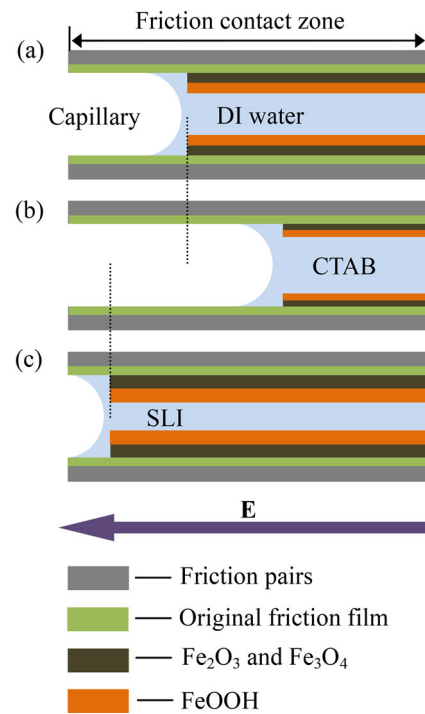|	Relative area (%)		
	FeO	Fe_2O_3 and Fe_3O_4	FeOOH
AISI 52100	—	66.37	—
CTAB	1.99	25.6	20.38
DI water	2.48	26.1	21.18
SLI	4.02	28.54	23.66

Fig. 11 Schematic of the lubricating layer under (a) DI water, (b) CTAB, and (c) SLI lubrication conditions.

to the oxide film formed on the friction interfaces [54]. As shown in Fig. 11, the addition of SLI promoted the penetration of DI water into the capillary, which accelerated the formation of an oxide film on the contact interface, leading to the enhanced tribological performance of the steel-on-steel friction interface.

4   Conclusions

In this study, the EOF velocities of pure DI water, DI water with CTAB, and DI water with SLI in steel capillaries with different inner diameters were verified by measurements under different electric fields. The lubrication properties of these

three types of lubricants were investigated by four-ball experiments of a steel-on-steel sliding interfaces. The results showed that the tribological performance of these lubricants were related to their EOF velocities. Furthermore, the lubrication mechanism of DI water as the base lubricant added with an electroosmotic suppressant (CTAB) and an electroosmosis promoter (SLI) was also revealed. The conclusions obtained are as follows:

1) The penetration property of DI water in the capillaries can be modified by adding electroosmotic additives. In addition, the EOF velocity is directly proportional to the electric field intensity and inversely proportional to the inner diameter of the capillary.

2) Owing to the existence of one cationic group containing nitrogen and two carboxylic acid anion groups in one SLI molecule, the wall charges of the capillary doubled, resulting in a stronger EOF directed to the deeper contact region. With the increase in CTAB, the polarity of the wall charges was reversed (from "negative" to "positive") because of the adsorption of the quaternary ammonium cationic group in the CTAB on the negatively charged capillary wall; thus, the direction of EOF was finally reversed. In general, compared with pure DI water, the SLI lubricant can reduce the COF and WSD, whereas the CTAB lubricant exhibits an opposite behavior.

3) The rotational speed and applied load have great influences on the friction and wear performances because changes in the rotational speed and applied load can affect both the intensity of electron emission and inner diameter of the capillaries on the friction interface. The most significant difference in lubrication performance with different lubricants was observed when the rotating speed was 800 rpm and the applied load was 98 N.

4) The addition of SLI can promote lubricant penetration into the capillaries of the contact zone and is beneficial to form a thicker oxide layer on the friction interface. The friction contact is transformed from the original steel to steel into film to film, which reduces the COFs and WSDs.

In the next research, we plan to investigate the characteristics of EDLs and electron emission capacities of different friction interfaces in lubricants to establish a capillary electroosmosis kinetic model of lubricants at friction interfaces.

References

[1] Zhao J H, Yang G B, Zhang C L, Zhang Y J, Zhang S M, Zhang P Y. Synthesis of water-soluble Cu nanoparticles and evaluation of their tribological properties and thermal conductivity as a water-based additive. *Friction* **7**(3): 246–259 (2019)

[2] Godlevski V A, Volkov A V, Latyshev V N, Maurin L N. The kinetics of lubricant penetration action during machining. *Lubricat Sci* **9**(2): 127–140 (1997)

[3] Mane S, Joshi S S, Karagadde S, Kapoor S G. Modeling of variable friction and heat partition ratio at the chip-tool interface during orthogonal cutting of Ti-6Al-4V. *J Manuf Process* **55**: 254–267 (2020)

[4] Behera B C, Chetan, Setti D, Ghosh S, Rao PV. Spreadability studies of metal working fluids on tool surface and its impact on minimum amount cooling and lubrication turning. *J Mater Process Tech* **244**: 1–16

(2017)

[5] Hwang J. Direct observation of fluid action at the chip-tool interface in machining. *Int J Precis Eng Manuf* **15**(10): 2041–2049 (2014)

[6] Hwang J, Chandrasekar S. Contact conditions at the chip-tool interface in machining. *Int J Precis Eng Manuf* **12**(2): 183–193 (2011)

[7] Bierla A, Fromentin G, Minfray C, Martin J M, Le Mogne T, Genet N. Mechanical and physico-chemical study of sulfur additives effect in milling of high strength steel. *Wear* **286–287**: 116–123 (2012)

[8] Zheng W J, Pei H J, Wang G C, Shen C G. A theoretical investigation on the capillary model of lubricant penetration. *Adv Mat Res* **383–390**: 3871–3875 (2011)

[9] Liu J Y, Liu H P, Han R D, Wang Y. The study on lubrication action with water vapor as coolant and lubricant in cutting ANSI 304 stainless steel. *Int J Mach Tool Manuf* **50**(3): 260–269 (2010)

[10] Xu X F, Feng B H, Huang S Q, Luan Z Q, Niu C C, Lin J B, Hu X D. Capillary penetration mechanism and machining characteristics of lubricant droplets in electrostatic minimum quantity lubrication (EMQL) grinding. *J Manuf Proc* **45**: 571–578 (2019)

[11] Ciniero A, Le Rouzic J, Baikie I, Reddyhoff T. "The origins of triboemission-Correlating wear damage with electron emission". *Wear* **374–375**: 113–119 (2017)

[12] Kharlamov V F. Effect of the electric field on electron chemiemission from a semiconductor surface. *Tech Phys* **55**(6): 893–895 (2010)

[13] Sokolowski-Tinten K, Ziegler W, von der Linde D, Siegal M P, Overmyer D L. Short-pulse-laser-induced optical damage and fracto-emission of amorphous, diamond-like carbon films. *Appl Phys Lett* **86**(12): 121911 (2005)

[14] Banerjee A, Jiang C C, Lohiya L, Yang Y, Lu Y. Fracto-emission in lanthanum-based metallic glass microwires under quasi-static tensile loading. *J Appl Phys* **119**(15): 155102 (2016)

[15] Wang W Q, Ji L, Li H X, Zhou H D, Ju P, Chen J M. Enhancing field electron emission behavior and mechanical properties of hydrogenated amorphous carbon films by incorporating vertically aligned carbon nanowires via facile reactive magnetron sputtering. *J Alloy Compd* **784**: 463–470 (2019)

[16] Govindaraj J, Subbiah S. Charged-particle emissions during material deformation, failure and tribological interactions of machining. *J Tribol* **141**(3): 031101 (2019)

[17] Nakayama K, Bou-Said B, Ikeda H. Tribo-electromagnetic phenomena of hydrogenated carbon films-Tribo-electrons, -ions, -photons, and -charging. *J Tribol* **119**(4): 764–768 (1997)

[18] Nakayama K, Fujimoto T. The energy of electrons emitted from wearing solid surfaces. *Tribol Lett* **17**(1): 75–81 (2004)

[19] Chiou Y C, Chang Y P, Lee R T. Tribo-electrification mechanism for self-mated metals in dry severe wear process: Part I. Pure hard metals. *Wear* **254**(7–8): 606–615 (2003)

[20] Nakayama K, Nevshupa R A. Effect of dry air pressure on characteristics and patterns of tribomicroplasma. *Vacuum* **74**(1): 11–17 (2004)

[21] Nakayama K, Nevshupa R A. Plasma generation in a gap around a sliding contact. *J Phys D Appl Phys* **35**(12): L53-L56 (2002)

[22] Nakayama K. Mechanism of triboplasma generation in oil. *Tribol Lett* **41**(2): 345–351 (2011)

[23] Ren C L, Li D Q. Improved understanding of the effect of electrical double layer on pressure-driven flow in microchannels. *Anal Chim Acta* **531**(1): 15–23 (2005)

[24] Lee J, Moon H, Fowler J, Schoellhammer T, Kim C J. Electrowetting and electrowetting-on-dielectric for microscale liquid handling. *Sensor Actuat A Phys* **95**(2–3): 259–268 (2002)

[25] van der Wouden E J, Heuser T, Hermes D C, Oosterbroek R E, Gardeniers J G E, van den Berg A. Field-effect control of electro-osmotic flow in microfluidic networks. *Colloid Surf A Physicochem Eng Aspects* **267**(1–3): 110–116 (2005)

[26] Li L, Wang X Y, Pu Q S, Liu S R. Advancement of electroosmotic pump in microflow analysis. *Anal Chim Acta* **1060**: 1–16 (2019)

[27] Sázelová P, Kasicka V, Koval D, Prusík Z, Fanali S, Aturki Z. Control of EOF in CE by different ways of application of radial electric field. *Electrophoresis* **28**(5): 756–766 (2007)

[28] Razunguzwa T T, Timperman A T. Fabrication and characterization of a fritless microfabricated electroosmotic pump with reduced pH dependence. *Anal Chem* **76**(5): 1336–1341 (2004)

[29] You H Y. *Electroosmosis and Its Application in Chromatography*. Beijing: Science Press, 2010.

[30] Guan Q, Noblitt S D, Henry C S. Electrophoretic separations in poly(dimethylsiloxane) microchips using a mixture of ionic and zwitterionic surfactants. *Electrophoresis* **33**(2): 379–387 (2012)

[31] Bekri S, Leclercq L, Cottet H. Influence of the ionic strength of acidic background electrolytes on the separation of proteins by capillary electrophoresis. *J Chromatogr A* **1432**: 145–151 (2016)

[32] Chen L X, Ma J P, Guan Y F. An electrosmotic pump for packed capillary liquid chromatography. *Microchem J* **75**(1): 15–21 (2003)

[33] Wang L, Wu J K. Flow behavior in microchannel made

of different materials with wall slip velocity and electro-viscous effects. *Acta Mech Sin* **26**(1): 73–80 (2010)

[34] Zhong W, Chen Y F. Hydrodynamic analysis of electroosmotic flow in micropump. *Chin J Mech Eng* **40**(2): 73–77 (2004)

[35] Jiang C Y, Liu G, Zhang D H, Xu X P. Research on the microfluidics control method based on the EOF technology. *Mat Sci Forum* **532–533**: 65–68 (2006)

[36] Huang S Q, Lv T, Wang M H, Xu X F. Enhanced machining performance and lubrication mechanism of electrostatic minimum quantity lubrication-EMQL milling process. *Int J Adv Manuf Tech* **94**(1–4): 655–666 (2018)

[37] Huang S Q, Wang Z, Yao W Q, Xu X F. Tribological evaluation of contact-charged electrostatic spray lubrication as a new near-dry machining technique. *Tribol Int* **91**: 74–84 (2015)

[38] Chen Y. *Capillary Electrophoresis Technology and Its Application*. Beijing: Chemical Industry, 2006

[39] Brinksmeier E, Riemer O. Measurement of optical surfaces generated by diamond turning. *Int J Mach Tool Manu* **38**(5–6): 699–705 (1998)

[40] Hu Z M, Dean T A. A study of surface topography, friction and lubricants in metalforming. *Int J Mach Tool Manuf* **40**(11): 1637–1649 (2000)

[41] Jia D Z, Li C H, Zhang Y B, Yang M, Zhang X P, Li R Z, Ji H J. Experimental evaluation of surface topographies of NMQL grinding ZrO2 ceramics combining multiangle ultrasonic vibration. *Int J Adv Manuf Tech* **100**(1–4): 457–473 (2019)

[42] Nakayama K, Hashimoto H. Triboemission of charged particles and photons from wearing ceramic surfaces in various hydrocarbon gases. *Wear* **185**: 183–188 (1995)

[43] Gáspár A, Gábor L. Study of quantitative analysis of traces in low-conductivity samples using capillary electrophoresis with electrokinetic injection. *J Chromatogr A* **1091**(1–2): 163–168 (2005)

[44] Teixeira W S R, Santos M S F, Gruber J, Gutz I G R, Lopes F S. Determination of neutral diols and carboxylic acids formed during glycerol electrooxidation by capillary electrophoresis with dual

(CD)-D-4. *Talanta* **178**: 1040–1045 (2018)

[45] Wang W, Zhao L, Zhang J R, Zhu J J. Indirect amperometric measurement of electroosmotic flow rates and effective mobilities in microchip capillary electrophoresis. *J Chromatogr A* **1142**(2): 209–213 (2007)

[46] Gao T, Li C H, Zhang Y B, Yang M, Jia D Z, Jin T, Hou Y L, Li R Z. Dispersing mechanism and tribological performance of vegetable oil-based CNT nanofluids with different surfactants. *Tribol Int* **131**: 51–63 (2019)

[47] Tyle P, Frank S G. Penetration temperatures of aqueous sodium lauriminodipropionate solutions into solid phytosterols. *J Pharm Sci* **80**(2): 201 (1991)

[48] Wojciechowski K, Linek K. Anion selectivity at the aqueous/polymeric membrane interface: A streaming current study of potentiometric Hofmeister effect. *Electrochim Acta* **71**: 159–165 (2012)

[49] Huang S Q, Wang Z, Yao W Q, Xu X F. Tribological evaluation of contact-charged electrostatic spray lubrication as a new near-dry machining technique. *Tribol Int* **91**: 74–84 (2015)

[50] Ferreira R O, Galvani G B, Tertuliano I S, Rodrigues A C P, Azevedo C R F. Characterization and evolution of the coefficient of friction during pin on disc tribotest: Comparison between C10200 Cu, AA6082-T6 Al and C36000 brass pins under varying normal loads. *Tribol Int* **138**: 403–414 (2019)

[51] She D S, Yue W, Du Y J, Fu Z Q, Wang C B, Liu J J. Vacuum tribological properties of titanium with a nanocrystalline surface layer. *Tribol Lett* **57**(1): 1 (2015)

[52] Yamashita T, Hayes P. Analysis of XPS spectra of Fe^{2+} and Fe^{3+} ions in oxide materials. *Appl Surf Sci* **254**(8): 2441–2449 (2008)

[53] Liu J Y, Han R D, Zhang L, Guo H B. Study on lubricating characteristic and tool wear with water vapor as coolant and lubricant in green cutting. *Wear* **262**(3–4): 442–452 (2007)

[54] Gao C P, Fan S G, Zhang S M, Zhang P Y, Wang Q H. Enhancement of tribofilm formation from water lubricated PEEK composites by copper nanowires. *Appl Surf Sci* **444**: 364–376 (2018)

Bohua FENG. He received his bachelor degree in mechanical engineering in 2016 from Zhijiang College of Zhejiang University of Technology, Hangzhou, China. Then, he is a Ph.D. student in the Key Lab of Special Purpose Equipment and Advanced Manufacturing Technology, Ministry of Education & Zhejiang Province, Zhejiang University of Technology. His research interests include tribology, ultra precision machining, and green manufacturing technology.

Xuefeng XU. He received his M.S. degree in specialty of precision machinery and testing from Shanghai University of Science and Technology, China, in 1990. And he received his Ph.D. degree in mechanical and electronic engineering from Zhejiang University of Technology, China, in 2010. He has been engaged in teaching and research in the field of mechanical manufacturing at Zhejiang University of Technology since 1992. His current position is a professor and the deputy director of the Key Lab of Special Purpose Equipment and Advanced Manufacturing Technology, Ministry of Education & Zhejiang Province. His research areas cover the tribology, green manufacturing technology, and precision and special processing technology.

Effect of electroosmosis on lubricant penetration at the tool–chip interface

Bohua Feng [a,b], Zhiqiang Luan [a,b], Ruochong Zhang [a,b], Yu Xia [a,b], Weiqiang Yao [a,b], Jiawei Liu [a,b], Yaliang Ma [a,b], Xiaodong Hu [a,b,*], Xuefeng Xu [a,b,*]

[a] *College of Mechanical Engineering, Zhejiang University of Technology, Hangzhou 310014, China*
[b] *Key Laboratory of Special Purpose Equipment and Advanced Processing Technology, Ministry of Education and Zhejiang Province, Zhejiang University of Technology, Hangzhou 310023, China*

ARTICLE INFO

ABSTRACT

Conventional microcapillary lubrication theories explain lubricant penetration into capillaries at the tool–chip interface under the action of atmospheric pressure and capillary force without considering the electrokinetic effect caused by triboelectrification. In this study, the effect of electroosmosis on the penetration of water-based cutting fluid at the tool–chip interface of a turning process was investigated for the first time. An ionic adsorption model was proposed to adjust the zeta potential of different tool and workpiece materials in fluids, and a self-excited electric field at the tool–chip interface was obtained using an exoelectron emission test. The electroosmotic force related to the zeta potential and electric field intensity can regulate electrically driven fluid penetration. Cutting tests with a fixed self-excited electric field indicated that the cutting force obtained using a higher zeta potential fluid was lower than that obtained using deionized water and reversed zeta potential fluids (e.g. significant declines of 31.1 % and 44.3 % in AISI 304 turning). Moreover, scanning electron microscopy and energy dispersive X-ray spectroscopy analyses on the worn tool edges produced using the above fluids indicated a transfer from adhesive wear to micro breakage, which explains the positive correlation between penetration and zeta potential, owing to an elevated electroosmosis effect. The results presented in this paper are significant for understanding the influence of the electroosmosis effect on lubricant penetration to perfect the microcapillary lubrication theory and provide a reference for formulating metal working fluids.

1. Introduction

During machinery operations, cutting fluids are applied to reduce friction at the tool–workpiece interface, ensure the surface quality of the machined workpiece, and prolong the tool life (Huang et al., 2021). To reduce friction and heat, fluids are applied in the contact zone between the processed material and tool (Li et al., 2017). During the grinding of a nickel-based alloy lubricated with different cutting fluids, Guo et al. (2017) observed that physicochemical properties of the lubricating fluid that penetrated the machining contact zone demonstrated a decisive influence on its lubrication performance. Gao et al. (2021) developed a material removal mechanism model of a carbon fibre-reinforced polymer (CFRP) using a single grain in the grinding process; they observed that the good penetration and spreading effect of the lubricating fluid on the grain–fibre contact surface could effectively reduce the machining force and friction coefficient and significantly improve the machinability of CFRPs. Cui et al. (2021) and Liu et al. (2021) outlined the

machinability of difficult-to-cut aerospace materials using minimum quantity lubrication (MQL) and cryogenic minimum quantity lubrication (CMQL) techniques, and found that the improvement of the penetrability of the cutting fluid in the machining contact zone could significantly reduce the cutting force and improve the tool life and the surface quality of the workpiece. Wang et al. (2020) demonstrated that using an ultrasonic vibration-assisted technology could improve the penetration of fluids into the tool-chip and workpiece interfaces, resulting in a satisfactory machining performance. Godlevski et al. (1997) established four penetration models of cutting fluids and demonstrated that the fluid action operated primarily through lubricant penetration at the tool–chip boundary through a dynamic network of interface capillaries under the influence of atmospheric pressure and capillary forces. Gerth et al. (2014) established a cutting zone contact model to study the contact formed between the tool and chip. They observed that the fluid could reduce the adhesive bond distance between the tool and chip surface in the secondary shear zone to decrease the

shear force. Thimm et al. (2021) proposed a newly developed experimental test setup based on optical measurements to determine the chip speed and maximum shear strain rate of AISI 1045 steel. The results indicated that fissures in the chips serve as alternative penetration access points for fluids, through which energy dissipation is elevated in the primary shear zone. In addition to the capillary lubrication theory mentioned above, Podgaetsky (2018) stated that the Rehbinder effect facilitates the separation of the workpiece material through the interaction of additives and microcracks; Yamada et al. (2021) claimed that the Marangoni effect creates a capillary force and drives the fluid away from the highest temperature zones, resulting in anti-penetration. While these detailed mechanisms of fluid penetration during machining operations address pressure-driven and surface-tension-driven effects, the authors propose a novel electrokinetic penetration effect caused by the triboelectrification phenomenon in the cutting process to perfect the capillary lubrication theory.

For the cutting process, Govindaraj and Subbiah (2019) conducted a comprehensive study on the electrical properties of materials. The results indicated that the workpiece undergoes shear and fracture-based failures in its primary shear zone and suffers high-contact-stress tribological interactions in its primary and secondary friction zones between the tool, chip, and machined surface, resulting in triboelectrification and charged particle emission. Wang et al. (2020) studied the electrification and charge transfer between polymers and metals. They observed that the degree of triboelectrification is affected by the difference in the work function of the tool and processing material, material transfer, or material defects (e.g. vacancies, microcracks, etc.). Olufayo and Kadernani (2014) summarized previous experimental studies and concluded that the triboelectrification potential generated by friction is related to the resistivity of the material, and this potential could be detected up to 1 kV by turning polymer materials with a diamond tool. Chang et al. (2007) studied the triboelectrification between metals, and the results indicated that the triboelectrification potential of the iron (disc)–carbon steel (pin) is tens of microvolts, and the charge polarity of the pin changes from random to negative polarity with an increase in the carbon content. Nakayama and Yagasaki (2019) performed an experiment and concluded that the triboelectrification potential can produce a strong radial electric field in the slit of the contact pair, and the excitation of frictional exoelectrons via an electron avalanche ultimately generates triboplasma. Molina et al. (2001) and Nakayama and Fujimoto (2004) conducted electron detection tests. The intensity of the triboemission electron is frequently measured using a channel electron multiplier under vacuum or special atmospheric conditions, and the emission intensity of the material follows the given order: insulator > semiconductor > conductor. Nakayama (1994) scratched various solids with a diamond stylus under boundary lubrication conditions and observed that the insulating materials cannot easily capture escaping charged particles; thus, the detected charged particles are stronger than those of metals. Additionally, the results indicated that the negatively charged particles are detected more intensely than positively charged particles. For complex environments, Scudiero et al. (1998) proposed a new charged-particle-detection method and demonstrated that a Faraday ion collector can be adopted to capture specific charged particles by providing an external bias voltage. Under atmospheric conditions, Govindaraj and Subbiah (2019) measured the intensity of charged particles using a Faraday collector at a bias voltage of $\pm$ 100 V during the machining of three different workpieces (mild steel, copper, and stainless steel) using a carbide cutting tool. The results demonstrated that the mechanical and electrical properties of workpieces are directly proportional to the intensity of charged particle emissions. However, limited attention has been directed towards the self-excited axial electric field generated by charged particle emission at the tool–chip or tool–workpiece contact zone. Matta et al. (2009) conducted sliding tests in a hydrogen-containing test chamber and analysed the chemistry of sliding contact surfaces. They observed that the emission of charged particles may have an important role in reducing friction and wear by

forming surface films. Furthermore, the author's previous four-ball friction experiments have demonstrated that lubricants with different electroosmotic properties can influence the formation of tribofilms on wear surfaces (Xu et al., 2020). Therefore, it is crucial to understand the influence of self-excitation electrical properties of the contact zone on lubricant electroosmosis and further explore the effect of the difference in self-excitation electrical properties in the processing area on the lubricant penetration mechanism.

Electroosmosis is an electrokinetic effect on a liquid in a microcapillary, which is produced by the action of the electric field on diffusion layer ions in the electric double layer (EDL) at the solid–liquid interface (Van et al., 2005). Harvey et al. (2002) established a solid–liquid interface model and concluded that the EDL is generated by the dissociation of surface groups or ion adsorption when the liquid contacts the material surface. He et al. (2012) and Ren (2018) have demonstrated that the resulting electroosmotic flow (EOF) causes the liquid to move in a defined direction relative to the stationary capillary wall, which is often employed in operations such as liquid chromatographic separations and electrokinetic micropumps. Wang et al. (2007) stated that the potential at the shear plane between the charged surface and liquid moving with respect to each other represents the zeta potential, which reflects the potential of electrostatic interactions and the expected capillary EOF through its polarity and amplitude. According to Huisman et al. (2000) and Sze et al. (2003), several methods, such as the electroviscous, electroosmosis, and streaming potential methods, can be used to measure the zeta potential at the solid–liquid interface. Gallardo et al. (2012) claimed that the streaming potential method has a wide range of applications, and it can determine the amplitude and polarity of the zeta potential simultaneously and can consider the inverse property of EOF. Mockel et al. (1998) measured the zeta potentials on ultrafilter membrane surfaces fabricated from unmodified polysulfone and six carboxylated polysulfones in 1 mM (mmol/L) KCl using the tangential streaming potential method. They observed that the surface properties have a significant influence on the zeta potential, and the potentials on different membrane surfaces varied from − 20 to − 50 mV. However, to date, only a few studies have focused on the zeta potential measurement of cutting tools (such as cemented carbide) and workpiece materials in low-concentration surfactant solutions. According to the principle of zeta potential measurement, when using the streaming potential method, the differences in the combination of materials and liquids can significantly affect the measurement of the zeta potential. When a higher surface charge material or lower concentration solution is employed, the contribution of the surface conductance of the material cannot be neglected (the reverse conductive current can be conducted through the surface of the material); otherwise, the zeta potential is underestimated. Fievet et al. (2003) claimed that the Helmholtz–Smoluchowski (H–S) equation should be selected for the calculation of the zeta potential, and Chang (1955) stated that the diffusion coefficient of the diluted solution can be calculated using the Wilke equation.

EOF can be directly affected by the axial electric field and zeta potential. Mockel et al. (1998) discussed that changing the pH value of the solution can adjust the polarity and magnitude of the zeta potential by dissociating the surface groups, and finally, the EOF is regulated. Moreover, the addition of a specific surfactant can affect the magnitude and direction of EOF. For instance, Macdonald et al. (2005) stated that zwitterionic surfactants (such as 3-[(3-choleamidopropyl)-dimethylamino]−1-propanesulfonate [CHAPS], sodium lauriminodipropionate [SLI], etc.) can increase EOF without changing its direction, whereas Tavares et al. (1997) claimed that the addition of cationic surfactants (such as tetradecyltrimethylammonium bromide [TTAB], cetyltrimethylammonium bromide [CTAB], etc.) can change the direction of EOF at a very low concentration (0.05 mM). Furthermore, Movahed et al. (2012) commented that the surfactant may have an underlying influence on the adjustment of EOF by forming an adsorption layer at the solid–liquid interface and changing the EDL structure owing to its special molecular structure. Feng et al. (2021)

studied the lubrication properties of deionized (DI) water, an electroosmotic promoter lubricant (SLI lubricant), and an electroosmotic suppressant lubricant (CTAB lubricant) at a steel–steel interface through four-ball wear tests. The research results indicated that the friction coefficient and wear scar diameter could be reduced by using the SLI lubricant, whereas the CTAB lubricant produced opposite test results. This phenomenon may be attributed to the role played by the electroosmosis of the lubricant in the gap of the friction contact zone in regulating its lubrication effect. However, only one type of steel–steel contact pair has been applied in experiments, and the friction between the tool and chip/workpiece contact pairs is similar to that in friction contact pairs, and there exist other apparent electrical phenomena. Therefore, it is necessary to further explore the electroosmosis effect of the cutting fluid during cutting using different tool–workpiece combinations. The electroosmosis performance of the cutting fluid may provide a significant understanding of the regulation mechanism of the electroosmosis effect. Thus, it would create a fundamental evolution of the penetration of the lubricant in the processing area and, eventually, increase the efficiency of lubricants in different processing methods.

1.1. Problem identification

This study attempts to investigate the capillary electroosmosis effect on water-based cutting fluids in the turning process. The performance of the electrical-driven fluid penetration of the tool–chip contact zone slit (Fig. 1[a, b]) primarily depends on the EDL characteristics of the tool and chip material surfaces and the axial self-excited electric field in the interstitial spaces. The zeta potential at the EDL reflects the net charge density of the diffusion layer; the electric field force applied to the net charges in the diffusion layer is produced by the space axial self-excited electric field, which results from the exoelectrons generated by the tool–chip friction. Therefore, the zeta potential at the solid–liquid interface and the intensity of the self-excited electric field are the main factors affecting EOF (Fig. 1(c)).

To evaluate the electroosmosis ability, we used two types of cutting fluids added with an electroosmotic promoter or suppressant to study the formation mechanism of the zeta potential at the tool–chip interface by detecting the streaming potential of tool and workpiece surfaces. In the cutting test, the charged particles escaping from the flank-machined surface interstitial spaces were detected by combining a Faraday collection plate with a bias electrode plate, which could both avoid the interference of chips during detection and selectively collect the specific particles. The self-excited electric field intensity in the contact zone was calculated using the emission intensity of the charged particles. Finally, the effects of cutting fluids with different electroosmosis capabilities on cutting force, surface roughness, and tool wear were analysed in the cutting experiments, and the mechanism and control means of electroosmosis were explored.

2. Experimental details

2.1. Streaming potential testing and zeta potential details in various cutting fluids

The EDL is formed when surface charges on the tool–chip capillary wall attract anti-ions in the cutting fluid. Under the direct current electric field, EOF is generated by the fluid in the diffusion layer. The EOF velocity can be directly affected by the zeta potential. According to Slepicka et al. (2010), the zeta potentials of tools and workpiece materials in the cutting fluids used in this study are generally not easily measurable using commercial instruments, but they can be calculated by measuring their streaming potential.

Commercial cutting fluid frequently contains many ionic compositions. To reduce the influence of different ions on the electroosmosis effect as much as possible, we selected DI water as the basic cutting fluid in this study. An electroosmotic promoter cutting fluid (SLI cutting fluid) and electroosmotic suppressant cutting fluid (CTAB cutting fluid) were prepared by adding a zwitterionic surfactant (SLI) and cationic surfactant (CTAB), respectively, to DI water. Both surfactants were purchased from Shanghai Macklin Biochemical Co., Ltd., China. The concentrations of the additives were 0.05, 0.1, 0.2, and 0.3 mM. Subsequently, the cutting fluids were ultrasonically treated in a water bath for 30 min to ensure that the additives dissolved completely.

The streaming potential represents an electrokinetic phenomenon at the solid–liquid interface under the action of hydrodynamic forces and can be obtained by changing the fluid pressure and recording the voltage change at both ends of the channel (Drechsler et al., 2020). The streaming potential measurement system is shown in Fig. 2(a). The pressure difference at both ends of the narrow channel in the testing cell (6) was controlled using the pressure regulator (2) and visualized using the pressure gauge (3). Platinum electrodes (5) were immersed in the liquid near both ends of the channel. The streaming potential data was recorded by the electrometer (4; Keithley, 6517B). The range of the pressure difference between both ends of the slit channel was 0–0.08 MPa, which was adjusted by 0.01 MPa each time and maintained for 3 min. Each test was executed three times at room temperature (25 °C), and the average value was calculated.

For consistency in the workpiece and tool materials in cutting, AISI 304 stainless steel, AISI 1015 mild steel, YG6 cemented carbide steel, polyethylene (PE), and acrylonitrile butadiene styrene (ABS) plates were selected to build slit channels. Schematic diagrams of the tangential streaming potential measuring principle and slit channel structure are shown in Fig. 2(b) and (c), respectively. Two measuring sheets were separated to form the channel using PTFE separators. The length (l) of the channel was 160 mm, the width (w) was 10 mm, and the height (H) was 0.3 mm.
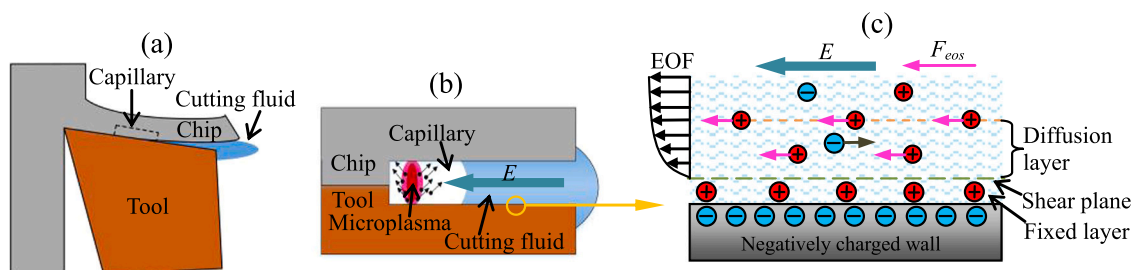

Fig. 1. (a) Location of the cutting zone; (b) penetration of cutting fluid in the cutting zone capillary; (c) schematic diagram of cutting fluid electroosmosis in a capillary under a self-excited axial electric field.
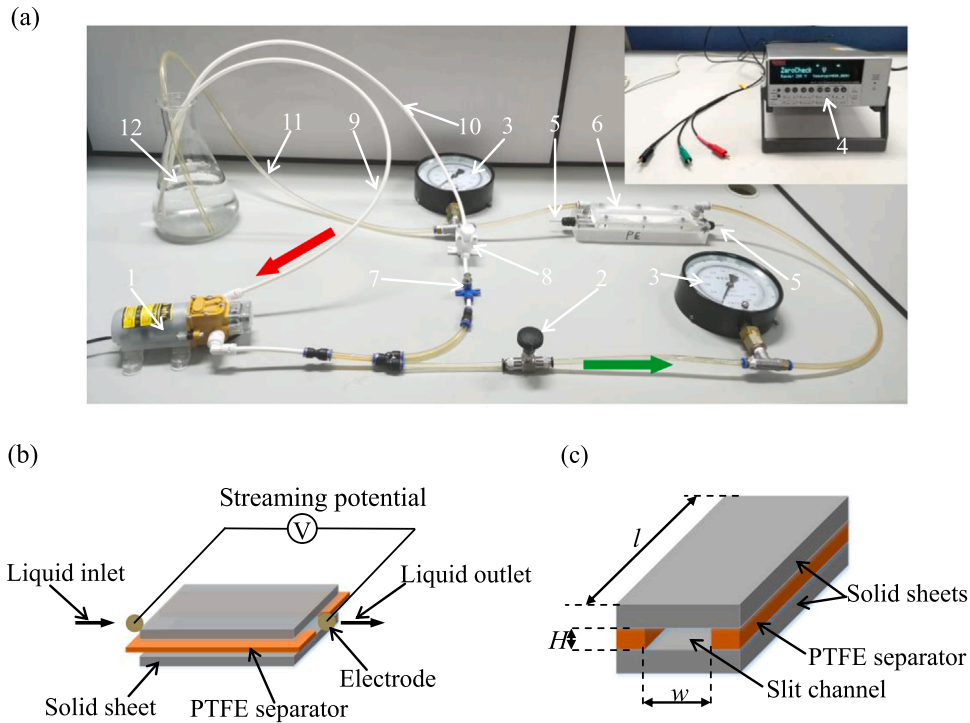
Fig. 2. (a) Streaming potential measurement system: (1) diaphragm pump, (2) pressure regulator, (3) pressure gauge, (4) 6517B electrometer, (5) platinum electrode, (6) testing cell, (7) pressure regulator, (8) constant pressure valve, (9) liquid inlet pipe, (10) liquid outlet pipe A, (11) liquid outlet pipe B, (12) liquid storage tank; (b) schematic diagram of tangential streaming potential measuring principle; (c) slit channel structure.
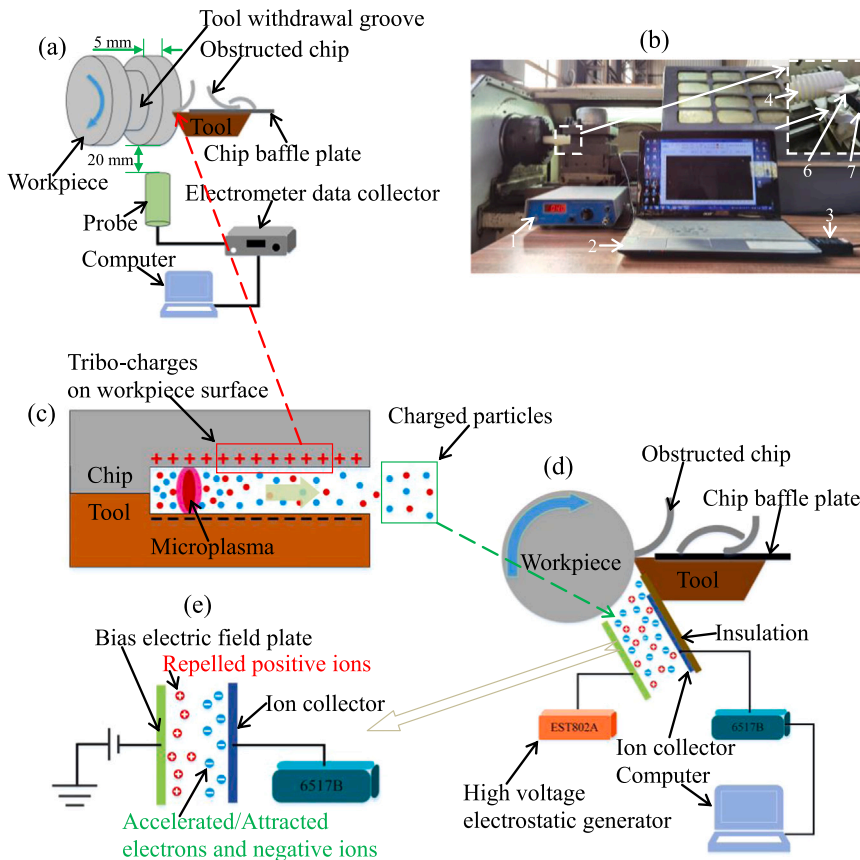

Fig. 3. Schematic illustration of the measurement of the triboelectrification electrostatic potential and charged particle emission intensity. (c) Distribution of the triboelectrification electrostatic potential and charged particle emission in the cutting contact zone; (b) schematic illustration of the triboelectrification electrostatic potential measurement; (c) photographic view of the triboelectrification electrostatic potential measurement of the workpiece experimental setup: (1) electrometer data collector, (2) computer, (3) data acquisition card, (4) workpiece, (5) probe, (6) chip baffle plate, and (7) tool; (d) principle of charged particle emission intensity measurement at atmosphere; (e) with negative bias electric field.

2.2. Testing details for triboelectrification electrostatic potential and charged particle emission intensity for various cutting parameters and materials

The triboelectrification electrostatic potential and radial electric field are caused by an equal number of different charges on the two contact surfaces owing to the intense friction between the tool and chip/workpiece in the cutting area. The axial electric field for the EOF of the cutting fluid in the cutting zone is generated by the emitted charged particles (including electrons and negatively and positively charged particles) caused by an electron avalanche. A schematic diagram of the triboelectrification electrostatic potential and charged particle emission in the cutting area gap is shown in Fig. 3(c).

The potential of the chip can be approximately replaced by that of the newly machined surface because directly measuring the potential of chips directly is difficult, and the tool experiences a similar friction process with the chip and machined surface of the workpiece in the turning test. For the measurement, a vibratory capacitance electrometer (EST102, Beijing Hua Jinghui Technology Ltd., China) probe was placed 20 mm below the newly machined surface (Fig. 3(a)).

The intensity of the charged particle emission in the tool–chip contact zone was approximately replaced by that of the tool flank–newly machined surface gap because of the contact between the curly chips and the tool rake face. The emission intensity of these escaping charged particles determined the magnitude and direction of the axial electric field at the cutting zone capillary. As shown in Fig. 3(d), a Faraday collecting plate fabricated from a silver sheet was set on the tool flank face, and a bias electric field plate was set at 20 mm away from the collecting plate to ensure that the Faraday collecting plate could capture specific charged particles. When a negative bias electric field (Fig. 3(e)) was applied, the escaping negatively charged particles were captured by the collector, and the intensity of the particle flow was detected by an electrometer (Keithley, 6517B). Similarly, the intensity of the positively charged particle flow can be obtained by applying a positive bias electric field. The voltage of the bias electric field was provided by a high voltage electrostatic generator (EST802A, Beijing Hua Jinghui Technology Ltd., China), and the intensity was set to $\pm$ 700 V/cm.

Detections of triboelectrification potentials and charged particle emission intensities were performed on a CAK6150D precision lathe (Fig. 3(b)). To prevent wrapping of the chip around the tool, we divided the workpiece into a stepped shaft with the same diameter and set the segment to 5 mm to limit the machining length of each experiment. An insulating baffle plate was set on the rake face to avoid interference between chips and the charged particle collector (Fig. 3(b)). The workpieces used were AISI 1015, AISI 304, PE, and ABS with a diameter of 60 mm. The cutting tools employed in these investigations were PVD-TiAlN-coated cemented carbide cutting tools (CCMT09T304N-SU, Sumitomo Electric, Japan), and the rake angle was 8°. The cutting speed was 44.6, 63.1, and 89.4 m/min; the depth of the cut was 0.25, 0.5, and 1 mm; the feed rate was 0.25 mm/r; and the cutting length was 5 mm. The average value of the measured potential or current in the machining period was considered as the measurement result. Before testing, the workpieces were pre-machined with a cut depth of 1 mm to eliminate any surface irregularities and ensure cutting continuity for all tests. Each set of tests was executed using a fresh tool edge to retain an identical experimental context. Each experiment was repeated three times, and the average value was recorded. All tests were conducted under dry cutting conditions. The intensity of charged particle emission is not affected by the cutting fluid during the actual machining because the emission of charged particles occurs in the initial separation stage between chip and workpiece.

2.3. Turning testing using cutting fluids with different electroosmotic properties at varying cutting parameters and materials

The turning experiment was conducted to investigate the influence of the electrokinetic effect on the performance of the cutting fluid in the contact zone capillaries during the cutting process. The workpieces, tool, and cutting parameters in this test are listed in Section 2.3. The cutting fluids employed are provided in Section 2.1, and the liquid was supplied to the cutting zone using a siphon nozzle with an air pressure of 0.2 MPa and flow rate of 50 ml/min. Each set of tests was conducted using a fresh workpiece and tool edge to maintain the same experimental context. Each test was repeated three times, and then the average value was recorded.

The cutting forces and surface roughness were recorded after the fourth pass (each cutting length was 125 mm). The cutting forces were measured using a three-component dynamometer (9129 A, Kistler, Switzerland). A portable surface roughness tester (SJ-210, Mitutoyo, Japan) with a sampling length of 0.8 mm was used to measure the surface roughness of the workpiece at five specific points. A scanning electron microscopy (SEM) system equipped with an energy dispersive X-ray spectroscope (EDS; EVO18, Zeiss, Germany) was employed to identify the predominant type of the tool wear mechanism.

3. Electroosmosis influential parameters: a prerequisite for understanding the electrokinetic effect of cutting fluid in the cutting contact zone

To explore the electroosmosis effect of cutting fluid in the cutting zone under turning conditions, we first studied the formation mechanism and regulation method of the zeta potential and streaming potential of cutting fluid on the surfaces of tool and chip materials.

The temperature in the cutting contact zone of the metal workpiece can reach several hundred degree Celsius. Although the temperature of the contact zone is lower than that of the metal during polymer cutting, it is still higher than that of the channel in the streaming potential measuring device employed in this study. The investigation conducted by Godlevski et al. (1997) indicated that the penetration of the cutting fluid into the cutting zone capillary can be divided into three phases: (a) penetration in the liquid phase, (b) microdroplet explosion, and (c) filling of the gas phase. This study focused only on the liquid phase penetration of the cutting fluid. It is generally accepted that the lubrication performance of the cutting fluid is positively correlated with the penetration degree of the liquid phase in the cutting zone. Therefore, this study focused on the streaming and zeta potentials of different cutting fluids in various workpieces in the liquid phase penetration stage, which can be used as the basis to explore the influence of electroosmosis on capillary penetration of cutting fluids. Additionally, when the cutting fluid is in the temperature range of the liquid phase, the absolute values of streaming and zeta potentials increase with temperature (Li, 2011), which is conducive to the electroosmosis effect of the cutting fluid.

Furthermore, the formation mechanism of the self-excited axial electric field in the capillary region of the tool–chip contact zone was described according to the triboelectrification electrostatic potential and charged particle emission. Based on these investigations, through the analysis and calculation of the capillary electroosmotic force in the tool–chip contact area, an understanding of the regulation mechanism of electroosmosis was obtained.

3.1. Formation mechanism of the zeta and streaming potentials of cutting fluid on tool and chip material surfaces

When metal and polymer materials encounter a solution, the solid–liquid interface is frequently negatively charged by the selective adsorption of ions. The excess negative surface charges attract anti-ions to form the interface EDL (Saboorian and Chen, 2019). When pressure is applied to one side of the slit channel, the charges in the diffusion layer accumulate on the other side. At this time, the streaming potential is generated on both sides of the slit channel (Fig. 4(c)).

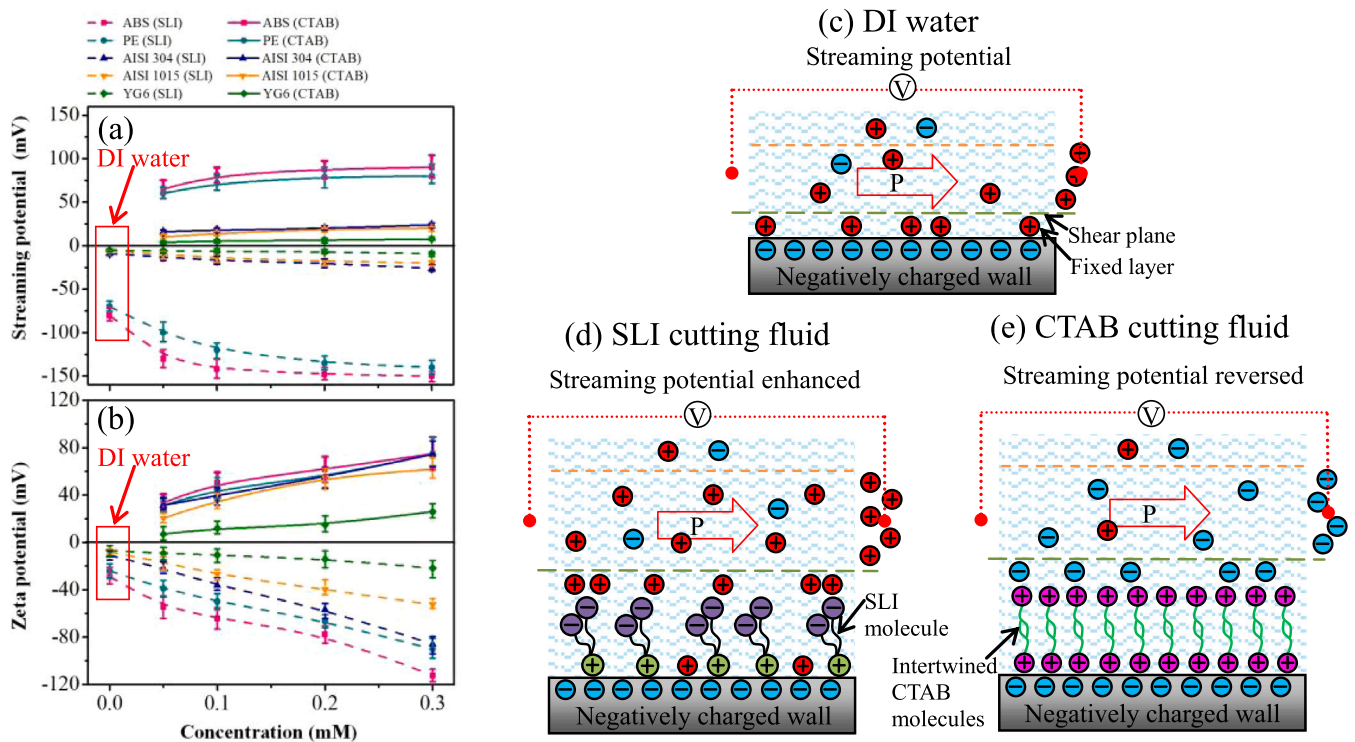The zeta potential of a flat material surface in a diluted solution can

Fig. 4. (a, b) Streaming and zeta potentials of different cutting fluids in different slit channels. (c–e) Regulation mechanism of different electroosmotic additive molecules on streaming potential: (d) SLI cutting fluid and (e) CTAB cutting fluid.

be calculated from the detected streaming potential using the H-S equation (Drechsler et al., 2020).

$$\varsigma = \frac{E_s}{\Delta P} \cdot \frac{\eta}{\varepsilon_r \cdot \varepsilon_0} \cdot \left(\frac{\lambda^h \cdot R^h}{R} \right) \quad (1)$$

where E_s is the streaming potential, ΔP is the pressure difference of single regulation (0.01 MPa), and η is the viscosity of the cutting fluid. The conductivity term is in parentheses, where λ^h is the conductivity of high concentration electrolyte solution (such as 100 mM KCl solution), R^h is the resistance when the slit channel is filled with high concentration electrolyte solution, and R is the resistance when the slit channel is filled with low-concentration cutting fluid (such as 0.1 mM CTAB cutting fluid). The resistance was measured by connecting the 6517B electrometer to the electrodes at both ends of the slit channel when this channel is filled with solution, and the results are shown in Supplementary Table S1.

One molecule of the SLI cutting fluid included a nitrogen-containing cationic group and two carboxylic acid anionic groups. Under the electrostatic force, the cationic group was adsorbed on the negatively charged material surface, and the carboxylic acid anion groups remained in the solution. The carboxylic acid anion groups adsorbed more positive ions in the solution to form a new diffusion layer with a higher concentration of positive ions, increasing the streaming potential (Fig. 4(c) to (d)). With an increase in the SLI concentration, the streaming potential initially increased and then stabilized, as shown by the dotted line in Fig. 4(a). This may be because the effective adsorption of additive molecules on the material wall tends to be saturated (Teixeira et al., 2018). Compared with DI water, the surface streaming potential of 0.2 mM SLI cutting fluid was greater by 85 % (ABS), 92.9 % (PE), 122.2 % (AISI 304), 198.5 % (AISI 1015), and 42 % (YG6). Additionally, the absolute values of the streaming potential on the insulating materials (60–150 mV) were higher than those on the metal materials (3.8–26 mV), indicating that the insulating material had a stronger selective capacity to absorb ions in the solution and generated more surface charges. The resistance decreased when the cutting fluid

with a higher concentration filled the channel, resulting in an increase in the conductivity term in Eq. (2). Therefore, the absolute values of zeta potentials continuously increased with the additive concentration, as shown by the dotted line in Fig. 4(b). The zeta potential of the 0.2 mM SLI cutting fluid on the five types of material surfaces was greater than that of DI water by 168.5 % (ABS), 170 % (PE), 419.3 % (AISI 304), 397.5 % (AISI 1015), and 104.3 % (YG6). Furthermore, the addition of SLI did not change the polarity of the zeta potential but only increased its absolute value.

The quaternary ammonium cationic groups in the CTAB molecules were positively charged, and they were firmly adsorbed on the material surface under the action of an electrostatic force. With the increase in concentration, CTAB molecules covered the material surface to form a single-molecule adsorption layer, and additional new molecules formed a second adsorption layer through hydrophobic interaction. Finally, the ionic electricity in the diffusion layer changed from positive to negative. When the concentration reached 0.05 mM, the polarity of the zeta potential changed from negative to positive and increased with the CTAB concentration (Fig. 4(c)–(e)). The streaming and zeta potentials of the CTAB cutting fluid on different material surfaces were opposite to those of the SLI cutting fluid. The streaming potentials of insulating materials initially increased and then tended to stabilize with the increase in the CTAB concentration, while this trend was not apparent in metal materials, as shown by the solid line in Fig. 4(a, b). Compared with 0.05 mM, when the CTAB concentration reached 0.2 mM, the streaming/zeta potential on the five material surfaces increased by 35.4 %/84.2 % (ABS), 31.7 %/76.9 % (PE), 25 %/76.3 % (AISI 304), 90 %/169.6 % (AISI 1015), and 60.5 %/111.4 % (YG6). Under a stable pressure, the streaming potential values on the insulator surfaces were relatively stable, and an apparent 'step' phenomenon occurred with the change in pressure, indicating that the electroosmotic additive molecules had stronger adsorption on the insulating material surface. For the metal channels, although the streaming potentials changed with the pressure, the 'step' was not apparent (Supplementary Fig. S1). This might be attributed to the metal material having a smaller surface charge and

weak adsorption capacity for surfactant molecules compared with the insulating material, resulting in the instability of the streaming potential value under the same pressure.

3.2. Measurement of triboelectrification electrostatic potential and charged particle emission intensity during cutting

Owing to the violent friction between two friction pairs (tool–chip and tool–workpiece), a strong self-excited radial electric field is produced in the tool–chip contact zone capillary, which causes an electron avalanche and microplasma, and charged particles can escape from the tool–chip contact zone through the capillary slit.

The triboelectrification electrostatic potential of the material surface detected in the turning test is the residual potential of the electrostatic dissipation. The dissipation velocity of the electrostatic potential on the workpiece surface can be represented by half the decay time $t_{1/2}$ (Peilin, 1992).

$$t_{1/2} = \tau \ln 2 = 0.69\tau = 0.69\frac{\varepsilon_0 \varepsilon_{\mathrm{rw}}}{\gamma} \qquad (2)$$

Here, γ is the material conductivity, ε_{rw} is the relative dielectric constant of the workpiece, and ε_0 is the vacuum dielectric constant.

Since the conductivities of metals are significantly higher than those of insulating materials, the half decay times of metals are significantly smaller than those of insulators (Table 1). The minimum time required for the workpiece to move from the cutting area to the measuring area directly above the electrometer probe was approximately 0.03 s. During the test, most of the surface potentials of metal workpieces dissipated, resulting in their triboelectrification electrostatic potentials being significantly lower than those of insulating workpieces (Fig. 5(a, b)). The range of the electrostatic potential of the insulating workpiece surface was 150–350 V, whereas it was less than 1 V on the metal material surface (Supplementary Fig. S2). The increase in cutting depth and cutting speed aggravates the friction between the tool and chip/workpiece, resulting in more active charge transfer on the two contact pair surfaces and resulting in an increase in triboelectrification electrostatic potential. This is because the triboelectrification electrostatic potential is generated by surface charge transfer between contact pairs, and the carrier of charge can be electrons (Wang and Wang, 2019), ions (Williams, 2013), and material fragments in the gap of the contact zone (Chang et al., 2007). The charge carrier transfers more frequently when the friction between the two contact surfaces increases, eventually increasing the triboelectrification electrostatic potential (Nakayama, 2014).

The specific atomic (atomic number and work function), electrical, physical, and mechanical properties of a material can affect the emission intensity of a given cutting condition (Nakayama, 1999). The material properties of the five materials used in this study are listed in Table 2.

The triboelectrification electrostatic potentials generated on insulating material surfaces were higher than those on metal materials, which could form a radial electric field with higher intensity, thus inducing stronger charged particle emission (Fig. 5(c, d)). The magnitude of the charged particle emission intensity was 1×10^{-9}–1×10^{-8} A, and the intensities of charged particles when cutting insulating materials were approximately 3–6 times higher than those of metal materials. Additionally, the increase in cutting depth and cutting speed enhanced the friction electrostatic potential on the tool–chip surface, increasing the emission intensity of positively and negatively charged particles. Some fluctuations were observed when detecting single

polarity charged particles (Supplementary Fig. S3). From the overall analysis of the cutting process, we can conclude that the intensity of the negatively charged particle emission was always dominant in both metals and insulators. Thus, the polarity of net charged particles in the capillary was negative.

3.3. Formation mechanism of the self-excited axial electric field in the tool–chip contact zone capillary

The charged particles generated from the tool–chip contact area escape outward along the capillary slit. The self-excited axial electric field intensity at both ends of the capillary can be calculated according to the escape current intensity. The self-excited electric field intensity can be expressed as $E = \rho J$, where ρ is the air resistivity in the capillary ($\Omega\cdot$m), and J is the current density of escaping particles (A/m^2). The current density of escaped particles from each capillary slit is $J=I/nA$, where I is the current intensity generated by the net escaping charged particles, A is the cross-sectional area of a single capillary, and n is the number of capillaries in the contact area.

The morphology of the chip surface detected by the microscope (VW-6000, Keyence, Japan) is shown in Fig. 6(c), and its surface grooves can be used as capillaries in the cutting area for the penetration of the cutting fluid (Liu et al., 2010). When calculating the axial electric field, setting the average capillary radius as 5 μm and assuming that the number of capillaries on the chip surface is 10, the self-excited axial electric field intensity in a single capillary is $E = \rho I/10\,A$. When considering the existence of cutting fluid, the resistivity of cutting fluid used in this study (1×10^3–$1 \times 10^4\,\Omega$ m) was employed, and the range of calculation results was 1.5×10^2–1.09×10^3 V/cm, which satisfied the electric field strength required for capillary electroosmosis (150 V/cm) (Chen, 2006).

Because the charged particle emission intensities in insulating materials were significantly stronger than those of metals, the self-excited axial electric field of insulating material capillaries was higher under the same cutting parameters (Fig. 6(a, b)). The electric field intensities in ABS/PE were 390.9 %/284.2 % and 515.8 %/381.9 % higher than those of AISI 304 and AISI 1015, respectively, under a cutting depth of 1 mm, cutting speed of 89.4 m/min, and feed rate of 0.25 mm/r. When the resistivity of the material was similar, the axial electric field intensity increased with the cutting depth and speed. A possible explanation for this might be that the cutting load increases with the hardness and ultimate strength of the material, resulting in a concomitant increase in the self-excited axial electric field strength at both ends of the capillary (AISI 304 was higher than AISI 1015, and ABS was higher than PE).

3.4. Influence mechanism of capillary electroosmotic force on cutting fluid penetration

The electroosmotic force (F_{eos}) is the driving force of the EOF of the fluid in the cutting zone capillary (Fig. 1(c)). F_{eos} can be expressed as

$$F_{eos} = E\rho_e V_k = E\cdot\left(-\frac{\varsigma\cdot\sigma}{D_{AB}}\right)\cdot\left(\pi\left(2Rr - r^2\right) \times h\right) = -\frac{E\varsigma\pi\sigma h(2Rr - r^2)}{D_{AB}} \qquad (3)$$

where, E is the external axial electric field intensity, ρ_e is the net charge density in the diffusion layer, V_k is the volume of the EDL, ζ is the zeta potential, σ is the conductivity of cutting fluid, D_{AB} is the diffusion coefficient of solute A in solvent B, R is the radius of the capillary, r is the thickness of the EDL, and h is the penetration depth of the cutting fluid in

Table 1
Half decay time of electrostatic dissipation of workpiece and tool materials into air.

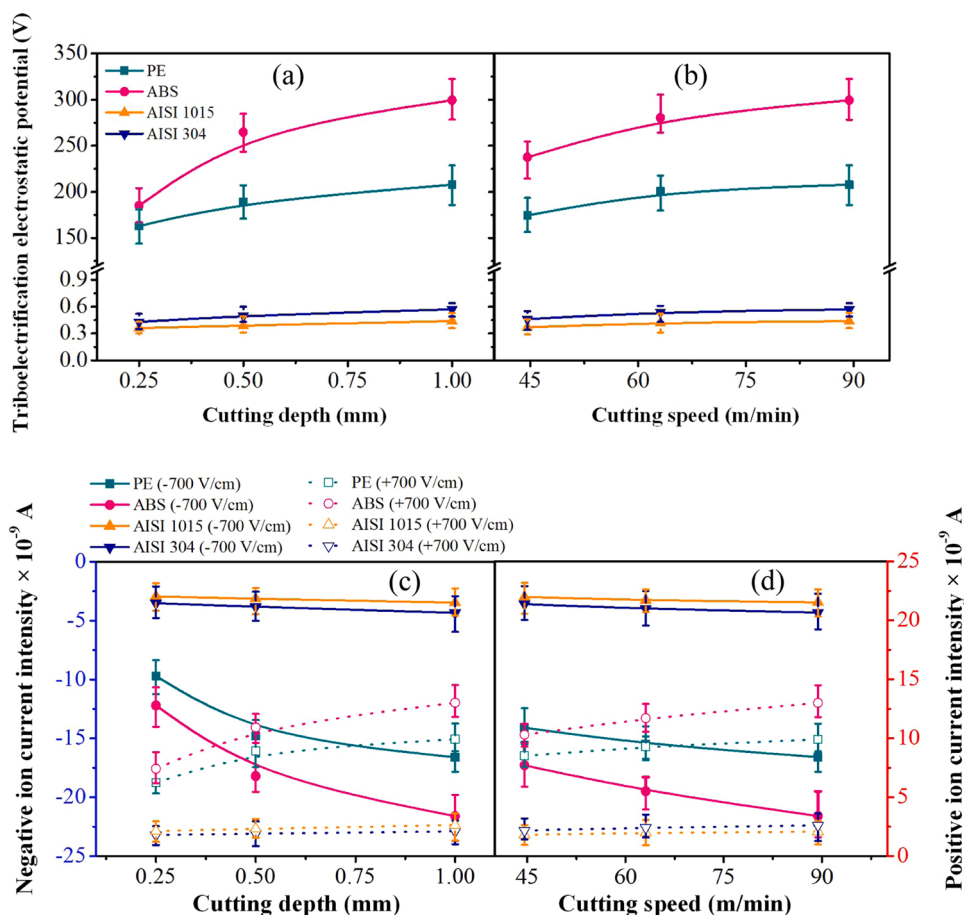| Material	AISI 1015	AISI 304	YG6	PE	ABS
Conductivity (S/m)	6.3×10^6	1.4×10^6	1.25×10^6	$\leq 1 \times 10^{-10}$	$\leq 1 \times 10^{-10}$
$t_{1/2}$ (s)	$< 2.3 \times 10^{-18}$	$< 1.05 \times 10^{-17}$	$< 1.17 \times 10^{-17}$	≥ 0.147	≥ 0.201

Fig. 5. (a, b) Variation in triboelectrification electrostatic potential under different cutting parameters; (c, d) variation in the negatively and positively charged particle emission intensity under different cutting parameters; (a, c) Cutting depth as a variable with the cutting speed and feed rate fixed at 89.4 m/min and 0.25 mm/r; (b, d) cutting speed as a variable with the cutting depth and feed rate fixed at 1 mm and 0.25 mm/r.

Table 2
Material properties of workpiece and tool materials.

Material	Electrical Resistivity (nΩ m)	Hardness	Ultimate Strength (MPa)	Yield Strength (MPa)
Mild steel (AISI 1015)	159	111 (HB)	385	325
Stainless steel (AISI 304)	720	201 (HB)	515	215
Tungsten carbide (YG6) as tool material	800	90 (HRA)	344	–
Polyethylene (PE)	$\geq 1 \times 10^{19}$	45 (Ball Indentation Hardness)	–	28
Acrylonitrile butadiene styrene (ABS)	$\geq 1 \times 10^{19}$	93.2 (Ball Indentation Hardness)	38	45.1

the cutting zone capillary. The calculation methods for diffusion coefficient D_{AB} and EDL thickness are described in Supplementary. The conductivity (σ) of the cutting fluid was measured using a conductivity meter (DDS-11A, INESA Scientific Instrument Co., Ltd.). The relative dielectric constant of water (78.49) was used for the calculation.

The magnitude and direction of the electroosmotic force on the cutting fluid column in the capillary can be adjusted by changing the electroosmosis performance of the cutting fluid, which is useful for clarifying the electroosmosis mechanism of cutting fluid in the tool–chip contact zone. According to the analysis in Section 3.1, the adsorption of

SLI molecules on the chip surface increases the density of ions in the diffusion layer and modifies the magnitude of the zeta potential without changing its polarity. Therefore, the electroosmotic force calculated using Eq. (3) increased with the SLI concentration and was consistent with the axial electric field direction, as shown by the dotted line in Fig. 7. When the SLI concentration reached 0.2 mM, the electroosmotic force in the capillary of the five materials reached 20.2×10^{-6} N (ABS), 12×10^{-6} N (PE), 3.1×10^{-6} N (AISI 304), 1.8×10^{-6} N (AISI 1015), and 0.6×10^{-6} N (YG6). However, when CTAB cutting fluid was used, the formation of a second adsorption layer of cations on the material surface changed the zeta potential polarity, changing the ionic polarity of the diffusion layer from positive to negative. The direction of the electroosmotic force was opposite to that of the axial electric field and increased with the concentration of CTAB, as indicated by the solid line in Fig. 7. In addition, the electroosmotic forces of the 0.2 mM SLI cutting fluid in insulation materials were 2.87–33.66 times higher than those of metal materials. Furthermore, the absolute value of electroosmotic force in ABS was 131.1 % higher than that in PE when the concentration of CTAB additive reached 0.2 mM. This discrepancy could be attributed to the fact that the electroosmotic force can be regulated by the axial electric field and zeta potential.

To study the influence of electroosmotic force on the penetrability of cutting fluid in capillaries, we established a force model of cutting fluid in the capillary penetration process and calculated the penetration depth of cutting fluid in capillaries of different materials. A single capillary was used as the object of investigation, and the following assumptions were made:
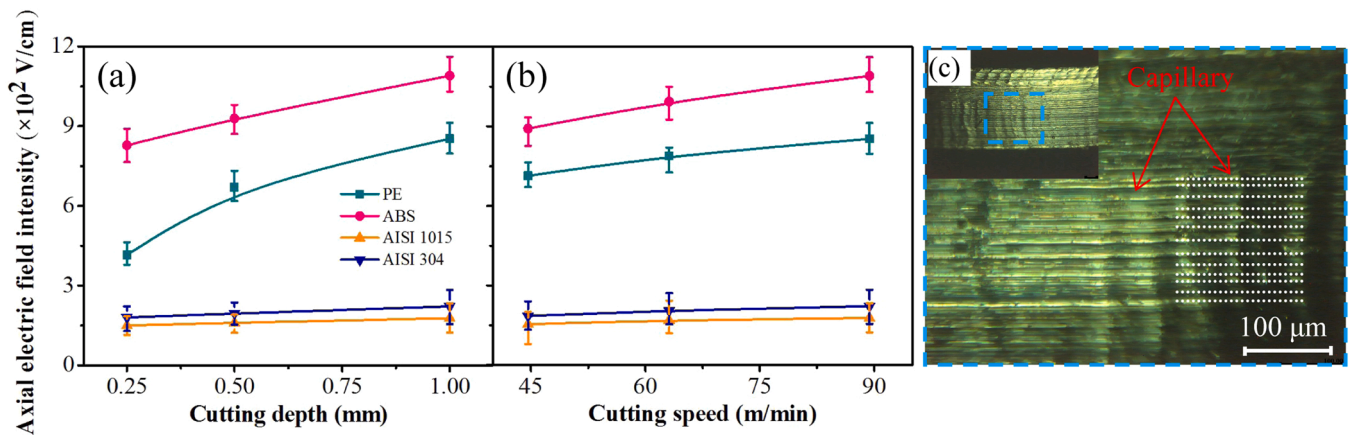
Fig. 6. (a, b) Variation in the self-excited axial electric field intensity under different cutting parameters when cutting various workpieces: (a) cutting depth as a variable with the cutting speed and feed rate fixed at 89.4 m/min and 0.25 mm/r, respectively, (b) cutting speed as a variable with the cutting depth and feed rate fixed at 1 mm and 0.25 mm/r, respectively; (c) chip surface topography (capillaries are formed by the grooves).
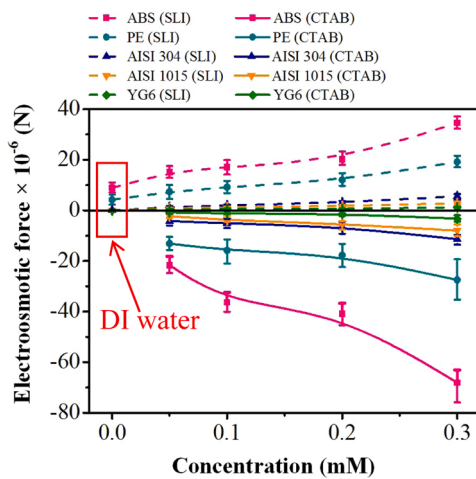

Fig. 7. Electroosmotic force of different cutting fluids in various capillaries. The electroosmotic force was positive when in the same direction as the axial electric field.

1. The capillaries in the cutting zone were distributed along the contact line of the workpiece and the tool.
2. The capillary lengths were 1–2 mm (Chiffre, 1977), and a single capillary was a vacuum cylinder with an opening at one end (Godlevski et al., 1997).
3. The existence time of capillary was significantly longer than the penetration time of the cutting fluid (Liu et al., 2010); here, the cutting fluid had sufficient time to penetrate inward.

The diagram of the cutting fluid force in the cutting zone capillary is presented in Fig. 8(a). Cutting fluids are subjected to the driving force (F_d) and resistance (F_r) during penetration. F_d includes capillary driving force (F_{cap}), atmospheric pressure (F_p), and electroosmotic force (F_{eos}); F_r is primarily the viscous resistance (F_{visco}) of cutting fluids on the capillary wall. The result of these forces is as follows:

$$F = F_{cap} + F_p + F_{eos} - F_{visco} \tag{4}$$

F_{cap} can be calculated using the Young–Laplace equation: $F_{cap} = 2\pi R\gamma\cos\theta$, where R is the capillary radius, γ is the surface tension, and θ is the contact angle of cutting fluids. P_{atm} is the standard atmospheric pressure (1.01×10^5 N/m^2), and $F_p = \pi R^2 \cdot P_{atm}$. The viscous resistance of the cutting fluid in the capillary can be derived using Newton's internal friction law and the Hagen–Poiseuille equation (Gao

and Liu, 2010): $F_{visco} = 8\pi\eta h\bar{\nu}$, where η is the cutting fluid dynamic viscosity, and $\bar{\nu}$ is the instantaneous velocity of fluid penetration.

In the process of the cutting fluid's capillary penetration, its speed and quality change. Therefore, these two changes should be considered simultaneously when examining the total inertia effect of the cutting fluid flow. The hydrodynamic equation was established by applying the momentum theorem, which can be expressed as follows: $d(m\bar{\nu})/dt = F$, where m is the mass of the cutting fluid in the capillary, $m = \pi R^2 h\rho_l$, ρ_l is the density of the cutting fluid, and F is the resultant force of the cutting fluid in the cutting zone capillary during penetration. The capillary dynamic equation can be expressed as follows:

$$2\pi R\gamma\cos\theta + \pi R^2 P_{atm} + \left(-\frac{E\zeta\pi\sigma h(2Rr - r^2)}{D}\right) - 8\pi\eta h\bar{\nu} = \frac{d(m\bar{\nu})}{dt} \tag{5}$$

The dynamic equation of cutting fluid's penetration into capillaries was solved using MATLAB software. Changes to the axial electric field and zeta potential affect the electroosmotic force of cutting fluid in capillaries of different materials, changing the direction and magnitude of EOF and the cutting fluid penetration. Fig. 8(b–f) compare the effect of cutting fluid type and capillary material on penetration depth. The addition of the electroosmotic promoter (SLI) enhanced the penetration depth of the cutting fluid. The penetration depth in ABS, PE, AISI 304, AISI 1015, and YG6 materials were 15.5 %, 13.2 %, 10.7 %, 9 %, and 5.8 % higher, respectively, than DI water. However, the penetration depth of cutting fluid with the electroosmotic suppressant (CTAB) in the above materials decreased by 13.7 %, 10.2 %, 8.4 %, 6.1 %, and 4.9 %, respectively. These calculation results indicated that electroosmotic force has an important role in regulating the process of the cutting fluid's penetration into capillaries.

4. Electroosmosis effect of cutting fluid during the turning process

Cutting fluids with different electroosmotic properties were used when cutting different materials. The cutting force, surface roughness, tool wear surface morphology, and element composition were analysed to reveal the influence of the electroosmosis effect of the cutting fluid in the cutting zone capillary on cutting performance.

4.1. Evolution of cutting force and surface finish behaviours using cutting fluids with different electroosmotic properties

Fig. 9 depicts the effect of the cutting fluids on the resulting cutting force and surface finish of four types of workpieces (AISI 1015, AISI 304, PE, and ABS). The resulting cutting force was calculated using the
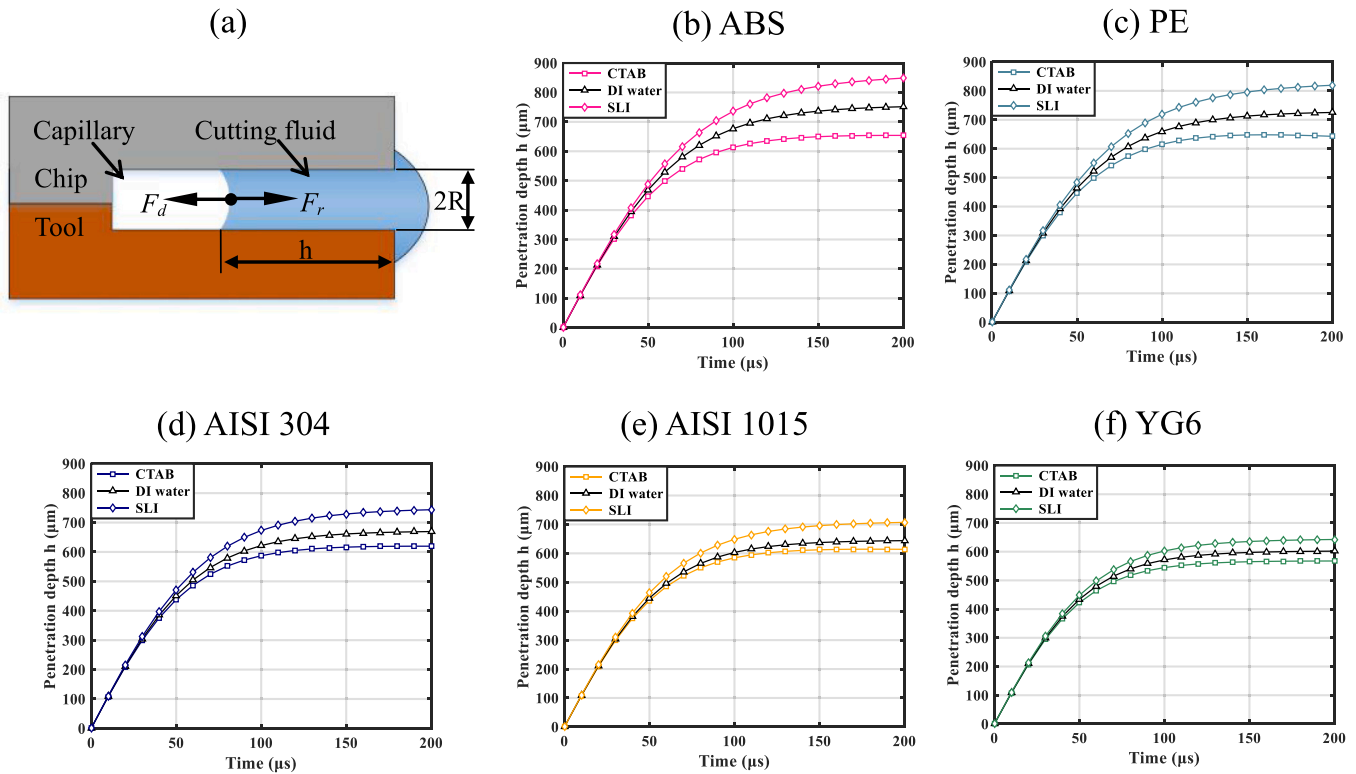
Fig. 8. (a) Force diagram of cutting fluid in a cutting zone capillary; (b–f) variation in the penetration depth of cutting fluids in capillaries of different materials. The concentration of electroosmotic additive was 0.2 mM, and the result achieved with DI water was used for comparison. The capillary length under all conditions was set to 1 mm.
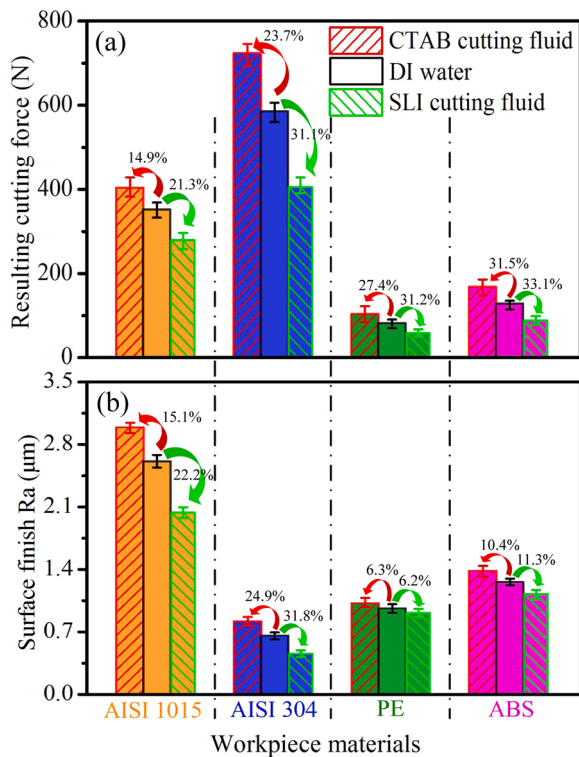

Fig. 9. Variation in the cutting force (a) and surface finish (b) under different cutting fluids. Additive concentration: 0.2 mM, depth of cut: 1 mm, cutting speed: 89.4 m/min, and feed rate: 0.25 mm/r.

formula $F_R = (F_x^2 + F_y^2 + F_z^2)^{1/2}$, where F_x is the radial thrust force, F_y is the tangential force, and F_z is the feed force. Compared with DI water, when SLI cutting fluid was employed, the electroosmotic force was enhanced in the same direction as the self-excited axial electric field. With the influence of electroosmosis, more cutting fluid penetrated the cutting zone capillary to lubricate the tool–chip contact interface, thus reducing the cutting force. However, the addition of CTAB changed the direction of the electroosmotic force, and the EOF was directed towards the outside of the capillary, which hindered the penetration of cutting fluid and ultimately resulted in an increase in the cutting force. With the increase in SLI concentration, the cutting force first decreased and then tended to stabilize (Supplementary Figs. S4[a, d, g, j]). When employing a 0.2 mM SLI cutting fluid, the cutting forces of AISI 1015, AISI 304, PE, and ABS decreased by 21.3 %, 31.1 %, 31.2 %, and 33.1 %, respectively, compared with DI water; however, for a 0.2 mM CTAB cutting fluid lubrication, the cutting forces of these four workpieces increased by 14.9 %, 23.7 %, 27.4 %, and 31.5 %, respectively (Fig. 9(a)). The stronger self-excited axial electric field generated in the capillary enhanced the electroosmosis effect of the cutting fluid. The influence of different cutting fluids on the cutting force of the insulating workpieces (27.4–33.1 % at 0.2 mM) was higher than that of metal workpieces (14.9–31.1 % at 0.2 mM), which was consistent with the trend of electroosmotic force.

For the same workpiece, the increase in cutting depth and speed could enhance the intensity of the axial electric field at both ends of the capillary, promoting the electrokinetic penetration of cutting fluid in the cutting zone. As depicted in Supplementary Figs. S4(b, e, h, k), compared with DI water, when the cutting depth was increased from 0.25 to 1 mm, the cutting force decreased by 8.1 %, 12.8 %, 13 %, and 13.4 % when cutting AISI 1015, AISI 304, PE, and ABS with a 0.2 mM SLI cutting fluid, whereas these cutting forces increased by 6.7 %, 9.9 %, 9.3 %, and 9.6 %, respectively, when 0.2 mM CTAB cutting fluid was employed. The variations in cutting force with cutting speed under the

lubrication of three cutting fluids are shown in Supplementary Figs. S4 (c, f, i, l). The cutting force clearly decreased as the cutting speed increased from 44.6 to 89.4 m/min in all scenarios. This was expected because a higher cutting speed can reduce the chip thickness and result in a lower cutting force (Huang et al., 2018). At higher cutting speeds, more severe friction between tool–chip/workpiece stimulates the emission of charged particles and thus increases the self-excited axial electric field intensity at both ends of the capillary, which increases the regulation of electroosmotic additives on the electroosmosis effect of cutting fluid in the cutting zone capillary, resulting in the effect of electroosmotic additives on the cutting force increased with cutting speed.

Fig. 9(b) presents the influence of cutting fluids on the surface quality of four workpieces. The change in surface quality was closely related to the cutting force, which was primarily attributed to electro-osmotic additives' regulation of the penetrability of cutting fluid in the cutting zone. When cutting insulators, the cutting force was low and the material was easy to remove; thus, the differences in surface quality due to cutting fluids with different electroosmotic properties were not apparent (Supplementary Fig. S5).

4.2. Analysis of tool wear mechanisms under the electroosmosis effect

The penetration ability of a cutting fluid affects its lubricity, resulting in differences in the tool edge wear form and the wear surface chemical composition (Xu et al., 2019). Cutting metal materials such as AISI 304 stainless steel can characterize tool edge wear significantly more than cutting ABS and other insulating materials.

Fig. 10 presents the SEM images of the worn tools after a 1000-mm cutting length lubricated with three different cutting fluids when cutting AISI 304. During cutting, high pressure and heat were applied to the cutting edge, which exacerbated the friction between the workpiece and the flank face, resulting in severe adhesive wear (Jawaid et al., 2000) and the breakage of the tool cutting edge (Lv et al., 2018). As shown in Fig. 10(a, b), a microchipping was obtained under lubrication using the CTAB cutting fluid. This may be because the severe friction in the interstitial spaces reduced the strength of the cutting edge when the CTAB lubricant was used, indicating the insufficient lubrication of the CTAB cutting fluid. Fig. 10(d, e) present the worn surface produced by DI water. The tool edge was relatively complete, indicating that the DI water's lubricating performance was better than that of the CTAB cutting fluid, but severe material adhesion still occurred. Furthermore, for the SLI cutting fluid, the worn flank face (Fig. 10(g, h)) exhibited the lowest wear and almost no tool breakage or adhesive layer, indicating an effective lubrication performance.

The EDS analyses of each worn flank face are depicted in Fig. 10(c, f, i), and the corresponding elemental contents are summarized in Table 3. The EDS analysis for the CTAB cutting fluid detected the highest concentration of W (75.47 wt %), the main chemical element of the cutting tool substrate, indicating that cutting edge breakage appeared. This was because insufficient lubrication in the cutting zone creates an increase in friction between the tool and workpiece, which causes the adhesion first. At the beginning of the cutting process, the adhered material could protect the cutting edge from rapid tool wear. If the processing continued, the seizure would become unstable, and the tool material would be torn and carried away from the substrate owing to the high tool temperature caused by the low thermal conductivity of austenitic stainless steels. Hence, microchipping of the cutting edge was the main wear pattern of the coated tools when cutting under CTAB cutting fluid lubrication.

When DI water was employed, the main contents of AISI-304 stainless steel (Fe for 74.01 wt %, Cr for 16.89 wt %, and Ni for 8.7 wt %) were clearly higher than those of the other two cutting fluids, indicating that adhesion was the main wear mechanism. In DI water cutting, more cutting fluid penetrated the interstitial spaces than with the CTAB cutting fluid. However, severe material adhesion still appeared on the flank

surface. This was primarily because the cutting fluid could not penetrate the interface area deeply to lubricate the contact layer; thus, it could not effectively reduce the thermally related adhesion mechanisms.

Under SLI cutting fluid lubrication, the contents of Fe, Cr, and Ni were 78.4 %, 34 %, and 98 % lower, respectively, than the contents of DI water, but the contents of Al and Ti, the two principal chemical elements of the tool coating, were approximately 200 times higher. This suggested that the cutting tool was subjected to less adhesive wear, corresponding to the improved machining performance. This phenomenon was due to the more efficient entry of cutting fluid into the cutting zone, resulting in a better lubrication performance for the tool–chip interface and, thus, relieving the tool wear.

4.3. Specific penetration mechanism at tool–chip interface under consideration of the electroosmosis effect

The analysis clearly demonstrates that electroosmosis has a significant influence on the penetration of cutting fluid at the tool–chip contact zone which would supplement and perfect the capillary penetration of cutting fluid in the machining process. The vapour blanket appears in the third stage penetration process (filling of the gas phase) when the cutting fluid penetrates the cutting zone capillary (Godlevski et al., 1997), but this study focused on the difference in the first stage penetration process (the liquid phase penetration stage) as the basis for evaluating the lubrication performance of cutting fluids. Therefore, the influence of the vapour blanket on the penetration of the cutting fluid through the capillaries at the tool chip interface was not considered.

Based on the above observations in Figs. 9 and 10, the distinct differences in the penetration mechanisms revealed by cutting fluids with different electroosmotic properties can be fully illustrated (Fig. 11). In the processes of friction and separation, the radial electric field established by the triboelectrification electrostatic potential on the chip and the rake face excites the initially escaped low-energy electrons, causing an electron avalanche and microplasma emission (Fig. 11(a)), which induces charged particle emission. The polarity of the net charged particles escaping outward from the capillary slit is negative, which forms a self-excited axial electric field pointing to the inside of the capillary region. As presented in Fig. 11(b), this electric field can trigger the electroosmosis of liquid in the capillary.

For DI water, the positive ions in the diffusion layer formed EOF under the action of an electroosmotic force in the same direction as the self-excited axial electric field, which promoted the penetration of cutting fluid into the cutting area (Fig. 11(c)). When the CTAB cutting fluid was employed, the adsorption of the CTAB molecules on the capillary wall reversed the polarity of the zeta potential. At this time, the negative ions in the diffusion layer were subjected to an electroosmotic force opposite to the direction of the axial electric field (Fig. 11(d)). The EOF towards the outside of the cutting area increased with the concentration, which hindered the penetration of the cutting fluid, resulting in insufficient lubrication of the tool–chip contact surface. Furthermore, the adsorption of SLI molecules on the capillary wall increased the number of surface charges, improved the zeta potential, and enhanced the number of positive ions in the diffusion layer. Compared with DI water, the positive ions in the SLI cutting fluid diffusion layer were subjected to a greater electroosmotic force in the same direction as the self-excited axial electric field, resulting in a higher EOF, which promoted the further penetration of cutting fluid into the cutting zone (Fig. 11(e)). The enhancement of the cutting fluid penetration in the cutting zone capillary can improve its role in lubrication and optimize the cutting performance.

5. Conclusions

In this study, to understand the electroosmosis effect on the penetration of water-based cutting fluids at the tool–chip interface, we comprehensively investigated the zeta potential properties of different
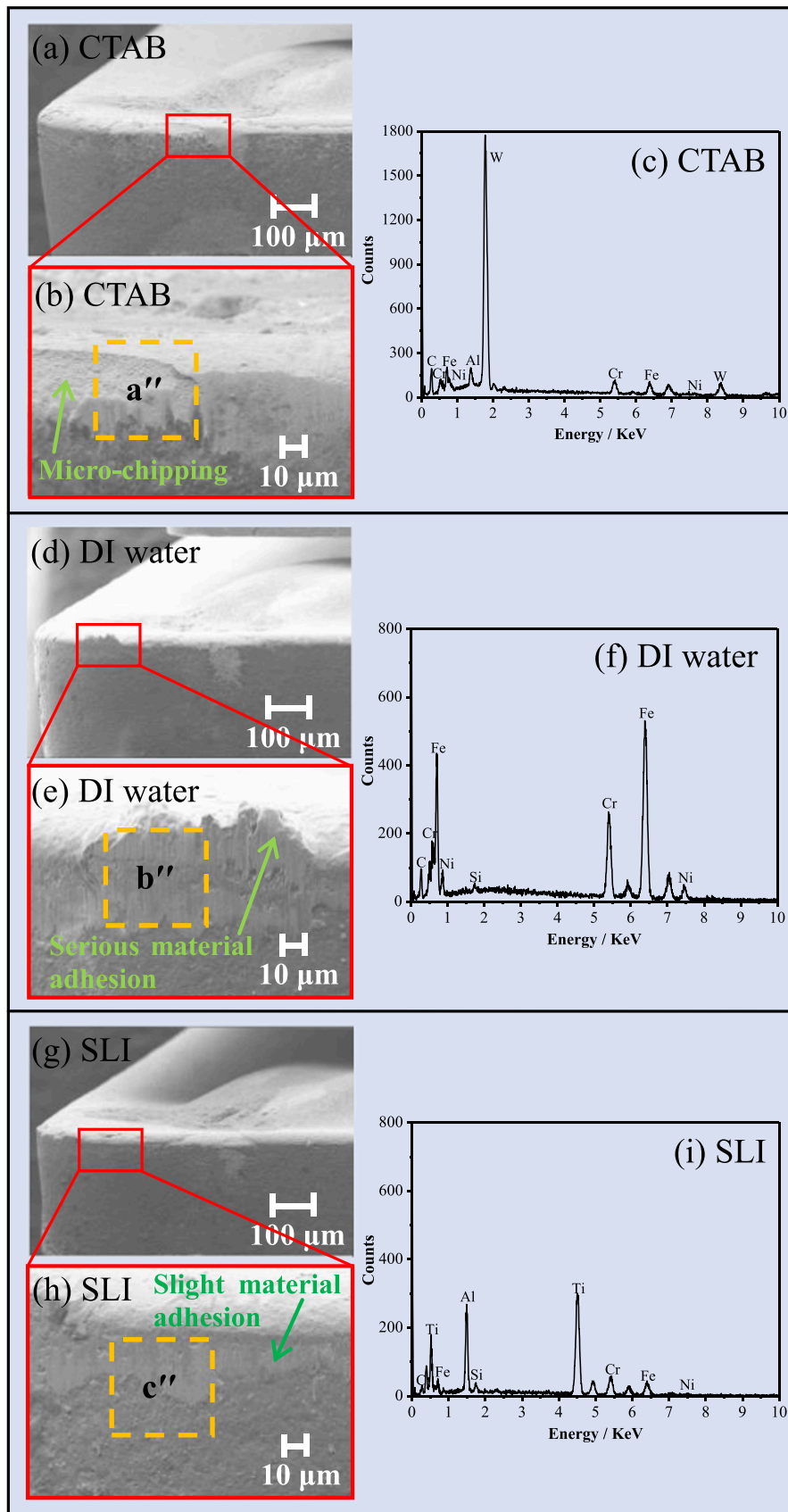
Fig. 10. SEM photographs and EDS analyses performed on the flank face of the coated tools when cutting 304 stainless steel with a cutting length of 1000 mm under (a–c) CTAB cutting fluid, (d–f) DI water, and (g–i) SLI cutting fluid conditions with an additive concentration of 0.2 mM, cutting depth of 1 mm, cutting speed of 89.4 m/min, and feed rate of 0.25 mm/r.

Table 3
Elemental content on the worn surface of cutting tools under different lubrication conditions (wt %).

	Fe	Cr	Ni	Al	Ti	W
CTAB cutting fluid	12.77	8.82	2.58	0.03	0.11	75.47
DI water	74.01	16.89	8.7	0.05	0.13	0
SLI cutting fluid	15.92	11.14	0.71	6.25	35.14	0

tools and workpiece materials in fluids, and the self-excited axial electric field in tool–chip interfaces based on exoelectron emission tests. The related underlying penetration mechanism caused by the electroosmosis effect on the cutting process was revealed for the first time. Key conclusions from this study are shown below:

● While the electroosmotic additive and its concentration in a fluid can adjust the EDL structure of the surface of a tool or workpiece through selective ionic adsorption, the regulatory methods of the zeta potentials of tools and workpieces in fluid have been revealed, by which the stronger capillary electroosmosis effect can be obtained with the cutting fluid with a higher zeta potential absolute value. According to the streaming potential measurements, the zwitterionic surfactant increased the zeta potential absolute value through electrostatic interaction, and the cationic surfactant reversed the zeta potential through electrostatic interaction and the hydrophobic effect,

indicating that the lubricant penetration in tool–chip interfaces could be controlled according to the properties of the EDL of tool and workpiece materials in a specific fluid.
● The self-excited axial-driven electric field and driving force of the capillary electroosmosis result from the triboelectrification potential in the tool–chip interface. While the net negatively charged particle emission flow escaping from the cutting contact area was detected by combining a Faraday collection plate with a bias electrode plate, we identified that the direction of the self-excited electric field and the calculated field intensity, with a range of 1.5×10^2–1.09×10^3 V/cm, satisfied the conditions for the occurrence of the electroosmosis effect on the lubricant penetration in tool–chip interstitial space.
● We observed that, compared with DI water, the cutting forces were reduced by 20–30 % in the cutting processes of AISI 1015, AISI 304, PE, and ABS materials under the lubrication condition with the higher zeta potential fluids, whereas the cutting forces increased by 15–30 % under the reversed zeta potential fluids, which was attributed to the direction change of the electroosmotic force. Moreover, the SEM/EDS analyses of the tool edges indicated the transfer from adhesive wear to micro breakage in AISI 304 turning, which explains the positive correlation between lubrication and penetration, resulting from an elevated electroosmosis effect.

The results described in this paper provide a comprehensive understanding of the electroosmosis effect on the lubrication potential of
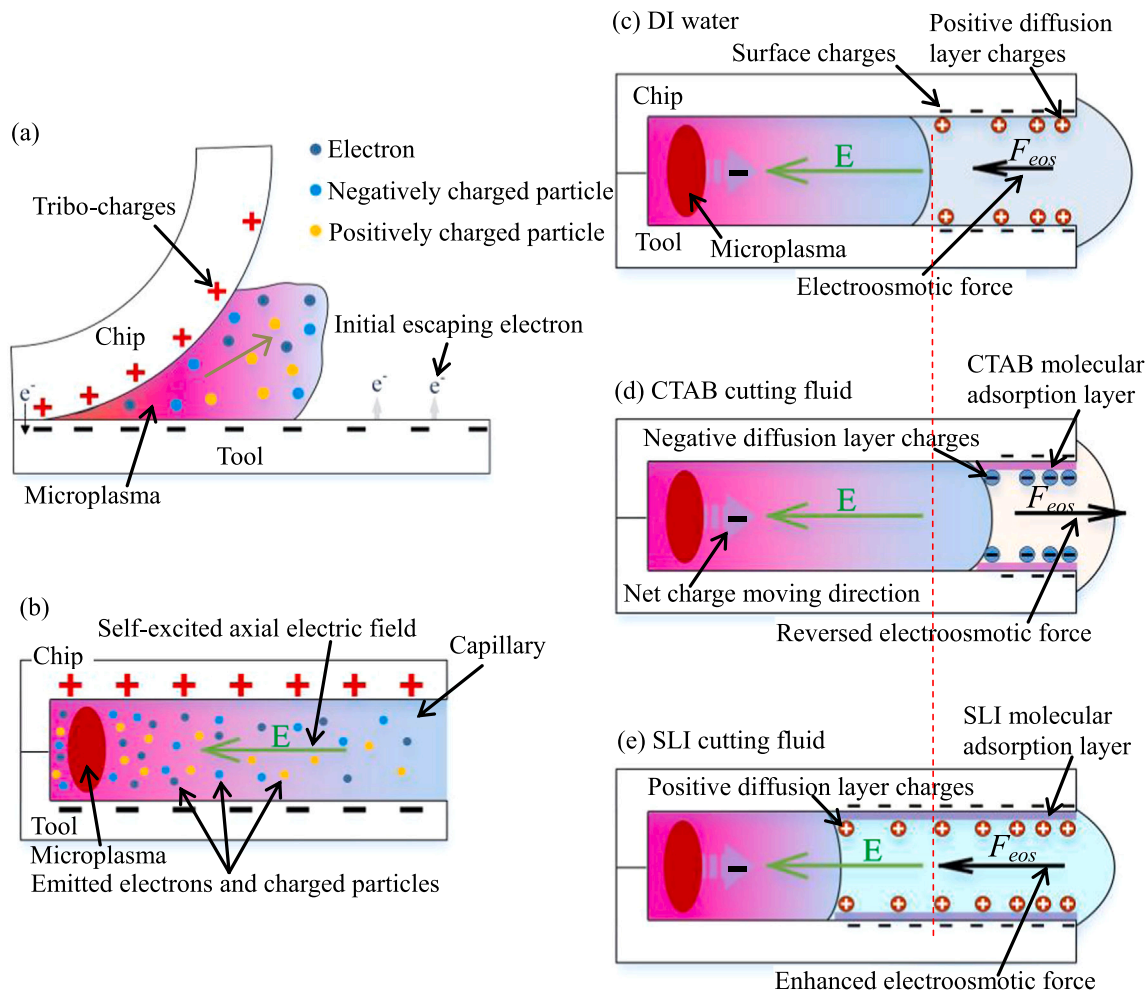
Fig. 11. (a) Model of the emission of charged particles due to triboelectrification. (b) Schematic of the generation of the self-excited axial electric field directed to the inside of the cutting zone capillary, which is generated by the emission of charged particles. Schematic of the specific penetration mechanism at the tool–chip interface in consideration of the electroosmosis effect on (c) DI water, (d) CTAB, and (e) SLI cutting fluids.

water-based cutting fluid under different combinations of tool and workpiece materials and on the specific penetration mechanism at different tool–chip interfaces. It can support future studies to improve the efficiency of commercial cutting fluid in different machining methods. Considering that the EOF in the cutting zone capillary is not visualized, a future development of the real-time monitoring of the EOF of commercial cutting fluid in microcapillaries will be performed in the laboratory or processing environment to further identify the universality of electroosmosis effect on water-based or even oil-based cutting fluid under different machining conditions.

CRediT authorship contribution statement

Bohua Feng: Conceptualization, Methodology, Software, Data curation, Formal analysis, Writing – original draft, Writing – review & editing. **Zhiqiang Luan:** Conceptualization, Resources, Writing – review & editing, Supervision. **Ruochong Zhang:** Methodology, Writing – review & editing. **Yu Xia:** Supervision, Writing – review & editing. **Weiqiang Yao:** Formal analysis, Investigation, Methodology. **Jiawei Liu:** Formal analysis, Investigation, Methodology, Writing – review & editing. **Yaliang Ma:** Investigation, Methodology. **Xiaodong Hu:** Investigation, Methodology, Writing – review & editing. **Xuefeng Xu:** Conceptualization, Formal analysis, Investigation, Methodology, Supervision, Writing – review & editing.

Declaration of Competing Interest

The authors declare that they have no known competing financial interests or personal relationships that could have appeared to influence the work reported in this paper.

Appendix A. Supporting information

Supplementary data associated with this article can be found in the online version at doi:10.1016/j.jmatprotec.2022.117653.

References

Chang, C., 1955. Correlation of diffusion coefficients in dilute solutions. Aiche J. 1, 264–270.

Chang, Y., Chu, H., Chou, H., 2007. Effects of mechanical properties on the tribo-electrification mechanisms of iron rubbing with carbon steels. Wear 262, 112–120. https://doi.org/10.1016/j.wear.2006.04.007.

Chen, Y., 2006. Capillary electrophoresis and its application. Chem. Ind.

Chiffre, L., 1977. Mechanics of metal cutting and cutting fluid action. Int. J. Mach. Tool. Des. Res. 17, 225–234. https://doi.org/10.1016/0020-7357(77)90016-6.

Cui, X., Li, C., Ding, W., Chen, Y., Mao, C., Xu, X., Liu, B., Wang, D., Li, H., Zhang, Y., Said, Z., Debnath, S., Jamil, M., Muhammad, A., Sharma, S., 2021. Minimum quantity lubrication machining of aeronautical materials using carbon group nanolubricant: from mechanisms to application. Chin. J. Aeronaut. https://doi.org/10.1016/j.cja.2021.08.011.

Drechsler, A., Caspari, A., Synytska, A., 2020. Influence of roughness and capillary size on the zeta potential values obtained by streaming potential measurements. Surf. Interface Anal. 52, 991–995. https://doi.org/10.1002/sia.6792.

Feng, B., Luan, Z., Zhang, T., Liu, J., Hu, X., Guan, J., Xu, X., 2021. Capillary electroosmosis properties of water lubricants with different electroosmotic additives under a steel-on-steel sliding interface. Friction 2223–7690. https://doi.org/10.1007/s40544-021-0507-3.

Fievet, P., Sbai, M., Szymczyk, A., Vidonne, A., 2003. Determining the zeta-potential of plane membranes from tangential streaming potential measurements: effect of the membrane body conductance. J. Membr. Sci. 226, 227–236. https://doi.org/10.1016/j.memsci.2003.09.007.

Gallardo, A., Vadillo, V., Perera, J., Bruque, J., Gonzalez, M., 2012. The zeta potential of extended dielectrics and conductors in terms of streaming potential and streaming current measurements. Phys. Chem. Chem. Phys. 14, 9758–9767. https://doi.org/10.1039/c2cp40743d.

Gao, S., Liu, H., 2010. Capillary Mechanics. Science Press, Beijing.

Gao, T., Li, C., Yang, M., Zhang, Y., Jia, D., Ding, W., Debnath, S., Yu, T., Said, Z., Wang, J., 2021. Mechanics analysis and predictive force models for the single-diamond grain grinding of carbon fiber reinforced polymers using CNT nano-lubricant. J. Mater. Process. Technol. 290. https://doi.org/10.1016/j.jmatprotec.2020.116976.

Gerth, J., Gustavsson, F., Collin, M., Andersson, G., Nordh, L., Heinrichs, J., Wiklund, U., 2014. Adhesion phenomena in the secondary shear zone in turning of austenitic stainless steel and carbon steel. J. Mater. Process. Technol. 214, 1467–1481. https://doi.org/10.1016/j.jmatprotec.2014.01.017.

Godlevski, V., Volkov, A., Latyshev, V., Maurin, L., 1997. The kinetics of lubricant penetration action during machining. Lubr. Sci. 9, 127–140. https://doi.org/10.1002/ls.3010090203.

Govindaraj, J., Subbiah, S., 2019. Charged-particle emissions during material deformation, failure and tribological interactions of machining. J. Tribology-Trans. Asme 141. https://doi.org/10.1115/1.4041670.

Guo, S., Li, C., Zhang, Y., Wang, Y., Li, B., Yang, M., Zhang, X., Liu, G., 2017. Experimental evaluation of the lubrication performance of mixtures of castor oil with other vegetable oils in MQL grinding of nickel-based alloy. J. Clean. Prod. 140, 1060–1076. https://doi.org/10.1016/j.jclepro.2016.10.073.

Harvey, T., Wood, R., Denuault, G., Powrie, H., 2002. Investigation of electrostatic charging mechanisms in oil lubricated tribo-contacts. Tribology Int. 35, 605–614. https://doi.org/10.1016/S0301-679X(02)00060-9.

He, C., Zhu, Z., Gu, C., Lu, J., Liu, S., 2012. Stacking open-capillary electroosmotic pumps in series to boost the pumping pressure to drive high-performance liquid chromatographic separations. J. Chromatogr. A 1227, 253–258. https://doi.org/10.1016/j.chroma.2011.12.105.

Huang, S., Lv, T., Wang, M., Xu, X., 2018. Effects of machining and oil mist parameters on electrostatic minimum quantity lubrication–emql turning process. Int. J. Precis. Eng. Manuf. Green Technol. 5, 317–326. https://doi.org/10.1007/s40684-018-0034-5.

Huang, S., Wu, H., Jiang, Z., Huang, H., 2021. Water-based nanosuspensions: Formulation, tribological property, lubrication mechanism, and applications. J. Manuf. Process. 71, 625–644. https://doi.org/10.1016/j.jmapro.2021.10.002.

Huisman, I., Pradanos, P., Hernandez, A., 2000. Electrokinetic characterisation of ultrafiltration membranes by streaming potential, electroviscous effect, and salt retention. J. Membr. Sci. 178, 55–64. https://doi.org/10.1016/S0376-7388(00)00479-8.

Jawaid, A., Sharif, S., Koksal, S., 2000. Evaluation of wear mechanisms of coated carbide tools when face milling titanium alloy. J. Mater. Process. Technol. 99, 266–274. https://doi.org/10.1016/S0924-0136(99)00438-0.

Li, B., Li, C., Zhang, Y., Wang, Y., Jia, D., Yang, M., Zhang, N., Wu, Q., Han, Z., Sun, K., 2017. Heat transfer performance of MQL grinding with different nanofluids for Ni-based alloys using vegetable oil. J. Clean. Prod. 154, 1–11. https://doi.org/10.1016/j.jclepro.2017.03.213.

Li, X., Jing, H., 2011. Effects of operating conditions on membrane charge property and nanofiltration. Front. Chem. Sci. Eng. 5, 492–499. https://doi.org/10.1007/s11705-011-1143-7.

Liu, J., Liu, H., Han, R., Wang, Y., 2010. The study on lubrication action with water vapor as coolant and lubricant in cutting ANSI 304 stainless steel. Int. J. Mach. Tools Manuf. 50, 260–269. https://doi.org/10.1016/j.ijmachtools.2009.12.001.

Liu, M., Li, C., Zhang, Y., An, Q., Yang, M., Gao, T., Mao, C., Liu, B., Cao, H., Xu, X., Said, Z., Debnath, S., Muhammad, J., Muhammad, A., Sharma, S., 2021. Cryogenic minimum quantity lubrication machining: From mechanism to application. Front. Mech. Eng. 16, 649–697. https://doi.org/10.1007/s11465-021-0654-2.

Lv, T., Huang, S., Liu, E., Ma, Y., Xu, X., 2018. Tribological and machining characteristics of an electrostatic minimum quantity lubrication (EMQL) technology using graphene nano-lubricants as cutting fluids. J. Manuf. Process. 34, 225–237. https://doi.org/10.1016/j.jmapro.2018.06.016.

Macdonald, A., Sheppard, M., Lucy, C., 2005. Enhancement of electroosmotic flow using zwitterionic additives. Electrophoresis 26, 4421–4428. https://doi.org/10.1002/elps.200500431.

Matta, C., Eryilmaz, O., Bouchet, M., Erdemir, A., Martin, J., Nakayama, K., 2009. On the possible role of triboplasma in friction and wear of diamond-like carbon films in hydrogen-containing environments. J. Phys. D-Appl. Phys. 42. https://doi.org/10.1088/0022-3727/42/7/075307.

Mockel, D., Staude, E., Dalcin, M., Darcovich, K., Guiver, M., 1998. Tangential flow streaming potential measurements: hydrodynamic cell characterization and zeta potentials of carboxylated polysulfone membranes. J. Membr. Sci. 145, 211–222. https://doi.org/10.1016/S0376-7388(98)00077-5.

Molina, G., Furey, M., Ritter, A., Kajdas, C., 2001. Triboemission from alumina, single crystal sapphire, and aluminum. Wear 249, 214–219. https://doi.org/10.1016/S0043-1648(01)00568-3.

Movahed, S., Khani, S., Wen, J., Li, D., 2012. Electroosmotic flow in a water column surrounded by an immiscible liquid. J. Colloid Interface Sci. 372, 207–211. https://doi.org/10.1016/j.jcis.2012.01.044.

Nakayama, K., 2014. Effect of normal force on the triboplasma generation under oil lubrication. Tribology Lett. 53, 449–456. https://doi.org/10.1007/s11249-013-0283-y.

Nakayama, K., 1999. Triboemission of charged particles and resistivity of solids. Tribology Lett. 6, 37–40. https://doi.org/10.1023/A:1019139002295.

Nakayama, K., 1994. Triboemission of charged particles from various solids under boundary lubrication conditions. Wear 178, 61–67. https://doi.org/10.1016/0043-1648(94)90129-5.

Nakayama, K., Fujimoto, T., 2004. The energy of electrons emitted from wearing solid surfaces. Tribology Lett. 17, 75–81. https://doi.org/10.1023/B: TRIL.0000017421.37209.15.

Nakayama, K., Yagasaki, F., 2019. The flow of triboplasma. Tribology Lett. 67. https://doi.org/10.1007/s11249-019-1186-3.

Olufayo, O.K.A., Kadernani, M., 2014. Tribo-electric charging in the ultra-high precision machining of contact lens polymers. Procedia Mater. Sci. 194–201. https://doi.org/10.1016/j.mspro.2014.07.024.

Peilin, Y., 1992. Generation and harm of static electricity. Phys. Technol. 29–31.

Podgaetsky, E., 2018. Determining the boundaries of the concentration area of action of the rehbinder effect for an s-shaped adsorption isotherm. Prot. Met. Phys. Chem. Surf. 54, 769–777. https://doi.org/10.1134/S2070205118050179.

Ren, Q., 2018. Bioparticle delivery in physiological conductivity solution using AC electrokinetic micropump with castellated electrodes. J. Phys. D. -Appl. Phys. 51. https://doi.org/10.1088/1361-6463/aae233.

Saboorian, J., Chen, Z., 2019. Calculation of re-defined electrical double layer thickness in symmetrical-electrolyte solutions. Results Phys. 15. https://doi.org/10.1016/j.rinp.2019.102501.

Scudiero, L., Dickinson, J., Enomoto, Y., 1998. The electrification of flowing gases by mechanical abrasion of mineral surfaces. Phys. Chem. Miner. 25, 566–573. https://doi.org/10.1007/s002690050149.

Slepicka, P., Vasina, A., Kolska, Z., Luxbacher, T., Malinsky, P., Mackova, A., Svorcik, V., 2010. Argon plasma irradiation of polypropylene. Nucl. Instrum. Methods Phys. Res. Sect. B-Beam Interact. Mater. At. 268, 2111–2114. https://doi.org/10.1016/j.nimb.2010.02.012.

Sze, A., Erickson, D., Ren, L., Li, D., 2003. Zeta-potential measurement using the smoluchowski equation and the slope of the current-time relationship in electroosmotic flow. J. Colloid Interface Sci. 261, 402–410. https://doi.org/10.1016/S0021-9797(03)00142-5.

Tavares, M., Colombara, R., Massaro, S., 1997. Modified electroosmotic flow by cationic surfactant additives in capillary electrophoresis - evaluation of electrolyte systems for anion analysis. J. Chromatogr. A 772, 171–178. https://doi.org/10.1016/S0021-9673(96)00985-5.

Teixeira, W., Santos, M., Gruber, J., Gutz, I., Lopes, F., 2018. Determination of neutral diols and carboxylic acids formed during glycerol electrooxidation by capillary electrophoresis with dual (CD)-D-4. Talanta 178, 1040–1045. https://doi.org/10.1016/j.talanta.2017.08.088.

Thimm, B., Glavas, A., Reuber, M., Christ, H., 2021. Determination of chip speed and shear strain rate in primary shear zone using digital image correlation (DIC) in linear-orthogonal cutting experiments. J. Mater. Process. Technol. 289. https://doi.org/10.1016/j.jmatprotec.2020.116957.

Van, E., Heuser, T., Hermes, D., Oosterbroek, R., Gardeniers, J., Van, A., 2005. Field-effect control of electro-osmotic flow in microfluidic networks. Colloids Surf. A-Physicochem. Eng. Asp. 267, 110–116. https://doi.org/10.1016/j.colsurfa.2005.06.048.

Wang, L., Dong, Y., 2020. Study of the mechanisms of contact electrification and charge transfer between polytetrafluoroethylene and metals. J. Phys. D: Appl. Phys. 53, 285–302. https://doi.org/10.1088/1361-6463/ab813e.

Wang, W., Zhou, F., Zhao, L., Zhang, J., Zhu, J., 2007. Measurement of electroosmotic flow in capillary and microchip electrophoresis. J. Chromatogr. A 1170, 1–8. https://doi.org/10.1016/j.chroma.2007.08.083.

Wang, X., Li, C., Zhang, Y., Ding, W., Yang, M., Gao, T., Cao, H., Xu, X., Wang, D., Said, Z., Debnath, S., Jamil, M., Muhammad, A., 2020. Vegetable oil-based nanofluid minimum quantity lubrication turning: academic review and perspectives. J. Manuf. Process. 59, 76–97. https://doi.org/10.1016/j.jmapro.2020.09.044.

Wang, Z., Wang, A., 2019. On the origin of contact-electrification. Mater. Today 30, 34–51. https://doi.org/10.1016/j.mattod.2019.05.016.

Williams, M., 2013. Triboelectric charging in metal-polymer contacts - how to distinguish between electron and material transfer mechanisms. J. Electrost. 71, 53–54. https://doi.org/10.1016/j.elstat.2012.11.006.

Xu, X., Luan, Z., Zhang, T., Liu, J., Feng, B., Lv, T., Hu, X., 2020. Effects of electroosmotic additives on capillary penetration of lubricants at steel/steel and steel/ceramic friction interfaces. Tribology Int. 151. https://doi.org/10.1016/j.triboint.2020.106441.

Xu, X., Lv, T., Luan, Z., Zhao, Y., Wang, M., Hu, X., 2019. Capillary penetration mechanism and oil mist concentration of Al_2O_3 nanoparticle fluids in electrostatic minimum quantity lubrication (EMQL) milling. Int. J. Adv. Manuf. Technol. 104, 1937–1951. https://doi.org/10.1007/s00170-019-04023-3.

Yamada, M., Shigemune, H., Maeda, S., Sawada, H., 2021. Temperature and humidity dependence of marangoni convection and its effect on the self-propulsion of an oil droplet. Chem. Lett. 50, 493–496. https://doi.org/10.1246/cl.200842.

电渗效应对水基切削液在刀-屑界面渗透润滑机理的影响

冯伯华[1, 2]　栾志强[1, 2]　张若冲[1, 2]　夏雨[1, 2]　姚伟强[1]　胡晓冬[1, 2]　许雪峰[1, 2]

(1. 浙江工业大学机械工程学院　杭州　310014；
2. 浙江工业大学特种装备制造与先进加工技术教育部/浙江省重点实验室　杭州　310023)

摘要：切削区毛细管润滑理论在解释切削液在刀-屑界面毛细管渗透发挥润滑作用时主要考虑大气压力和毛细力，而没有关注切削区荷电粒子发射所引起的切削液电动效应。接触区存在的电学效应所产生的电场足以诱发切削液产生电渗流。基于此，首次探索了电渗效应对水基切削液在刀-屑界面毛细管中渗透机理的影响。利用电渗流速度测量装置揭示了电渗添加剂、毛细管材料和轴向电场对切削液电渗特性的影响规律。通过测量切削区间隙中的荷电粒子发射强度，掌握了切削区毛细管两端自激轴向电场的变化特性。结果表明，切削液在切削区存在电渗效应且其作用效果与工件材料和荷电粒子发射强度相关，并且使用电渗促进型切削液润滑 AISI 304 工件时的切削力相比于纯去离子水和电渗抑制型切削液润滑时分别降低了 31.1% 和 44.3%。此外，对利用不同切削液润滑时的刀具刃口进行的 SEM 和 EDS 分析显示切削刃的磨损形式由粘附磨损转变为微崩刃，表明电渗效应与切削液在切削区的渗透以及切削性能存在正向联系。研究结果对于了解电渗效应对切削液渗透机理的影响，完善毛细润滑理论，以及最终提高切削液使用效率有重要参考价值。

关键词：电渗效应；电渗流；荷电粒子；水基切削液；切削性能

中图分类号：TG519.3

Influence of Electroosmotic Effect on the Penetration and Lubrication Mechanism of Water-based Cutting Fluid at Tool-Chip Interface

FENG Bohua[1, 2]　LUAN Zhiqiang[1, 2]　ZHANG Ruochong[1, 2]　XIA Yu[1, 2]　YAO Weiqiang[1]　HU Xiaodong[1, 2]　XU Xuefeng[1, 2]

(1. College of Mechanical Engineering, Zhejiang University of Technology, Hangzhou 310014;
2. Key Laboratory of Special Purpose Equipment and Advanced Processing Technology, Ministry of Education and Zhejiang Province, Zhejiang University of Technology, Hangzhou 310023)

Abstract：The micro-capillary lubrication theory explained lubricant penetration into the capillaries in the tool–chip interface under the action of atmospheric pressure and capillary force without considering the electrokinetic effect caused by triboelectrification. The axial electric field generated by the electrical effect in the cutting contact zone was enough to trigger the electroosmotic flow of cutting fluid. Based on this, the effect of electroosmosis on the penetration mechanism of water-based cutting fluid in the capillary at tool-chip interface was explored for the first time. The effects of electroosmosis additives, capillary materials and axial electric field on the electroosmosis characteristics of cutting fluid were revealed by using the measurement system of electroosmotic velocity. The variation of self-excited axial electric field at both ends of capillary in cutting zone was investigated by measuring the emission intensity of charged particles. The results showed that the cutting fluid has electroosmosis effect in the cutting zone, which related to the property of workpiece material and the emission intensity of charged particle. Compared with pure deionized water and electroosmotic suppressant cutting fluid, the cutting force lubricated with electroosmotic promoter cutting fluid was reduced by 31.1% and 44.3% respectively when cutting AISI 304. Moreover, the scanning electron microscopy (SEM) and energy dispersive X-ray spectroscopy (EDS) analyses on the tool edges using the above fluids showed a transfer from adhesive wear to micro breakage, which demonstrated that the electroosmosis effect has a positive relationship with the penetration of cutting fluid in the cutting zone and cutting performance. The results presented in this study are of great significance for understanding electroosmosis effect on the

lubricant penetration mechanism to perfect the micro-capillary lubrication theory and provide reference for improving the efficiency of cutting fluid.

Key words：Electrokinetic effect；Electroosmotic flow；Charged particle；Water-based cutting fluid；Cutting performance

0　前言

应用切削液的主要目的包括提高工件表面质量，减少刀具磨损以及提升生产效率等。加工过程中，切削液被施加于刀具与工件接触区，并且在大气压力和毛细力的影响下，切削液通过刀-屑界面毛细管的动态网络向切削区内部渗透[1]；切削液的应用可减小第二剪切区刀具与切屑表面间的粘结距离，从而减小剪切力[2]；此外，切屑自身裂缝是切削液的另一个渗透入口，可加快第一剪切区热量的消散[3]。除上述毛细渗透润滑理论外，Rehbinder效应可通过添加剂和微裂纹的相互作用促进工件材料的去除[4, 5]；Marangoni效应产生的毛细力驱使切削液远离高温区域，导致反向渗透[6]。然而，现有研究中切削液渗透的机理主要针对大气压力和表面张力驱动效应。为进一步完善毛细渗透润滑理论，作者提出了一种新颖的由切削过程中的荷电粒子发射现象所诱发的切削液电动渗透效应。

近年来，研究人员设计并应用透明刀具对纯铅、纯铝和纯铜进行切削加工，探究了刀-屑接触区存在的毛细管网络对润滑液渗透的影响[7, 8]。相关结果表明刀-屑接触区接触面上存在成束的毛细管，润滑液通过这些毛细管向内渗透并润湿接触界面，促进润滑膜的形成[7, 9]。此外，切削过程中工件的第一剪切区存在剪切和断裂失效现象，在刀具、切屑和已加工表面之间的主摩擦区和次摩擦区均发生了较高接触应力的摩擦学相互作用，可引起接触面的摩擦生电和毛细管中的荷电粒子发射现象[10, 11]。刀具和工件材料间的功函数差异、碎片转移方向和固有缺陷（如空穴、微裂纹等）均可影响摩擦生电性能[12-14]。此外，由摩擦产生的摩擦生电电势还与材料的电阻率相关，当使用金刚石刀具划擦聚合物材料时，该电势可达1 kV以上[15]；而电阻相对较低的铁（盘）-碳钢（销）的摩擦生电电势仅为几十微伏，且随着碳含量增加，销的带电极性由随机向负电性转变[16]。值得注意的是，摩擦生电电势可以在接触区狭缝中形成一个极强的径向电场，其中的初始低能电子在此径向电场加速下轰击中性分子，最终引起电子雪崩并伴随有摩擦微等离子体的产生[17]。接触区狭缝中所发射荷电粒子的强度通常需要在真空

或特殊气氛条件下利用通道电子倍增器进行测量[18, 19]，且在不同材料中的发射强度规律为绝缘体>半导体>导体[20]。对于复杂工况，可利用法拉第离子收集器辅助外部偏置电压的方法来捕获特定极性的荷电粒子[21]。Govindaraj使用硬质合金刀具分别加工低碳钢、铜和不锈钢时，在法拉第收集器施加±100 V的偏置电压以测量切削区荷电粒子的极性和发射强度。研究结果表明荷电粒子的发射特性与工件材料的力学和电学性能紧密相关[11]。然而，与材料和加工参数紧密相关的荷电粒子在刀-屑/工件接触区所产生的自激轴向电场特征却鲜有研究。事实上，荷电粒子可通过影响摩擦副表面所形成润滑膜性质而在减少摩擦和磨损方面发挥重要作用[22]。此外，作者通过四球摩擦磨损试验研究表明，不同电渗性能润滑液可影响磨损表面摩擦膜的形成[23, 24]。因此，了解切削区自激电学性能与切削液电渗的关联，进一步探讨自激电学性能差异对切削液渗透机理的影响至关重要。

当溶液接触例如金属、石英以及自然界中的大部分固体材料表面时，材料表面基团的解离或离子的特性吸附效应使得材料表面电荷一般为负电性，并形成双电层[25, 26]。毛细管电渗是电场作用于固/液界面双电层（包括扩散层和固定层）中扩散层离子而产生的一种对毛细管中溶液的电动效应[27]。产生的电渗流使溶液本体相对于固定的毛细管壁面朝一个确定的方向移动，通常应用于液相色谱分离和电动微泵等领域[28, 29]。Chen[30]系统研究了高压电渗泵在微柱液相色谱中的应用，并设计了一款对于纯水和甲醇可输出压力至少为5 MPa，稳定流量在1 μL/min的电渗泵。其研究表明，通过调节毛细管两端的轴向驱动电场可定量控制电渗流的流量和压力。仲武等[31]研究发现，在直径25 μm毛细管两端施加800 V/cm的轴向电场后，去离子水可产生约11 mm/s的电渗流，这与基于刀-屑接触区毛细管渗透模型得到的研究结果相类似[32]。

切削液在刀-屑接触区毛细管中的电驱动渗透性能（如图1a、b所示）主要取决于毛细管两端的轴向电场以及固-液界面的双电层特性。双电层的形成主要是由于毛细管壁产生的表面电荷，溶液中与表面电荷极性相同的离子被排斥，极性相反的离子被吸引，以屏蔽表面电荷，在靠近毛细管的内表面形成带电区域[27]。由于离子间的强静电效应，双电层中固定层离子是固定不动的，而扩散层离子在电场的作用下沿电场力方向移动。运动的扩散层离子

在溶液粘度的影响下驱动毛细管中的溶液本体一齐运动，最终形成电渗流 [33]，如图 1c 所示。一般情况下，提高轴向电场强度 [34] 和溶液的 pH 值 [35] 可增强电渗流。此外，两性离子表面活性剂 [36]（如 3-[(3-胆 固 醇 氨 丙 基)- 二 甲 基 氨 基]-1- 丙 磺 酸（3-[(3-cholamidopropyl)-dimethylammonio]-1-propanesulfonate, CHAPS）和月桂亚氨基二丙酸二钠（Sodium Lauriminodipropionate, SLI））可在不改变方向的前提下提高电渗流，但阳离子表面活性剂 [37]（ 如 十 六 烷 基 三 甲 基 溴 化 铵（Cetyltrimethylammonium bromide, CTAB）和十四烷基三甲基溴化铵（Tetradecyltrimethylammonium bromide, TTAB））可通过其分子在毛细管壁面的特性吸附来改变电渗流方向 [38]。由此可知，表面活性剂由于其特殊的分子结构，可在固-液界面形成吸附层，改变双电层结构，对电渗流调节产生显著影响 [39, 40]。切削液的电渗特性为了解电渗效应的调控机理提供了重要依据。基于此，可提升对润滑液在加工接触区渗透的认知，并作为提高润滑液在不同加工工况下使用效率的参考。

(a) 切削区示意图

(b) 切削液
在切削区毛细管中的渗透

(c) 切削液在材料表面形成电渗流示意图
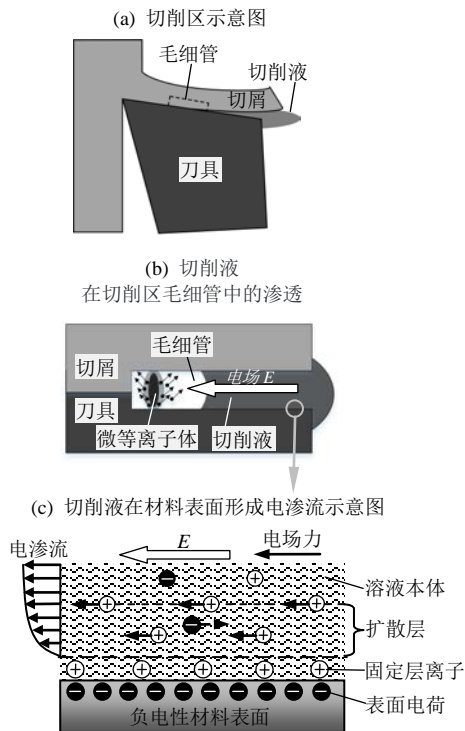
图 1　切削液在切削区材料表面电渗流的形成原理示意图

本研究中，首先建立了电渗流速度测量装置，考察了切削液中的电渗添加剂和毛细管两端轴向电场强度对切削液在 AISI 304 不锈钢毛细管和 PE 绝缘毛细管中电渗流的影响。其次在切削试验中，采用法拉第收集板与偏置电场板相结合的方法检测了由后刀面-已加工表面间隙中逃逸的荷电粒子，这既可避免检测过程中切屑的干扰，又可有选择性地采集特定电性粒子。再次，通过荷电粒子的发射强度计算出了接触区毛细管中的自激轴向电场强度，并考察了影响轴向电场的相关因素。最后，通过切削试验分析了不同电渗性能切削液对切削力、表面粗糙度和刀具磨损的影响，探讨了切削液在切削区毛细管中产生电渗效应的机理及调控手段。

1　试验材料与试验方案

1.1　切削液的制备

本文选用去离子水作为基础切削液以避免商用切削液中已有离子的干扰。另外选用月桂亚氨基二丙酸二钠（Lauriminodipropionate, SLI）和十六烷基三甲基溴化铵（Cetyltrimethylammonium bromide, CTAB）作为电渗添加剂。将电渗添加剂加入到基础液中，超声分散 30 分钟制备成浓度分别为 0.05 mM（mmol/L）、0.1 mM、0.2 mM 和 0.3 mM 的切削液。所用药品均为分析纯，购自上海麦克林生化科技有限公司（Shanghai Macklir Biochemical Co., Ltd., China）。其中含有 SLI 的为电渗促进型切削液，含有 CTAB 的为电渗抑制型切削液。所用切削液的成分以 m 及两种添加剂的化学分子式列于表 1.

表 1　切削液的成分以及 SLI 和 CTAB 的化学分子式

润滑液类型	成分
基础润滑液	去离子水
电渗促进型切削液	去离子水 + 0.05 mM SLI
	去离子水 + 0.1 mM SLI
	去离子水 + 0.2 mM SLI
	去离子水 + 0.3 mM SLI
电渗抑制型切削液	去离子水 + 0.05 mM CTAB
	去离子水 + 0.1 mM CTAB
	去离子水 + 0.2 mM CTAB
	去离子水 + 0.3 mM CTAB

（ SLI ）

（ CTAB ）
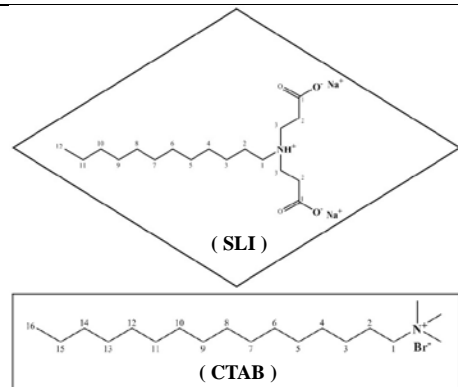
1.2　毛细管电渗试验

为分析切削液在刀-屑接触区毛细管内的电渗特性，采用 AISI 304 不锈钢和 PE 毛细管对切削液电渗流速度进行了测量。图 2 示出了毛细管电渗流速度测量原理示意图。两注射器针筒分别垂直放置

于绝缘底座两侧，中间与内/外径为 1/1.5 mm、长度 40 mm 的毛细管连接。切削液由一端针筒加入，在重力作用下最终达到两侧针筒液面平齐。采用输出电压连续可调的高压静电发生器（EST802A，北京华晶汇科技有限公司）在毛细管两端对切削液施加轴向电场。将高压静电发生器的正电压输出端插入左侧针筒切削液中，另一侧切削液接地。本试验所用电压分别为 2 kV 和 4 kV，由电场计算公式 $E=U/d$ 可知，毛细管两端的轴向电场强度分别约为 500 V/cm 和 1000 V/cm，超过了启动毛细管电渗所需电压（150 V/cm）[41]。每次测试持续 30 分钟，根据切削液的移动体积计算出电渗流速度。试验在室温（25℃）下进行，每次测试重复 3 次，并取平均值。
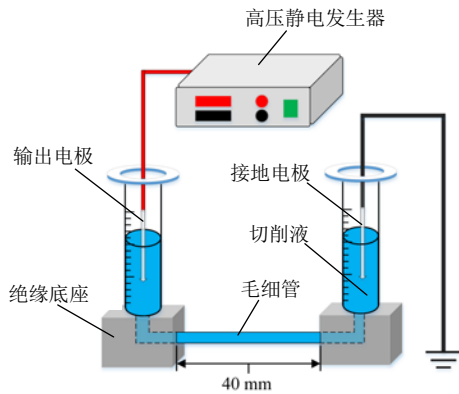
图 2 切削液电渗流测量系统示意图

1.3 切削区荷电粒子检测

刀-屑/工件接触表面的摩擦生电静电势导致切削区毛细管中存在很强的径向电场，其中的电子在此径向电场的加速作用下轰击中性气体分子而产生电子雪崩并激发出不同极性的荷电粒子。电子、负电粒子和正电粒子组成的荷电粒子群中有一部分在静电力作用下不可避免的被吸引至壁面中和，其余部分向毛细管开口端移动，在毛细管两端形成自激发轴向电场。为探究车削加工中荷电粒子发射强度的变化规律，分别考察了工件材料与加工参数的影响，并对不同极性荷电粒子的发射强度特征进行了研究。

采用法拉第粒子收集板测量常态下荷电粒子的发射强度。法拉第收集板是由铜或银等优良导体材料制成的薄片，用来捕获荷电粒子[21]。发射出的荷电粒子由于能量低（通常为 10 到 200 eV），如不加干预会向四面八方散射。在法拉第收集板一侧提供一偏置电场，对不同极性荷电粒子进行筛选，原理如图 3 所示。利用这一原理，可分别检测正电（正离子）或负电（电子、负离子）粒子的强度。如图 3b 所示，当给法拉第收集板提供负偏置电场时，负荷电粒子被吸引至收集板而正荷电粒子被排斥。当施加如图 3c 所示的正偏置电场时，检测原理类似。

这些收集到的荷电粒子在与收集板连接的电路中产生电流，应用最低可测量 1 飞安的精密静电计检测这种超低离子电流。
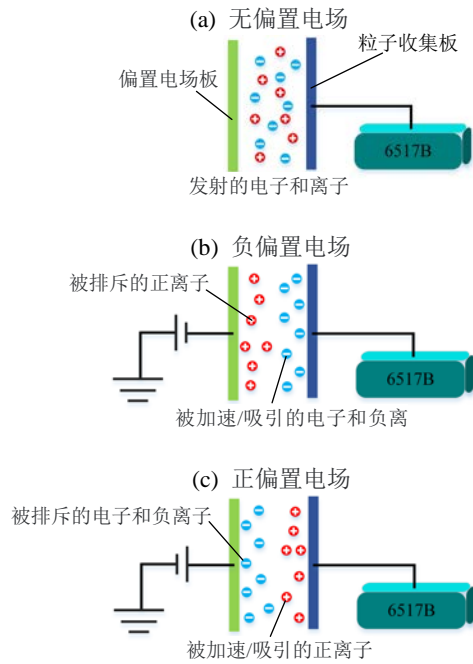
图 3 大气气氛下荷电粒子发射强度测量原理示意图

(a) 测量系统

(b) 工件形状
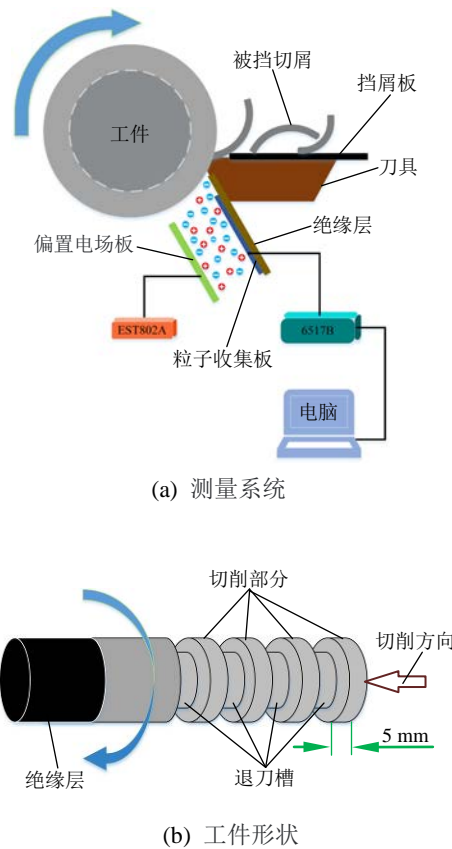
图 4 用于测量荷电粒子发射强度的工件形状和测量系统示意图

在主后刀面设置 0.05 mm 厚的银片作为法拉第

收集板。为防止切屑对试验的影响，工件每隔 5 mm 设置一个退刀槽来控制切屑长度（工件形状如图 4b 所示），并且在前刀面上方设置挡屑板，防止切屑掉落至检测区，如图 4a 所示。收集板与主后刀面通过绝缘层隔离，以防止荷电粒子通过刀具流失。收集板上边缘与切削刃的距离保持在 4 mm，确保加工过程中工件与收集板无接触。采用静电计（Keithley，6517B）测量电路中的超低离子电流。为分别测量正/负荷电粒子强度，在法拉第收集板上施加强度为 ±700 V/cm 的偏置电场，偏置电场板由形状与收集板相同的铜片制成。偏置电场所需电压由高压静电发生器（EST802A，北京华晶汇科技有限公司）提供。荷电粒子发射强度与偏置电场无关，偏置电场的施加只起到筛选粒子极性的作用。图 4a 还示出了测量系统中的电路连接以及数据采集方法。

由于荷电粒子的发射产生于切屑与工件的最初分离阶段，荷电粒子的外逸强度基本不受实际加工时切削液的影响。荷电粒子电流强度测量试验系统如图 5 所示。试验在 CAK6150D 精密车床上进行，所用工件为直径 60 mm，切削长度 5 mm 的 AISI 304 和 PE 棒料。测试前，对所有工件进行切削深度为 2 mm 的预加工处理，以保证表面均匀，确保测试时的切削连续性。所用刀具为 PVD-TiAlN 硬质合金涂层刀具（CCMT09T304N-SU，住友电气，日本）。每组测试均使用全新的工件和刀具，以保持相同的试验环境。试验条件汇总于表 2，加工时间段内所测电流平均值作为单次测量结果。每组试验做三次并取平均值。
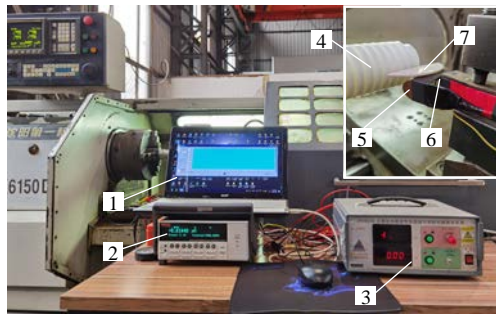
图 5 荷电粒子电流强度检测试验台

1. 电脑 2. 精密电流表 3. 高压静电发生器 4. 工件 5. 偏置电场板 6. 刀具 7. 挡屑板

1.4 车削试验

为揭示轴向电场对切削过程中接触区毛细管内切削液润滑性能的影响，在 CAK6150D 型数控车床上进行了基于水基切削液电渗调控的切削加工性能试验研究，试验装置如图 6 所示。采用 AISI 304 不锈钢和 PE 棒料作为加工工件，尺寸为 Φ60 mm×310 mm。为保证试验中加工表面性能参数的一致性，在试验前对所有工件毛坯预先切除 2 mm。采用硬

质合金刀片（CCMT09T304N-SU，住友电气，日本）进行切削加工。供液选择气压 0.2 MPa、流量 50 ml/min 的微量润滑方式，对比考察去离子水、电渗促进型切削液（SLI 切削液）和电渗抑制型切削液（CTAB 切削液）润滑下的切削力和工件表面粗糙度。每组试验均采用新的工件及刀片进行加工以保证切削环境相同。切削参数见表 2。

不同润滑工况下，在第 4 刀对切削力和表面粗糙度进行测量（每刀切削长度 125 mm）。切削力采用 Kistler 9129A 型（瑞士奇石乐）三向测力仪测量，F_X、F_Y 和 F_Z 作为主要切削力参数，其中 F_X 是切深抗力，F_Y 是切向力，F_Z 是进给力，利用公式 $F_R=(F_X^2+F_Y^2+F_Z^2)^{1/2}$ 计算的合力 F_R 作为不同润滑工况下切削力的最终测试结果。工件表面粗糙度 Ra 值利用便携式粗糙度仪（SJ-210，日本三丰）进行测量，测量时在加工后工件轴向等距取五个测量点。最后，采用配备了能谱仪的扫描电子显微镜（SEM，EVO18，蔡司，德国）分析不同工况下刀具的磨损形貌，揭示磨损机理。每组试验平行进行三次，最后取平均值。

表 2 试验条件

机床	CAK6150D 型精密车床
切削刀具	硬质合金刀具（CCMT09T304N-SU，日本住友）
刀柄	SCLCR2020KO9C
工件材料	不锈钢（AISI 304）；聚乙烯（PE）；切削速度：44.6、63.1 和 89.4 m/min；
切削参数	切削深度：0.25、0.5 和 1 mm；进给速度：0.25 mm/r；切削长度：5 mm
润滑条件	干切削
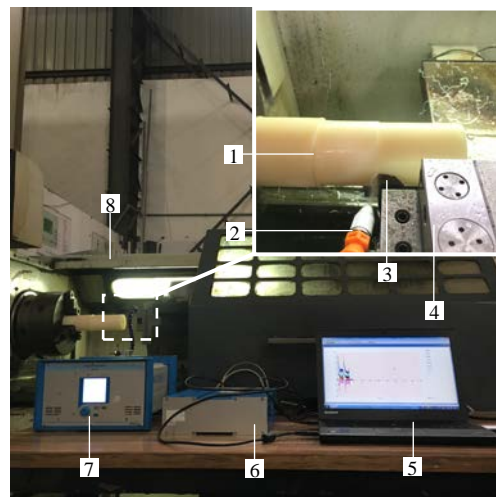
图 6 切削力检测试验台

1. 工件 2. 喷嘴 3. 刀具 4. 测力计 5. 电脑 6. 数据采集器 7. 电荷放大器 8. 精密车床

2 试验结果分析

2.1 毛细管电渗流特性

2.1.1 电渗添加剂的影响

含 CTAB 和 SLI 的切削液在 AISI 304 和 PE 两种毛细管中的电渗流速度分别示于图 7a、b 中,此时毛细管两端的轴向电场强度为 500 V/cm,其中去离子水的试验结果示于图中作为对比。由图可知,同一电场强度下,去离子水在两种毛细管中的电渗流速度分别达到了 $0.65×10^{-4}$ μL/ms(AISI 304)和 $1.07×10^{-4}$ μL/ms(PE),并且方向与电场线方向一致。说明当去离子水与毛细管壁面相接触后,由于离子的选择性吸附,壁面解离等原因产生于毛细管壁面的表面电荷极性为负,致使扩散层中起主导作用的为正离子。施加轴向电场后,在粘性作用下扩散层带动溶液本体沿电场线方向移动产生电渗流。此外,不同材料毛细管中的电渗流速度绝对值均随电渗添加剂浓度的增加而迅速增大,表明电渗添加剂分子在毛细管内壁面进行了有效吸附,改变了双电层结构,最终影响了电渗流性能。

如图 7 所示,SLI 切削液在两种毛细管中的电渗流方向始终与电场线方向一致,并且电渗流速度随浓度而升高。当浓度达到 0.2 mM 时,在 AISI 304 毛细管中的电渗流速度达到 $0.89×10^{-4}$ μL/ms,相比于去离子水提高了 36.9%;在 PE 毛细管中的电渗流速度达到了 $1.64×10^{-4}$ μL/ms,相比于去离子水提高了 53.2%。这主要是因为每个 SLI 分子同时含有一个含氮的阳离子基团和两个羧酸阴离子基团。SLI 分子中的阳离子基团在电荷间静电力作用下被带负电荷的毛细管壁牢固吸附,形成额外的固定层。两个羧酸阴离子基团则留在溶液中,不随溶液而移动,效果相当于使毛细管壁上的负电荷数量增加一倍,进而增加了扩散层中的正离子浓度,最终提高了电渗流速度[23]。

当 CTAB 切削液应用时,尽管在两种毛细管中的电渗流速度绝对值都随浓度而增加,但电渗流方向发生了改变(与电场线方向相反)。0.2 mM 的 CTAB 切削液在 AISI 304 和 PE 毛细管中的电渗流速度分别达到了 $-0.92×10^{-4}$ μL/ms 和 $-1.45×10^{-4}$ μL/ms。这主要是因为 CTAB 分子中的季铵盐阳离子基团带正电荷[42],致使 CTAB 分子在静电力作用下紧密吸附在毛细管内壁上[43]。CTAB 分子在毛细管壁上的吸附量随浓度而逐渐增加,直至整个带负电荷的毛细管内壁面被覆盖,形成单分子吸附层;与此同时,毛细管壁上的负电荷密度持续减小,直至为零,电渗流相应减弱直至消失。随 CTAB 浓度

的继续增加,其分子中疏水链相互作用形成毛细管壁上的第二吸附层,研究表明[41],当 CTAB 浓度达到 0.05 mM 时,第二吸附层便开始形成(此时扩散层中的离子电性由正转负,电渗流方向反转)。当 CTAB 浓度进一步增加,反向电渗流速度便持续提高,当浓度达到 0.2 mM 时,电渗流趋于稳定。

在图 7 中我们还可发现,不同切削液在绝缘的 PE 毛细管中所产生的电渗流均高于金属的 AISI 304 毛细管。其中去离子水、0.2 mM 的 SLI 和 CTAB 切削液在 PE 毛细管中的电渗流速度分别比在金属毛细管中提高了 64.6%、84.2% 和 57.6%。这种现象产生的原因可能是在与溶液相接触后,绝缘性更优的 PE 材料壁面可产生更多的负极性表面电荷,致使扩散层中的正离子数量更多。当在毛细管两端施加相同轴向电场后,可移动的扩散层正离子数量更多的绝缘毛细管中可产生更强的电渗效应。

由图 7a、b 可知,当电渗添加剂浓度达到 0.2 mM 后,不同材料毛细管中的电渗流速度均趋于稳定,不再随浓度而明显增加。这可能是电渗添加剂分子在毛细管内表面的有效吸附趋于饱和所致[44, 45]。电渗添加剂本质是表面活性剂,切削液的表面张力和接触角随电渗添加剂浓度的升高而一直降低,表明切削液液滴自身的润湿渗透能力在持续提升。但是当浓度由 0.2 mM 增至 0.3 mM 后,电渗流速度无明显变化,可证明在电渗添加剂浓度较低条件下,切削液在毛细管中的渗透主要受电渗效应支配而非切削液本身的电润湿现象。
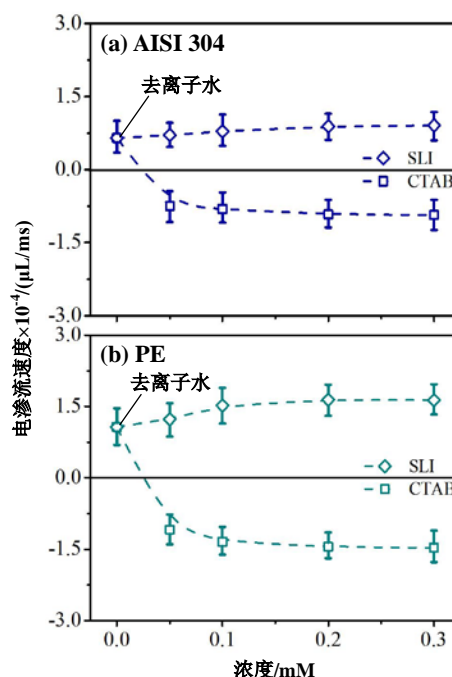
图 7 电渗添加剂和毛细管材料对电渗流速度的影响,与电场线方向一致时电渗流速度值为正

2.1.2 轴向电场强度的影响

图 8a、b 示出了去离子水、0.2 mM 的 CTAB 和 SLI 切削液在两种材料毛细管中电渗流速度随两端轴向电场强度的变化。由图可知，随毛细管两端轴向电场强度从 500 V/cm 增至 1000 V/cm，不同切削液在金属和绝缘毛细管中的电渗流速度绝对值均增加。这是因为随电场强度的增加，扩散层中每个正离子所受电场力增强，导致整个扩散层受力增加，最终以更高的速度带动溶液本体移动。当毛细管两端电场强度增大后，CTAB 切削液产生的反向电渗流在方向不变的条件下继续增加，表明轴向电场不影响双电层性质，只对扩散层离子所受电场力有调节作用。

对比图 8a 和 b，可以发现不同切削液在 PE 毛细管中电渗流强度的增加幅度明显高于在 AISI 304 毛细管中。当电场强度提升后，去离子水在 PE 毛细管中电渗流的增加幅度比在 AISI 304 毛细管中的增加幅度高出 57.2%（PE 毛细管中的增加幅度 75.7% 减去 AISI 304 毛细管中的增加幅度 18.5%）；SLI 和 CTAB 切削液的这一升高数值分别为 86.4% 和 93.3%。产生这一差距的主要原因是与同一溶液相接触后，绝缘材料毛细管产生的表面电荷数量高于金属材料毛细管，导致绝缘材料毛细管扩散层中的离子浓度更高，施加在扩散层的电场力受电场强度变化的影响更为明显。
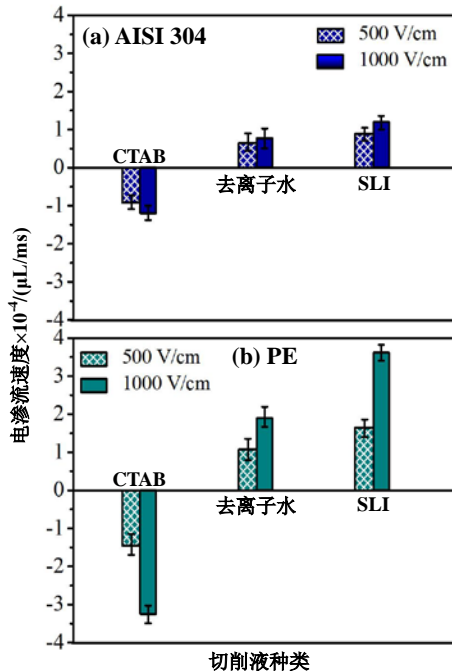
图 8 毛细管两端轴向电场强度对电渗流速度的影响，电渗添加剂浓度为 0.2 mM，与电场线方向一致时电渗流速度值为正

2.2 切削区荷电粒子发射强度及其形成的自激发轴向电场

2.2.1 荷电粒子发射强度

图 9 和图 10 分别示出了切削 AISI 304 和 PE 时，切削深度和切削速度对切削区正、负荷电粒子发射强度的影响。从图中荷电粒子所诱发电流强度的变化不难发现，荷电粒子发射强度随切削参数的增加均呈现单调增大的趋势。从两图中可以看出，在本文所用切削参数下，荷电粒子发射强度范围集中在 $1 \times 10^{-9} \sim 1 \times 10^{-8}$ A。切削区荷电粒子主要受加工过程中产生于两接触面的摩擦生电静电势诱导而产生。当切削区两接触表面分别带上等量异种电荷后，可在接触区间隙中形成强度极高的径向电场（因为接触区间隙很小，为微米级别），此径向电场可作为间隙中初始低能电子（由于热电子发射或场致电子发射而产生）的加速场，被加速的电子高速轰击间隙中的中性分子，被轰击后的每个中性分子可额外产生一个正离子和一个负离子，可在间隙中形成微等离子体[46]。正离子、负离子和电子共同组成了切削区的外逸荷电粒子[11]。
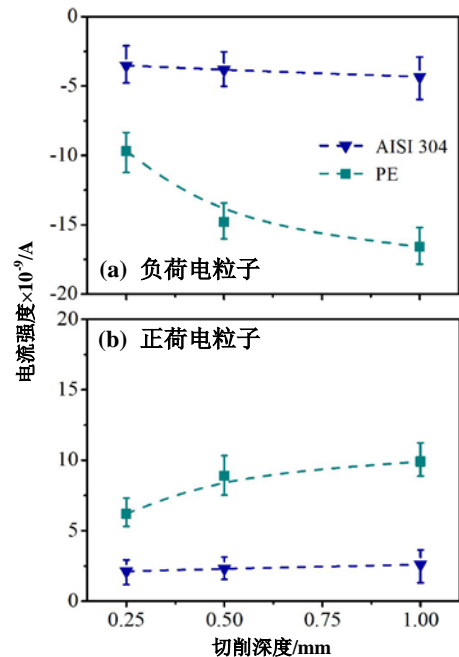
图 9 切削不同材料时切削深度对负/正荷电粒子发射强度的影响

如图 9 所示，当切深由 0.25 mm 增至 1 mm 后，两工件的负荷电粒子发射强度分别由 -3.52×10^{-9} A 增加到 -4.34×10^{-9} A（AISI 304）以及由 -9.7×10^{-9} A 增加到 -16.6×10^{-9} A（PE）；正荷电粒子发射强度由 2.11×10^{-9} A 增加到 2.6×10^{-9} A（AISI 304）以及由 6.2×10^{-9} A 增加到 9.9×10^{-9} A（PE）。这是因为切削深度增加导致了经受剪切变形的切屑体积增大，提高了材料的电子发射强度以及两接触表面的摩擦生

电静电势。同时，由于后刀面与切屑表面之间的划擦压力升高，刀具与切屑的摩擦接触面积和摩擦剧烈程度增大而产生了更为强烈的摩擦电子发射。在此综合作用下，荷电粒子发射强度随切削深度而增大。

由于荷电粒子发射强度受材料的功函数、原子序数和电学特性的影响[47]。每种材料都具有特定的原子（功函数、原子数）、物理、电学和机械特性，这些特性可影响具体工况下的荷电粒子发射强度。此外，通过研究发现材料的电阻率对荷电粒子发射强度的影响起主导作用，其次是材料的硬度和极限强度等。从图 9 中还可发现，切削绝缘材料时的荷电粒子发射强度远大于切削金属材料时（平均高出3 倍），其中两种工件材料的电阻率和硬度示于表 3。

表 3 工件材料的电阻率和硬度

材料	电阻率 (nΩ.m)	硬度
AISI 304	720	201 (布氏硬度)
PE	≥1×10^{19}	45 (球压硬度)
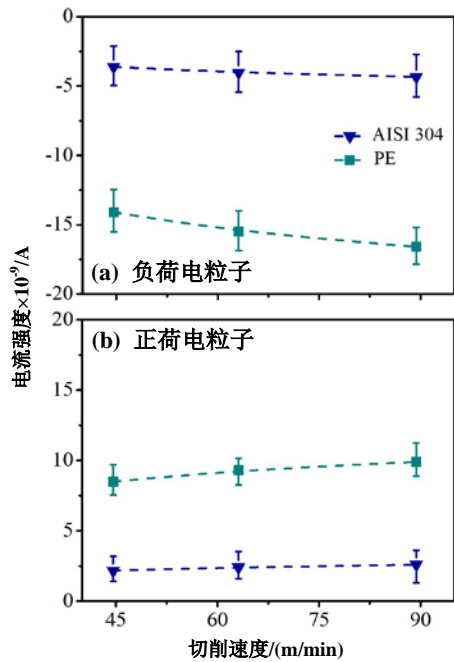
图 10 加工不同材料时切削速度对负/正荷电粒子发射强度的影响

图 10 所示为切削深度 1 mm，进给速度 0.25 mm/r 时，切削区正负荷电粒子发射强度随切削速度的变化情况。由图可知，当切削速度由 44.6 m/min 增大到 89.4 m/min 后，切削 AISI 304 时负荷电粒子发射强度增加了 19.9%，正荷电粒子发射强度增加了 19.8%；切削 PE 时负荷电粒子发射强度增加了17.7%而正荷电粒子发射强度增加了 16.5%。相比于低速切削，较高切削速度下，材料的变形和剪切速率更大，产生的更高热量和摩擦生电静电势导致了更强的荷电粒子发射。此外，法拉第收集板捕获荷电粒子的数量为其发射强度，切削速度提高后单位

时间间隔内刀具划擦切屑和工件的距离更长，由此激发的更多荷电粒子被收集，使得最终检测电流增强。

从图 9 和图 10 中不难看出，切削两种工件时的负荷电粒子发射强度均显著高于正荷电粒子。这是因为电子是材料在机械损伤过程中接触区发射的最主要粒子，且发射的负荷电粒子包括电子和负离子，而发射的正荷电粒子只包括正离子[11, 48]。本文几乎在所有切削条件下都可观察到负荷电粒子发射强度处于优势，这与 K. Nakayama 等[49]的研究结果一致。

2.2.2 自激发轴向电场

切削加工过程中，切削区间隙内产生的大量荷电粒子迅速向间隙开口端移动，流出的荷电粒子被法拉第板收集而形成电流[11]。如图 11 所示，荷电粒子从产生到被收集所经过的路径被定义为荷电粒子流通道。根据逸出电流强度 $E=\rho J$ 可计算得到毛细窄缝两端的自激发轴向电场强度，其中 ρ 为毛细窄缝中的空气电阻率（Ω·m），J 为逸出粒子的电流密度（A/m^2）。每个毛细窄缝逸出粒子的电流密度为 $J=I/nA$，其中 I 为通过法拉第收集板测得的净电流强度（负电流强度减去正电流强度），A 是单个毛细窄缝的横截面积，n 为刀-屑接触区毛细窄缝的数量。

图 11 同样示出了切屑表面微观形貌，其表面沟槽可作为切削区毛细管以供切削液向内渗透[32]。为便于计算且在合理范围内，计算轴向电场时取 5 μm 作为毛细管平均半径，且假定不同切削参数下切屑表面有效毛细管数量为 10，则单根毛细管内自激轴向电场强度为 $E=\rho I/10A$。考虑切削液存在时，采用本文所用切削液电阻率（1×10^3–1×10^4 Ω·m）进行计算，计算结果范围为 1.5×10^2 V/cm ~ 1.09×10^3 V/cm，满足毛细管电渗所需电场强度（150 V/cm）[41]。
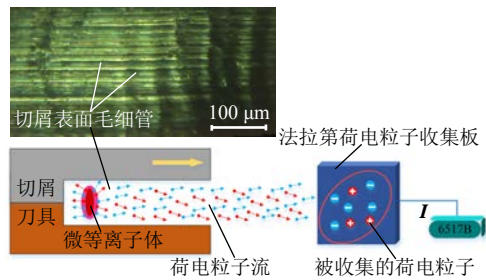
图 11 切削区毛细管中荷电粒子发射产生轴向电场的计算原理图

图 12 描述了切削深度和切削速度对两种工件材料毛细管中自激轴向电场强度的影响。从图中可以看出，自激轴向电场强度随切削参数而增加，且PE 毛细管中产生的自激轴向电场强度明显高于AISI 304 毛细管。在切削深度 1 mm，切削速度 89.4 m/min，进给速度 0.25 mm/r 条件下，PE 毛细管中

的自激轴向电场强度比金属毛细管中高 284.2%。此外，随切削参数的增加，绝缘材料毛细管中自激轴向电场强度的增速也远快于金属毛细管。产生这种现象的原因可能是绝缘工件的阻抗远大于导体工件，在相同切削参数下，毛细管中径向电场对切削绝缘材料时荷电粒子发射的刺激远高于切削金属材料时，最终阻抗更高的材料中形成了较强的自激轴向电场且对切削参数的变化更为敏感。值得一提的是，由于毛细管逸出的荷电粒子整体呈负电性，致使自激发轴向电场方向始终指向毛细管内侧。
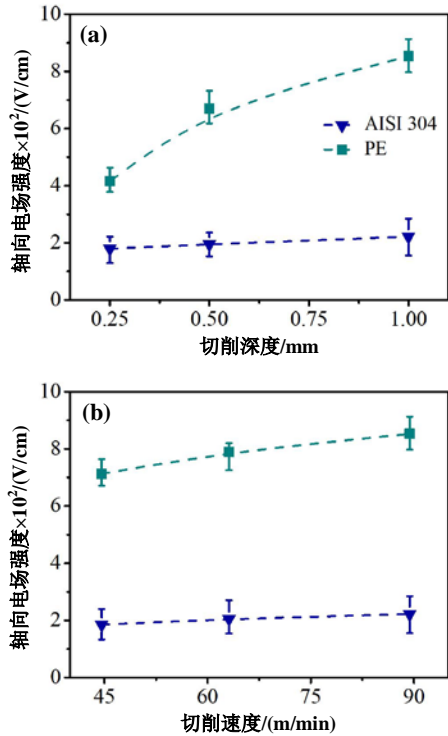
图 12　切削不同材料时切削参数对轴向电场强度的影响

2.3　车削性能

2.3.1　电渗添加剂的影响

图 13 示出了电渗添加剂类型和浓度对切削金属和绝缘工件（AISI 304 和 PE）时切削力和表面粗糙度的影响。电渗添加剂种类为 SLI 和 CTAB，浓度范围为 0.05-0.3 mM，切削深度 1 mm，切削速度 89.4 m/min，进给量 0.25 mm/r。从图中可以看出，与去离子水相比，SLI 的加入显著降低了切削力，改善了表面质量，而 CTAB 切削液的使用则导致了较高的切削力和较差的表面质量。产生这种差异的原因是 SLI 的添加增大了正向电渗流，促进了更多的切削液渗透到切削区间隙中参与润滑。而 CTAB 的加入使得电渗流反向，减少了切削液的渗透量，导致切削区润滑不足，因此得到了较差的切削性能。随着浓度的增加，SLI 切削液润滑下的切削力和表面粗糙度均先减小后趋于稳定。与去离子水相比，0.2 mM SLI 切削液对 AISI 304 和 PE 的切削力分别降低了 31.1% 和 31.2%，表面粗糙度分别降低了

31.7% 和 6.3%，显现出更好的切削性能。而在 0.2 mM CTAB 切削液润滑条件下，金属和绝缘工件的切削力分别增加了 23.7% 和 27.4%，表面粗糙度也分别增加了 25% 和 6.4%，此时的切削性能较差。从图中还可看出，在电渗添加剂浓度升高的初始阶段，切削性能随浓度变化较为敏感，这是因为电渗添加剂浓度升高可增大切削液中的分子浓度，增强了添加剂分子在毛细管壁面的吸附量，提高了其对切削区毛细管中切削液电渗流的调控强度。随浓度的进一步提高，切削力和表面粗糙度的变化趋缓，这是由于添加剂分子在毛细管壁面的有效吸附趋于饱和的缘故[50]。

对比金属和绝缘工件，可以发现电渗添加剂对绝缘工件切削性能的影响高于对金属工件，这与前述电渗流速度的趋势一致。此外，当切削净荷电粒子发射强度高的材料时，切削区毛细管中可产生更强的自激轴向电场。结果表明，在更强自激轴向电场作用下，毛细管电渗效应增强，可提高电渗添加剂对切削液在切削区间隙中渗透的调节能力。最终导致不同切削液润滑条件下，切削高荷电粒子发射强度材料时的切削性能差异相比于切削低荷电粒子发射强度材料时更为明显。
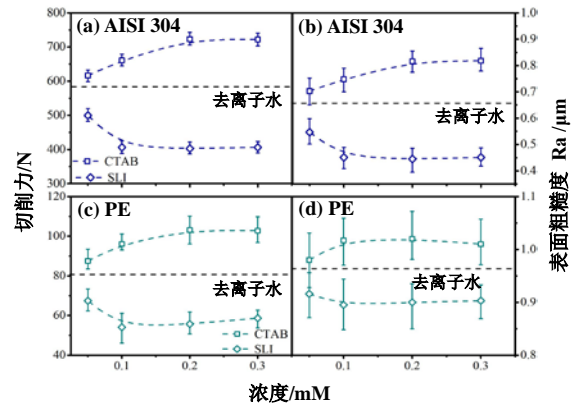
图 13　切削不同材料时电渗添加剂对切削力和表面粗糙度的影响

2.3.2　切削深度的影响

图 14 描述了当使用 0.2 mM 电渗添加剂，将切削深度从 0.25 mm 增加到 1 mm 时，切削深度对金属和绝缘工件切削力和表面质量的影响。切削速度和进给量分别为 89.4 m/min 和 0.25 mm/r。可以发现，切削力和表面粗糙度均随切削深度而提高，且不同切削深度时，SLI 切削液润滑下的切削力和表面粗糙度均低于去离子水润滑下的，而 CTAB 切削液润滑时得到了相反的结果。切削深度的增大提高了切削难度，使切削区的摩擦更为剧烈，从而增大了切削力。另一方面，摩擦程度的加大增强了接触区两接触面间的电荷转移，促进接触界面毛细管中的荷电粒子发射，最终提高了毛细间隙中的自激发

轴向电场强度。在电渗效应影响下，电渗添加剂对电渗流的调控效果随切削深度的提高而增强，最终导致不同切削液润滑下的切削性能差异随切削深度而增大。如图 14a、c 所示，当切削深度由 0.25 mm 增大到 1 mm 后，切削 AISI 304 时 SLI 和 CTAB 切削液润滑下的切削力相比于纯去离子水润滑下的降低/提高幅度分别提升了 12.7%/9.9%，此值在切削 PE 时分别为 12.8%/9.3%。表明在电渗调控下，切削深度对不同性质工件切削性能的影响具有相同趋势。

如图 14b、d 可知，不同切削液润滑下金属和绝缘工件表面质量随切削深度的变化趋势与切削力变化趋势相仿。电渗促进剂切削液的应用增进了去离子水向切削区深处的进一步渗透，减轻了刀-屑/工件间的摩擦，从而得到了较低的表面粗糙度。而电渗抑制剂的添加改变了扩散层离子所受电场力的方向，致使电渗流朝向切削区外部，阻碍了切削液的渗透，减少了参与减磨抗磨的切削液量，在接触面引起了更为强烈的摩擦，最终导致了较为粗糙的加工表面。
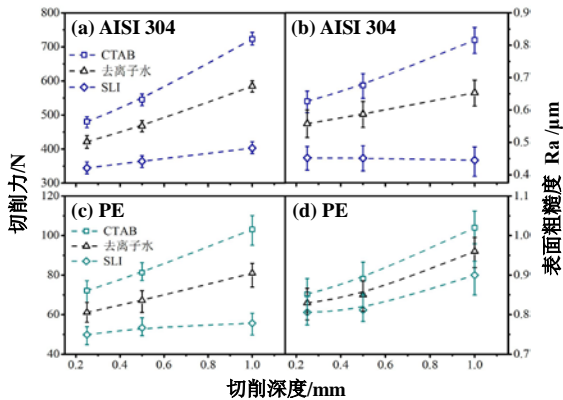
图 14　切削不同材料时切削深度对切削力和表面粗糙度的影响

2.3.3　切削速度的影响

图 15 示出了基于电渗调控下切削速度对不同切削液润滑下切削金属和绝缘材料时切削性能的影响。试验条件：电渗添加剂浓度 0.2 mM，工件为 AISI 304 不锈钢和 PE，切削深度 1 mm，进给速度 0.25 mm/r。其中去离子水的试验结果示于图中作为对比。可见，各切削液润滑条件下，切削力和表面粗糙度均随切削速度的提高而降低。进给速度保持不变时，较高的切速可以降低切屑厚度，因此获得更低的切削力。但提高切削速度后，单位时间内刀具划擦切屑的距离变长，加强了两接触面的摩擦，增进了刀-屑间电荷的转移，切削区两接触面所带等量异种电荷所形成的径向电场强度更高，激发出更强的荷电粒子发射而增强了毛细管两端的自激发轴向电场强度。电渗效应下，电渗添加剂对切削性能

的影响随切削速度而加大。

由图 15a、c 可知，当切削速度由 44.6 m/min 增大到 89.4 m/min 后，切削两材料时 SLI 和 CTAB 切削液润滑下的切削力比去离子水润滑时的降低/增大幅度分别提升了约 11.3%/10.7%（AISI 304）和 13.4%/10.1%（PE）。此外，从图 15b、d 可知，随切削速度的变化，电渗调控对两工件表面质量的影响虽然没有对切削力的影响显著，但与其变化趋势相同。应用不同电渗性能切削液时，切削速度与切削深度对切削液渗透的影响机理相似，切削参数的提高影响了切削区毛细管中的轴向电场强度，进而增强了对不同电渗性能切削液所形成电渗流的调控，影响切削区中切削液的渗透量，最终导致切削性能差异。另外，相同切削液与不同性质材料接触时产生的表面电荷差异对电渗流有明显影响，最终改变了基于电渗调控下电渗添加剂对切削性能的调节能力。
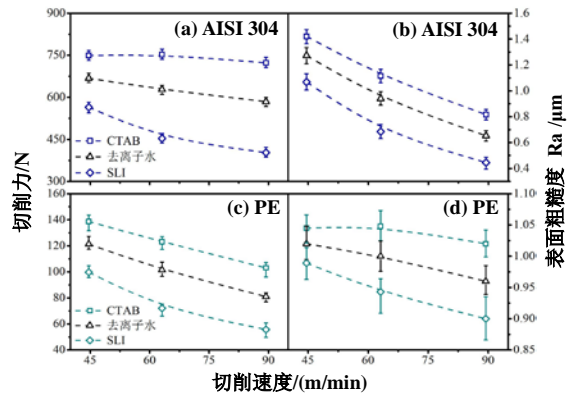
图 15　切削不同材料时切削速度对切削力和表面粗糙度的影响

2.3.4　磨损机理分析

切削液在切削区的渗透能力影响其润滑性，导致刀具刃口磨损形式和磨损表面化学成分的差异[51]。与切削绝缘材料 PE 相比，切削金属材料 AISI 304 不锈钢可以显著表征刀具刃口磨损。

图 16 为切削 AISI 304 不锈钢时，三种不同润滑条件下切削长度为 1000 mm 后刀具刃口磨损的 SEM 图像。在切削过程中，切削刃上产生了高压和热集中现象，加剧了工件与后刀面的摩擦，可导致严重的粘着磨损[52]，甚至是刀具切削刃的断裂[53]。如图 16a1 和 a2 所示，在 CTAB 切削液润滑条件下出现了微崩刃现象。这可能是由于使用 CTAB 切削液时，切削区的严重摩擦降低了切削刃的强度，表明 CTAB 切削液的润滑能力欠缺。图 16b1 和 b2 为纯去离子水润滑下的磨损表面，没有崩刃但存在严重的材料粘附现象，说明去离子水的润滑性能优于 CTAB 切削液。此外，对于 SLI 切削液，如图 16c1、c2 所示的磨损面磨损最轻，没有崩刃且粘附现象不

明显，表明其对切削接触区进行了有效的润滑。
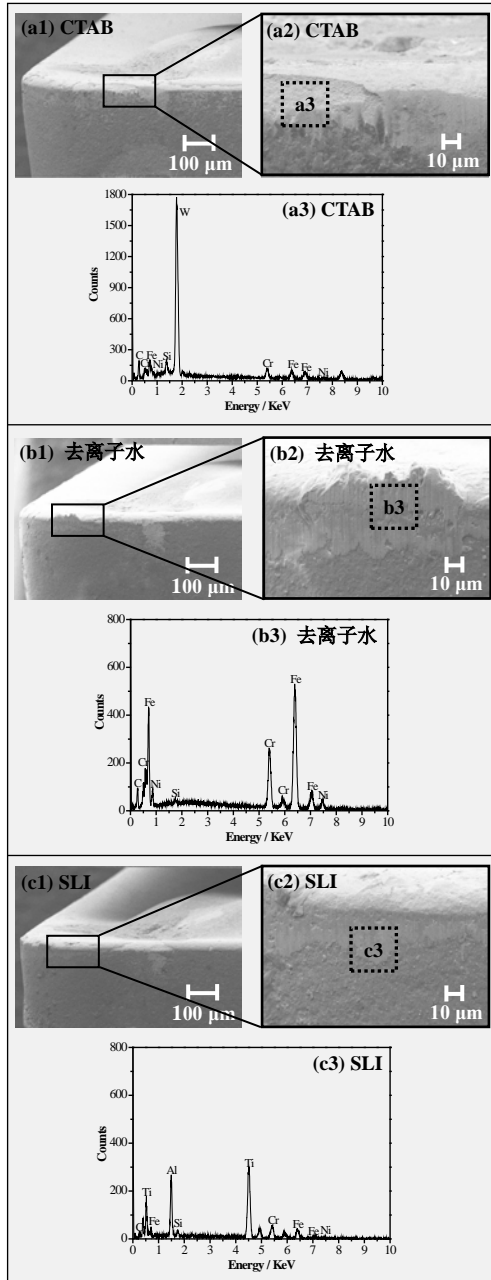
图 16　不同润滑条件下切削 304 不锈钢时对涂层刀具后刀面的 SEM/EDS 分析

图 16（a3-c3）列出了各磨损面的 EDS 分析，表 4 总结了相应的元素含量。可以看出，CTAB 切削液润滑下的磨损面 EDS 分析检测到刀具基体主要化学元素 W 的浓度最高（75.47 wt.%），表明出现了切削刃断裂现象。这是因为切削区润滑不充分，导致刀具与工件摩擦增大，首先引起材料黏附。在切削初始阶段，粘附的材料可以保护切削刃免于快速磨损。随着加工的继续，由于奥氏体不锈钢导热率低，导致刀具温度过高，最终刃口材料被撕裂并从基体中带走。因此，在 CTAB 切削液润滑下，刀具的主要磨损形式是切削刃的微崩刃。当使用去离子水时，AISI 304 不锈钢的主要化学成分明显高于

其他两种切削液（Fe 为 74.01 wt.%，Cr 为 16.89 wt.%，Ni 为 8.7% wt.%），表明其主要磨损机制为材料黏附。与 CTAB 切削液相比，纯去离子水润滑下有更多的切削液渗透到切削区间隙中，但刀具表面仍出现了严重的材料粘附。这主要是因为切削液无法深入到切削接触区去充分润滑两接触面，导致其不能有效降低与切削热相关的粘附磨损。在 SLI 切削液润滑条件下，Fe、Cr 和 Ni 含量分别比去离子水润滑时低 78.4%、34% 和 98%，而刀具涂层的两种主要化学元素 Al 和 Ti 的含量则高出约 200 倍。表明此时刀具的粘附磨损减小，加工性能得到改善。在切削过程中 SLI 切削液的渗透性更好，切削液可更高效地为切削区两接触面提供润滑，从而减轻了刀具磨损。

表 4　不同润滑条件下刀具磨损面的元素含量 （wt%）

	Fe	Cr	Ni	Al	Ti	W
CTAB	12.77	8.82	2.58	0.03	0.11	75.47
去离子水	74.01	16.89	8.7	0.05	0.13	0
SLI	15.92	11.14	0.71	6.25	35.14	0

2.3.5　润滑机理

电渗效应对切削性能的影响可反映出切削液在刀-屑接触区渗透的差异，这是对切削液在加工过程中毛细渗透机理的补充和完善。在切屑与前刀面的滑动-摩擦-分离过程中，由摩擦生电静电势产生的径向电场激发最初低能电子向外逃逸，引起电子雪崩和微等离子体发射现象，从而诱发荷电粒子发射。由于从毛细狭缝中逸出的净荷电粒子极性为负，从而在毛细管中形成了指向内部的自激轴向电场，此电场可触发毛细管中液体的电渗效应。根据上文研究结果可知，不同电渗特性切削液在切削接触区毛细管中的渗透效果存在明显差异，不同电渗特性切削液在毛细管中的润滑渗透机理如图 17 所示。

去离子水情况下，扩散层中的正离子在电场力的作用下移动，并且在溶液粘度影响下带动溶液本体形成了与自激轴向电场方向相同的电渗流，它促进了切削液进入切削区，如图 17a 所示。当使用 CTAB 切削液时，CTAB 分子在毛细管壁上的吸附改变了扩散层中的离子极性。此时扩散层中的负离子受到与轴向电场方向相反的电场力作用，如图 17b 所示。向切削区域外侧的电渗流随 CTAB 浓度而增大，阻碍了切削液的渗透，导致刀-屑接触面润滑不足。此外，SLI 分子在毛细管壁上的吸附特性在不改变极性的条件下增加了表面电荷数量，提高了扩散层中的正离子浓度。与去离子水润滑相比，SLI 切削液扩散层中的正离子受到与自激轴向电场方向相同的更大电场力作用，此时产生了更高的电渗流（如图 17c 所示），促进了切削液向切削区的进一步渗透，提高了切削液在切削区毛细管中的渗透深度，切削液得以更好地发挥润滑作用，最终改善

了切削性能。
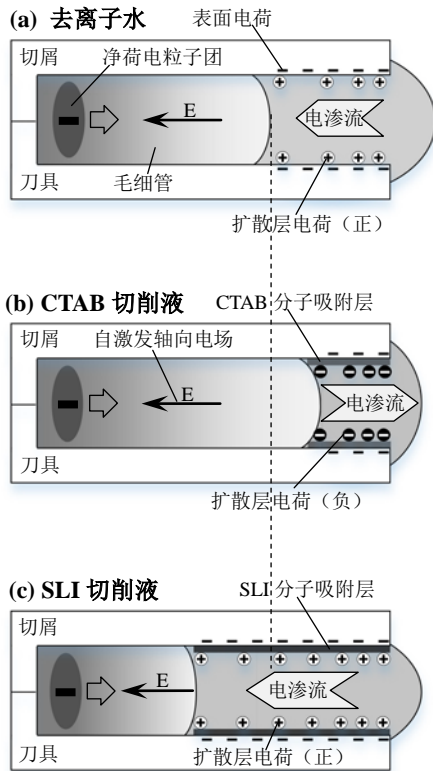
图 17 不同切削液润滑机理示意图

3 结论

本研究搭建了电渗流速度测量装置，并通过测量不同轴向电场下去离子水、含电渗抑制剂 CTAB 和含电渗促进剂 SLI 的去离子水在金属和绝缘毛细管中的电渗流速度模拟了电渗效应对水基切削液在刀-屑接触区毛细管中的渗透。此外，全面研究了基于外电子发射在不同工件切削区毛细管中所形成的自激轴向电场，并揭示了不同电渗性能切削液在切削过程中的润滑机理。结果表明，使用不同切削液润滑对金属和绝缘工件的切削性能与切削液在毛细管中的电渗流速度紧密相关。结论如下：

1. 通过应用电渗添加剂，可调节去离子水在毛细管中的渗透方向和速度。此外，绝缘毛细管中的电渗流速度明显高于金属毛细管，且电渗流速度与轴向电场强度成正比。

2. 切削液在切削区毛细管中产生电渗效应所需的轴向电场由管中发射的荷电粒子提供。采用法拉第收集板与偏置电场板相结合的方式，对切削接触区逃逸的净荷电粒子流进行了检测并确定了自激轴向电场的方向和场强，其强度范围为 1.5×10^2 V/cm – 1.09×10^3 V/cm，满足触发切削液在刀-屑间隙中产生电渗效应的条件。

3. 由于每个 SLI 分子中同时存在一个含氮的阳离子基团和两个羧酸阴离子基团，其在毛细管壁面

的吸附可使表面电荷数量提升一倍，增加了扩散层中正离子的数量，导致指向毛细管深处的电渗流增强。而 CTAB 分子中的季铵盐阳离子基团吸附在带负电荷的毛细管壁后，表面电荷极性随浓度发生了转变，导致扩散层离子极性由正变负，最终改变了电渗流方向。试验结果表明，在电渗促进型 SLI 切削液润滑条件下，对 AISI 304 和 PE 工件的切削力比纯去离子水润滑下降低了 20% ~ 30%；而在电渗抑制型 CTAB 切削液润滑下，由于电渗流方向的改变，切削力增加了 15% ~ 30%。此外，对切削 AISI 304 所用刀具切削刃的 SEM/EDS 分析表明，车削过程中，切削刃从粘附磨损过渡到微崩刃，表明在电渗效应作用下切削液对切削区的润滑与其渗透效果紧密相关。

本研究为了解电渗效应对水基切削液在不同刀具和工件材料组合下润滑潜力的影响，以及在不同刀-屑界面上的渗透机理提供了新颖的观点，为今后在不同加工方式下提高商品润滑液使用效率的研究提供了依据。考虑到切削区毛细管中的电渗流在现阶段不便直接观测，商用切削液在加工接触区微毛细管中电渗流的实时监测将在下一阶段的实验室或加工环境中进行，以进一步探究不同加工条件下电渗效应对水基甚至油基切削液渗透影响的普遍性。

参 考 文 献

[1] V A Godlevski, A V Volkov, V N Latyshev, et al. The kinetics of lubricant penetration action during machining[J]. Lubrication Science, 1997, 9(2)：127-140.

[2] J A Willians. The action of lubricants in metal cutting[J]. Journal Mechanical Engineering, 1977(5)：202-212.

[3] V A Godlevskiy. Technological lubricating means: Evolution of materials and ideas[J]. Frontiers Of Mechanical Engineering, 2016, 11(1)：101-107.

[4] S M C. On the action of metal cutting fluids at low speeds[J]. Wear, 1959, 2(3)：217-227.

[5] E M Podgaetsky. Determining the Boundaries of the Concentration Area of Action of the Rehbinder Effect for an S-shaped Adsorption Isotherm[J]. Protection Of Metals And Physical Chemistry Of Surfaces, 2018, 54(5)：769-777.

[6] M Yamada, H Shigemune, S Maeda, et al. Temperature and Humidity Dependence of Marangoni Convection and Its Effect on the Self-propulsion of an Oil Droplet[J]. Chemistry Letters, 2021, 50(3)：493-496.

[7] J Hwang. Direct Observation of Fluid Action at the Chip-Tool Interface in Machining[J]. International Journal Of Precision Engineering And Manufacturing, 2014, 15(10)：2041-2049.

[8] J Hwang, S Chandrasekar. Contact Conditions at the Chip-Tool Interface in Machining[J]. International Journal Of Precision Engineering And Manufacturing,

2011, 12(2)：183-193.

[9] S Mane, S S Joshi, S Karagadde, et al. Modeling of variable friction and heat partition ratio at the chip-tool interface during orthogonal cutting of Ti-6Al-4V[J]. Journal Of Manufacturing Processes, 2020, 55：254-267.

[10] K Goto. The Influence Of Surface-Induced Voltage on the Wear Mode Of Stainless-Steel[J]. Wear, 1995, 185(1-2)：75-81.

[11] J Govindaraj, S. Subbiah. Charged-Particle Emissions During Material Deformation, Failure and Tribological Interactions of Machining[J]. Journal Of Tribology-Transactions Of the Asme, 2019, 141(3).

[12] R Pham, R C Virnelson, R M Sankaran, et al. Contact charging between surfaces of identical insulating materials in asymmetric geometries[J]. Journal Of Electrostatics, 2011, 69(5)：456-460.

[13] WANG L, Y Dong, J Tao, et al. Study of the mechanisms of contact electrification and charge transfer between polytetrafluoroethylene and metals[J]. Journal of Physics D: Applied Physics, 2020, 53(28)：285-302.

[14] M W Williams. Triboelectric charging of insulating polymers-some new perspectives[J]. Aip Advances, 2012, 2(1).

[15] KAEH OAOlufayo, MM Kadernani. Tribo-electric Charging in the Ultra-high Precision Machining of Contact lens Polymers[J]. Procedia Materials Science, 2014(6); 194-201.

[16] CHANG Y P, CHU H M, CHOU H M. Effects of mechanical properties on the tribo-electrification mechanisms of iron rubbing with carbon steels[J]. Wear, 2007, 262(1-2)：112-120.

[17] K Nakayama, F Yagasaki. The Flow of Triboplasma[J]. Tribology Letters, 2019, 67(3).

[18] G J Molina, M J Furey, A L Ritter, et al. Triboemission from alumina, single crystal sapphire, and aluminum[J]. Wear, 2001, 249(3-4)：214-219.

[19] K Nakayama, J A Leiva, Y Enomoto. Chemi-emission of electrons from metal surfaces in the cutting process due to metal/gas interactions[J]. Tribology International, 1995, 28(8)：507-515.

[20] K Nakayama, T Fujimoto. The energy of electrons emitted from wearing solid surfaces[J]. Tribology Letters, 2004, 17(1)：75-81.

[21] L Scudiero, J T Dickinson, Y Enomoto. The electrification of flowing gases by mechanical abrasion of mineral surfaces[J]. Physics And Chemistry Of Minerals, 1998, 25(8)：566-573.

[22] T Sakurai, K Sato. Study of Corrosivity and Correlation between Chemical Reactivity and Load-Carrying Capacity of Oils Containing Extreme Pressure Agents[J]. A S L E Transactions, 1966, 9(1)：77-87.

[23] L Z, FENG Bohua, ZHANG Tao, et al. Capillary electroosmosis properties of water lubricants with different electroosmotic additives under a steel-on-steel sliding interface[J]. Friction, 2021.

[24] XU Xuefeng, LUAN Zhiqiang, ZHANG Tao, et al. Effects of electroosmotic additives on capillary penetration of lubricants at steel/steel and steel/ceramic friction interfaces[J]. Tribology International, 2020, 151.

[25] T J Harvey, R J K Wood, G Denuault, et al. Investigation of electrostatic charging mechanisms in oil lubricated tribo-contacts[J]. Tribology International, 2002, 35(9)：605-614.

[26] D Mockel, E Staude, M Dal-Cin, et al. Tangential flow streaming potential measurements: Hydrodynamic cell characterization and zeta potentials of carboxylated polysulfone membranes[J]. Journal Of Membrane Science, 1998, 145(2)：211-222.

[27] E J van der Wouden, T Heuser, D C Hermes, et al. Field-effect control of electro-osmotic flow in microfluidic networks[J]. Colloids And Surfaces a-Physicochemical And Engineering Aspects, 2005, 267(1-3)：110-116.

[28] HE C Y, ZHU Z F, GU C Y, et al. Stacking open-capillary electroosmotic pumps in series to boost the pumping pressure to drive high-performance liquid chromatographic separations[J]. Journal Of Chromatography A, 2012, 1227：253-258.

[29] REN Q L. Bioparticle delivery in physiological conductivity solution using AC electrokinetic micropump with castellated electrodes[J]. Journal Of Physics D-Applied Physics, 2018, 51(46).

[30] CHEN L X, MA J P, GUAN Y F. An electroosmotic pump for packed capillary liquid chromatography[J]. Microchemical Journal, 2003, 75(1)：15-21.

[31] 仲武, 陈云飞. 毛细管电渗流微泵的流体动力学的数值仿真[J]. 机械工程学报, 2004, 40(2)：73-77.
ZHONG Wu, CHEN Yunfei. Hydrodynamic analysis of electroosmotic flow in micropump[J]. Journal of Mechanical Engineering, 2004, 40(2)：73-77.

[32] Liu J Y, Liu H P, Han R D, et al. The study on lubrication action with water vapor as coolant and lubricant in cutting ANSI 304 stainless steel[J]. International Journal Of Machine Tools & Manufacture, 2010, 50(3)：260-269.

[33] LI L, WANG X Y, PU Q S, et al. Advancement of electroosmotic pump in microflow analysis[J]. Analytica Chimica Acta, 2019, 1060：1-16.

[34] P Sazelova, V Kasicka, D Koval, et al. Control of EOF in CE by different ways of application of radial electric field[J]. Electrophoresis, 2007, 28(5)：756-766.

[35] T T Razunguzwa, A T Timperman. Fabrication and characterization of a fritless microfabricated electroosmotic pump with reduced pH dependence[J]. Analytical Chemistry, 2004, 76(5)：1336-1341.

[36] Q Guan, S D Noblitt, C S Henry. Electrophoretic separations in poly(dimethylsiloxane) microchips using a mixture of ionic and zwitterionic surfactants[J]. Electrophoresis, 2012, 33(2)：379-387.

[37] S Bekri, L Leclercq, H Cottet. Influence of the ionic strength of acidic background electrolytes on the

separation of proteins by capillary electrophoresis[J]. Journal Of Chromatography A, 2016, 1432：145-151.

[38] WANG W, ZHOU F, ZHAO L, et al. Measurement of electroosmotic flow in capillary and microchip electrophoresis[J]. Journal Of Chromatography A, 2007, 1170(1-2)：1-8.

[39] K Heinig, C Vogt, G Werner. Determination of cationic surfactants by capillary electrophoresis[J]. Fresenius Journal Of Analytical Chemistry, 1997, 358(4)：500-505.

[40] S Movahed, S Khani, J Z Wen, et al. Electroosmotic flow in a water column surrounded by an immiscible liquid[J]. Journal Of Colloid And Interface Science, 2012, 372：207-211.

[41] 陈义. 毛细管电泳技术及应用[M]. 北京：化学工业出版社, 2006.
CHEN Y. Capillary electrophoresis and its application[M], Beijing：Chemical industry, 2006.

[42] WANG W, ZHAO L, ZHANG J R, et al. Indirect amperometric measurement of electroosmotic flow rates and effective mobilities in microchip capillary electrophoresis[J]. Journal Of Chromatography A, 2007, 1142(2)：209-213.

[43] GAO T. Dispersing mechanism and tribological performance of vegetable oil-based CNT nanofluids with different surfactants[J]. Tribology International, 2019, 131：51-63.

[44] A Gaspar, L Gabor. Study of quantitative analysis of traces in low-conductivity samples using capillary electrophoresis with electrokinetic injection[J]. Journal Of Chromatography A, 2005, 1091(1-2)：163-168.

[45] W S R Teixeira, M S F Santos, J Gruber, et al. Determination of neutral diols and carboxylic acids formed during glycerol electrooxidation by capillary electrophoresis with dual (CD)-D-4[J]. Talanta, 2018, 178：1040-1045.

[46] K Nakayama. Effect of Normal Force on the Triboplasma Generation Under Oil Lubrication[J]. Tribology Letters,
2014, 53(2)：449-456.

[47] K Nakayama. Triboemission of charged particles and resistivity of solids[J]. Tribology Letters, 1999, 6(1)：37-40.

[48] K Nakayama. Triboemission of Charged Particles from Various Solids Under Boundary Lubrication Conditions[J]. Wear, 1994, 178：61-67.

[49] K Nakayama, H Hashimoto. Triboemission From Various Materials In Atmosphere[J]. Wear, 1991, 147(2)：335-343.

[50] S S Wells, E De La Toba, C R Harrison. Metal cation control of electroosmotic flow magnitude in phospholipid-coated capillaries[J]. Electrophoresis, 2016, 37(10)：1303-1309.

[51] XU X F, LV T, LUAN Z Q, et al. Capillary penetration mechanism and oil mist concentration of Al2O3 nanoparticle fluids in electrostatic minimum quantity lubrication (EMQL) milling[J]. International Journal Of Advanced Manufacturing Technology, 2019, 104(5-8)：1937-1951.

[52] A Jawaid, S Sharif, S Koksal. Evaluation of wear mechanisms of coated carbide tools when face milling titanium alloy[J]. Journal of Materials Processing Technology, 2000, 99(1-3)：266-274.

[53] LV T, HUANG S Q, LIU E T, et al. Tribological and machining characteristics of an electrostatic minimum quantity lubrication (EMQL) technology using graphene nano-lubricants as cutting fluids[J]. Journal Of Manufacturing Processes, 2018, 34：225-237.

作者简介：冯伯华，男，1994 年出生，博士研究生。主要研究方向为切削液渗透。
E-mail：512394246@qq.com
许雪峰(通信作者)，男，1964 年出生，博士，教授，博士研究生导师。
主要研究方向为摩擦学、绿色制造技术、精密和特种加工技术。
E-mail：xuxuefeng@zjut.edu.cn

Friction期刊基本信息

基本信息	登录收藏

期刊名字	Friction FRICTION	LetPub评分 8.3 ★★★★☆ 62人评分　我要评分 ✏ 声誉 ━━━━━━━━ 9.1 影响力 ━━━━━━ 7.2 速度 ━━━━━━━ 8.5

期刊ISSN	2223-7690
E-ISSN	2223-7704
2021-2022最新影响因子 （数据来源于搜索引擎）	注册或登录后，查看影响因子和历年趋势图
2021-2022自引率	9.70%　注册或登录后，查看自引率趋势图
h-index ⓘ	19

CiteScore ⓘ	CiteScore	SJR	SNIP	CiteScore排名			
	7.60	1.283	2.102	学科	分区	排名	百分位
				大类：Engineering 小类：Mechanical Engineering	Q1	61 / 601	89%
				大类：Engineering 小类：Surfaces, Coatings and Films	Q1	16 / 129	87%

期刊简介	Friction is a peer-reviewed international journal for the publication of theoretical and experimental research works related to the friction, lubrication and wear. Original, high quality research papers and review articles on all aspects of tribology are welcome, including, but are not limited to, a variety of topics, such as: Friction: Origin of friction, Friction theories, New phenomena of friction, Nano-friction, Ultra-low friction, Molecular friction, Ultra-high friction, Friction at high speed, Friction at high temperature or low temperature, Friction at solid/liquid interfaces, Bio-friction, Adhesion, etc. Lubrication: Superlubricity, Green lubricants, Nano-lubrication, Boundary lubrication, Thin film lubrication, Elastohydrodynamic lubrication, Mixed lubrication, New lubricants, New additives, Gas lubrication, Solid lubrication, etc. Wear: Wear materials, Wear mechanism, Wear models, Wear in severe conditions, Wear measurement, Wear monitoring, etc. Surface Engineering: Surface texturing, Molecular films, Surface coatings, Surface modification, Bionic surfaces, etc. Basic Sciences: Tribology system, Principles of tribology, Thermodynamics of tribo-systems, Micro-fluidics, Thermal stability of tribo-systems, etc. Friction is an open access journal. It is published quarterly by Tsinghua University Press and Springer, and sponsored by the State Key Laboratory of Tribology (TsinghuaUniversity) and the Tribology Institute of Chinese Mechanical Engineering Society.

通讯方式	ONE NEW YORK PLAZA, SUITE 4600 , NEW YORK, United States, NY, 10004
出版商	Tsinghua University Press
涉及的研究方向	Engineering-Mechanical Engineering
出版国家或地区	PEOPLES R CHINA
出版语言	English
出版周期	Bimonthly
出版年份	2013
年文章数 ⓘ	95　注册或登录后，查看年文章数趋势图
Gold OA文章占比	100.00%
研究类文章占比： 文章÷（文章＋综述）	91.58%

WOS期刊SCI分区 ⓘ （2021-2022年最新版）	WOS分区等级：1区

按学科分区
ENGINEERING, MECHANICAL　Q1

中科院《国际期刊预警 名单（试行）》名单 ⓘ	2021年12月发布的2021版：不在预警名单中 2021年01月发布的2020版：不在预警名单中

注册或登录后，查看中科院SCI期刊分区趋势图

中科院SCI期刊分区 （2021年12月最新基础版）	大类学科	小类学科	Top期刊	综述期刊
	工程技术　1区	ENGINEERING, MECHANICAL 工程：机械　1区	是	否

中科院SCI期刊分区 （2021年12月最新升级版）	大类学科	小类学科	Top期刊	综述期刊
	工程技术　1区	ENGINEERING, MECHANICAL 工程：机械　1区	是	否

中科院SCI期刊分区 （2020年12月旧的升级版）	大类学科	小类学科	Top期刊	综述期刊
	工程技术　1区	ENGINEERING, MECHANICAL 工程：机械　1区	是	否

Science Citation Index Expanded (SCIE)

基本信息

☆ 登录收藏

期刊名字	JOURNAL OF MATERIALS PROCESSING TECHNOLOGY J MATER PROCESS TECH

LetPub评分

8.1 ★★★★☆ 111人评分   **我要评分** ✎

声誉		8.5
影响力		7.6
速度		8.4

期刊ISSN	0924-0136
E-ISSN	1873-4774
2021-2022最新影响因子 （数据来源于搜索引擎）	注册或登录后，查看影响因子和历年趋势图
2021-2022自引率	6.30% 注册或登录后，查看自引率趋势图
h-index ⓘ	158

微信扫码收藏此期刊

CiteScore ⓘ	CiteScore	SJR	SNIP	CiteScore排名			
	11.30	1.578	2.168	**学科**	**分区**	**排名**	**百分位**
				大类：Materials Science 小类：Metals and Alloys	Q1	7 / 155	95%
				大类：Materials Science 小类：Industrial and Manufacturing Engineering	Q1	18 / 338	94%
				大类：Materials Science 小类：Computer Science Applications	Q1	43 / 747	94%
				大类：Materials Science 小类：Ceramics and Composites	Q1	9 / 115	92%

期刊简介	The Journal of Materials Processing Technology covers the processing techniques used in manufacturing components from metals and other materials. The journal aims to publish full research papers of original, significant and rigorous work and so to contribute to increased production efficiency and improved component performance. Areas of interest to the journal include: • Casting, forming and machining • Additive processing and joining technologies • The evolution of material properties under the specific conditions met in manufacturing processes

文章÷（文章＋综述）	91.82%

WOS期刊SCI分区 ⓘ （2021-2022年最新版）	WOS分区等级：2区

按学科分区	
ENGINEERING, INDUSTRIAL	Q2
ENGINEERING, MANUFACTURING	Q2
MATERIALS SCIENCE, MULTIDISCIPLINARY	Q2

中科院《国际期刊预警名单（试行）》名单 ⓘ	2021年12月发布的2021版：不在预警名单中 2021年01月发布的2020版：不在预警名单中

注册或登录后，查看中科院SCI期刊分区趋势图

中科院SCI期刊分区 （2021年12月最新基础版）	大类学科		小类学科		Top期刊	综述期刊
	工程技术	2区	ENGINEERING, INDUSTRIAL 工程：工业	2区	否	否
			ENGINEERING, MANUFACTURING 工程：制造	2区		
			MATERIALS SCIENCE, MULTIDISCIPLINARY 材料科学：综合	3区		

中科院SCI期刊分区 （2021年12月最新升级版）ⓘ	大类学科		小类学科		Top期刊	综述期刊
	材料科学	1区	ENGINEERING, MANUFACTURING 工程：制造	1区	是	否
			MATERIALS SCIENCE, MULTIDISCIPLINARY 材料科学：综合	1区		
			ENGINEERING, INDUSTRIAL 工程：工业	2区		

中科院SCI期刊分区 （2020年12月旧的升级版）	大类学科		小类学科		Top期刊	综述期刊
	材料科学	2区	ENGINEERING, INDUSTRIAL 工程：工业	1区	是	否
			ENGINEERING, MANUFACTURING 工程：制造	2区		
			MATERIALS SCIENCE, MULTIDISCIPLINARY 材料科学：综合	2区		

SCI期刊收录coverage	Science Citation Index Expanded (SCIE) Scopus (CiteScore)

Ei 收录
百强报刊
国家期刊奖（三届）
第二届中国出版政府奖期刊奖
中国科技期刊卓越行动计划梯队期
刊项目资助
中国科协精品科技期刊TOP50
中国科协中文科技期刊精品建设计
划学术创新引领项目资助

点击进入

SCI收录
百强报刊
中国最具国际影响力学术期刊
中国科技期刊卓越行动计划重点期
刊项目资助
中国科技期刊登峰行动计划项目资
助
中国科技期刊国际影响力提升计划
项目资助

点击进入

学报动态 News

more >

- 重磅发布｜CJME最新影响因子2.964,Q2区！　　2022-06-28
- 西安交通大学雷亚国教授团队：跨设备的机械故障靶向迁移诊…　　2022-10-31
- 第五届中国机械工程教育大会暨中国机械行业卓越工程师教育…　　2022-10-10
- 中国工程院机械与运载工程学部关于举办第二届人工自愈与装…　　2022-08-03
- 重磅｜机械工程领域SCI期刊一览(2021JCR)　　2022-06-28
- 《中国机械工程技术路线图（2021版）》重磅发布　　2022-05-18
- 重磅！2022年研考国家线公布　　2022-03-14
- 2022全球大学学术影响力排名出炉！　　2022-02-08
- 机械工业出版社学术媒体中心刊群多位编委入选2021年两院…　　2021-11-22